

THE MAPPINGS III LIBRARY OF FAST RADIATIVE SHOCK MODELS

MARK G. ALLEN

Observatoire de Strasbourg UMR 7550 Strasbourg 67000, France

BRENT A. GROVES

Sterrewacht Leiden, Leiden University, Neils Bohrweg 2, Leiden 2333-CA The Netherlands

MICHAEL A. DOPITA

Research School of Astronomy and Astrophysics, Australian National University, Cotter Road , Weston Creek ACT 2611, Australia

RALPH S. SUTHERLAND

Research School of Astronomy and Astrophysics, Australian National University, Cotter Road , Weston Creek ACT 2611, Australia

LISA J. KEWLEY

Institute for Astronomy, University of Hawaii, 2680 Woodlawn Drive Manoa, HI 96822. USA

ABSTRACT

We present a new library of fully-radiative shock models calculated with the MAPPINGS III shock and photoionization code. The library consists of grids of models with shock velocities in the range $v_s=100\text{-}1000\text{ km s}^{-1}$ and magnetic parameters B/\sqrt{n} of $10^{-4}\text{-}10\text{ }\mu\text{G cm}^{3/2}$ for five different atomic abundance sets, and for a pre-shock density of 1.0 cm^{-3} . Additionally, Solar abundance model grids have been calculated for densities of 0.01, 0.1, 10, 100, and 1000 cm^{-3} with the same range in v_s and B/\sqrt{n} . Each model includes components of both the radiative shock and its photoionized precursor, ionized by the EUV and soft X-ray radiation generated in the radiative gas. We present the details of the ionization structure, the column densities, and the luminosities of the shock and its precursor. Emission line ratio predictions are separately given for the shock and its precursor as well as for the composite shock+precursor structure to facilitate comparison with observations in cases where the shock and its precursor are not resolved. Emission line ratio grids for shock and shock+precursor are presented on standard line ratio diagnostic diagrams, and we compare these grids to observations of radio galaxies and a sample of AGN and star forming galaxies from the Sloan Digital Sky Survey. This library is available online, along with a suite of tools to enable the analysis of the shocks and the easy creation of emission line ratio diagnostic diagrams. These models represent a significant increase in parameter space coverage over previously available models, and therefore provide a unique tool in the diagnosis of emission by shocks.

Subject headings: hydrodynamics - shock waves - ISM: abundances,- Galaxies: Nuclei, Galaxies: Seyfert - infrared: ISM, Ultraviolet: ISM, X-rays: ISM

1. INTRODUCTION

Supersonic motions are a common phenomenon in our complex and fascinating Universe. The kinetic energy of such motions will almost inevitably be eventually dissipated through radiative shocks. Cloud-cloud collisions, the expansion of H II regions into the surrounding interstellar medium, outflows from young stellar objects, supernova blast waves, outflows from active and starburst galaxies, and collisions between galaxies are all examples of astrophysical situations in which radiative shock waves provide an important component of the total energy budget and may determine the line emission spectrum.

In this paper we do not consider very slow (molecular) shocks or indeed, the faster atomic shocks for which the theory has been well-developed by such authors as Dopita (1977) or Raymond (1979). Rather, we consider only fast shocks, where the ionizing radiation generated

by the cooling of hot gas behind the shock front generates a strong radiation field of extreme ultraviolet and soft X-ray photons, which leads to significant photoionizing effects. The detailed theory of steady-flow photoionizing (or auto-ionizing) shocks was developed by Sutherland et al. (1993) and Dopita & Sutherland (1995, 1996) (hereafter DS95 and DS96). A detailed text-book development of the theory of shocks is given in Dopita & Sutherland (2003).

In photoionizing shocks, the flux of the ionizing radiation emitted by the shock increases in approximate proportion to the energy flux through the shock ($\propto v_s^3$). The ratio of this flux in advance of the shock to the pre-shock density, classified as the ionization parameter, determines the velocity of the photoionization front that is driven into the pre-shock gas. At low values of the ionization parameter, the velocity of the photoionization front is lower than the velocity of the shock and the ionizing photons are absorbed in the immediate vicinity of the shock front. The effect of this is to change the ion-

TABLE 1
ABUNDANCE SETS (BY NUMBER WRT HYDROGEN)

Element	Solar	Solar $\times 2$	dopita2005	LMC	SMC
H	0.00	0.00	0.00	0.00	0.00
He	-1.01	-1.01	-1.01	-1.05	-1.09
C	-3.44	-3.14	-4.11	-3.96	-4.24
N	-3.95	-3.65	-4.42	-4.86	-5.37
O	-3.07	-2.77	-3.56	-3.65	-3.97
Ne	-3.91	-3.61	-3.91	-4.39	-4.73
Na			-6.35	-4.85	-5.92
Mg	-4.42	-4.12	-5.12	-4.53	-5.01
Al	-5.53	-5.23	-7.31	-4.28	-5.60
Si	-4.45	-4.15	-5.49	-5.29	-4.69
S	-4.79	-4.49	-5.01	-7.23	-5.41
Cl			-6.70		-7.30
Ar	-5.44	-5.14	-5.44	-5.71	-6.29
Ca	-5.88	-5.58	-8.16	-6.03	-6.16
Fe	-4.63	-4.33	-6.55	-4.77	-5.11
Ni			-7.08	-6.04	-6.14

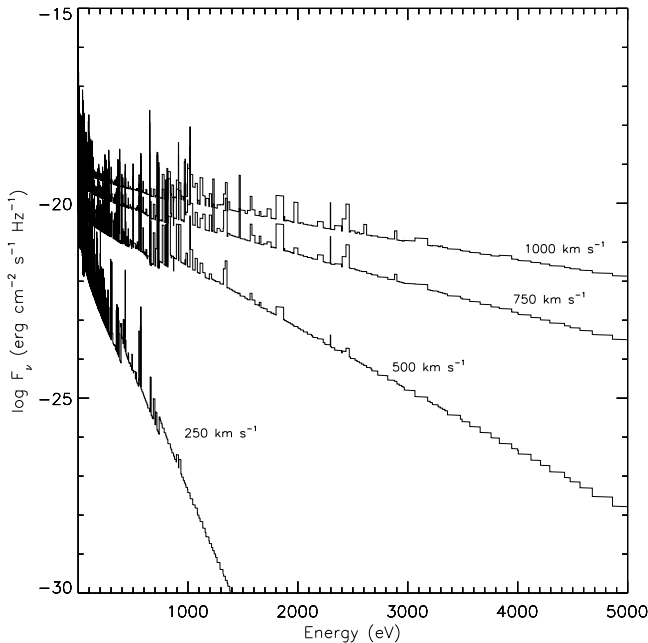


FIG. 1.— Ionizing spectra generated by $v_s=250, 500, 750$ and 1000 km s^{-1} shock models with $n=1.0 \text{ cm}^{-3}$ and solar abundance.

ization state of the gas feeding across the shock front. As the velocity of the shock increases, the emitted ionizing flux, and therefore the velocity of the photoionization front, increases rapidly. At shock velocities above a certain limit ($v_s \approx 170 \text{ km s}^{-1}$), the ionization front velocity exceeds that of the shock (and is supersonic with respect to the pre-shock gas) and the photoionization front detaches from the shock front as an R-Type ionization front¹. This front expands to form a precursor H II region ahead of the shock. At the highest shock velocities, the photoionized precursor emission may come to dominate the optical emission of the shock, and the global radiative shock spectrum provides a rich mixture of emission

¹ R-Type ionization fronts are defined as being supersonic with respect to the gas ahead of the front. (subsonic ionization fronts are classified as D-Type) see McKee & Hollenbach (1980)

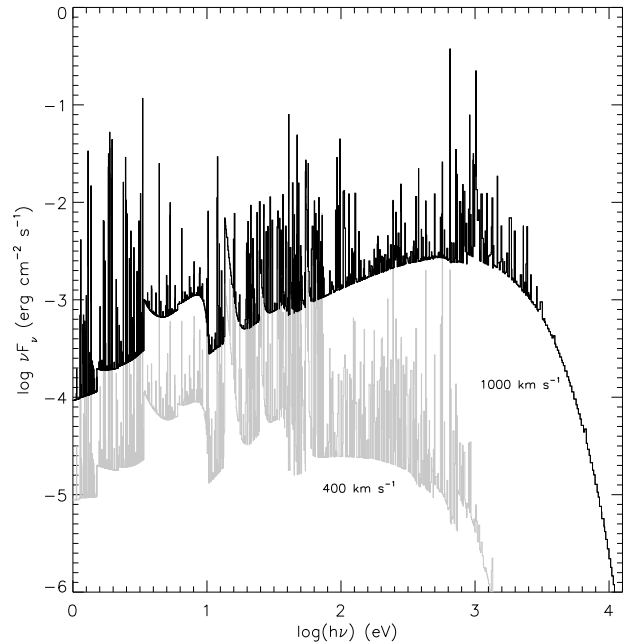
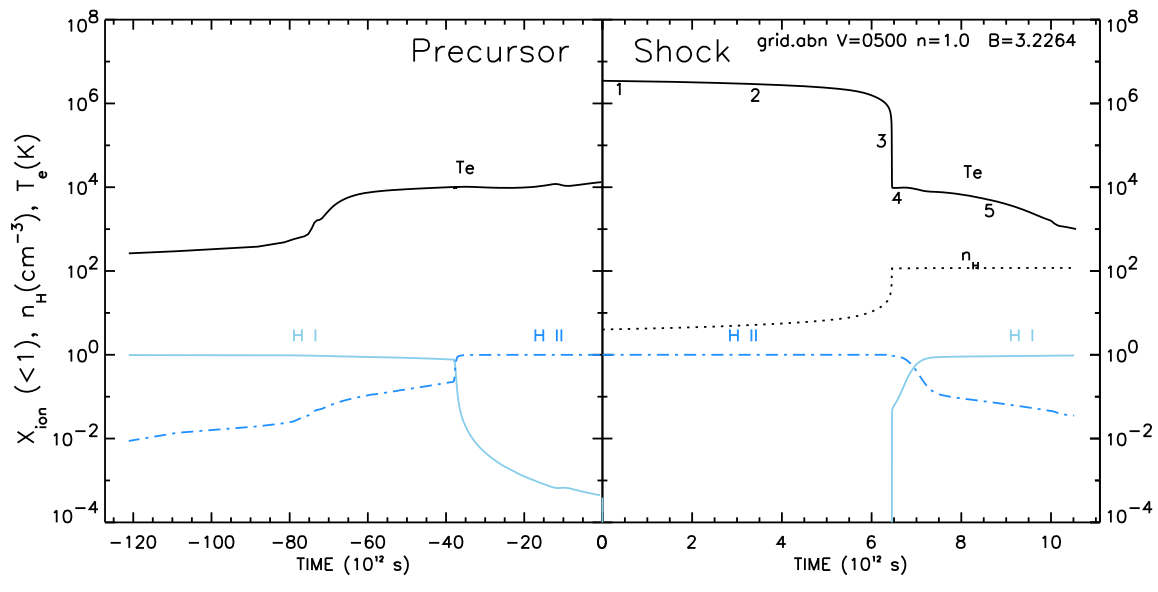


FIG. 2.— Ionizing spectra of $v_s=400$ and 1000 km s^{-1} shock models shown on νF_ν scale.

lines from both high- and low-ionization species.

Appreciable photoionization effects are also produced in the gas behind the shock front, near to the recombination region of the shock. However, in this shock region the velocity of the ionization front is much slower due to the gas compression through the shock front and the ionization front stays trapped in the recombination region to much higher shock velocities. When magnetic effects are negligible, the compression of the gas in the shocked region is proportional to the square of the Mach number in the pre-shock gas, $\mathcal{M} = v_s/c_{II}$, where c_{II} is the sound speed in the pre-shock gas. When the magnetic field pressure in the post-shock gas dominates over the gas pressure, the compression factor is determined by the Alfvén Mach Number, \mathcal{M}_A , which is the ratio of the shock velocity to the Alfvén velocity; $v_A = (B^2/4\pi\rho)^{1/2}$, where B is the transverse component of the pre-shock magnetic field, and ρ is the pre-shock mass density. Thus the presence of magnetic fields act to limit the compression through the shock. In order to account for this effect in computations of the shock structure, DS96 developed the concept of a magnetic parameter; B/\sqrt{n} , where n is the pre-shock particle number density.

The grid of low density photoionizing shock models described in DS96 has proved to be a valuable resource to the astronomical community for assessing the role of photoionizing shocks in a range of astrophysical objects. This utility is increased by their availability in electronic form from the AAS CD-ROM Series, Vol 7. (see Leitherer et al. 1996). These models have most often been applied in studies of the narrow line regions (NLR) of active galaxies, developing the debate on the relative roles of shock and/or photoionization excitation of the NLR, and the question of the radiative versus mechanical energy output of active galactic nuclei (AGN). Other uses of the models have included studies of ionized gas around high velocity clouds (Fox et al. 2004), and the intergalac-



[t]

FIG. 3.— The hydrogen ionization structure, temperature profile and density profile of a shock and precursor. The vertical axis represents i) the ionization fraction X_{ion} (values ≤ 1) for the ionization structure curves, ii) the electron temperature profile (T_e) in degrees Kelvin, shown as the upper line plotted in the figure, and iii) the hydrogen density (n_H) in cm^{-3} , shown by the dotted line in the shock region (right) panel of the figure. As n_H is constant in the precursor (left) it is not plotted. The horizontal axis represents the time since passage of the shock front, with positive values for the shock structure shown in the right of the figure, and negative values for the precursor region where the shock is yet to arrive. The numerical labels indicated on the temperature profile of the shock correspond to different regions of the shock structure as described in the text. The model plotted here is our fiducial model with solar abundances, equipartition magnetic field, a precursor density of $n_H = 1 \text{ cm}^{-3}$, and shock velocity of $v_s = 500 \text{ km s}^{-1}$, as labelled in the upper right corner of the figure. See the electronic edition of the Journal for a color version of this figure.

tic medium (Shull et al. 2003).

In DS95 these models were applied to optical line ratios observed in NLRs. They found that Seyferts have values close to the shock + precursor predictions and that Low Ionization Emission Line Region (LINER) galaxies fall within the range of the shock-only models. In Allen et al. (1998) we highlighted the importance of UV line ratios which help separate shock and photoionization models, and we defined a set of UV line ratio diagnostic diagrams. These UV diagnostics were applied to individual objects M 87 (Dopita et al. 1997), NGC 5728 and NGC 5643 (Evans et al. 1999) and NGC 1068 (Groves et al. 2004). NGC 2992 was also investigated in detail with optical diagnostics and other multi-wavelength data (Allen et al. 1999).

The DS95 model grid has also been extensively used by other authors in studies of AGN. Best et al. (2000) and Inskip et al. (2002) used optical and UV line ratios to show that shocks associated with radio sources in $z \sim 1$ 3CR radio galaxies can dominate the kinematics and ionization as the radio source expands through the interstellar medium of the host galaxy. These models have also application to the analysis of emission lines in high redshift radio galaxies (Villar-Martin et al. 1997; Maxfield et al. 2002; De Breuck et al. 2000; Villar-Martín et al. 2003; Iwamuro et al. 2003; Reuland et al. 2007), and in studies of individual low redshift active galaxies including NGC 4151 (Nelson et al. 2000), M 51 (Bradley et al. 2004), M 87 (Sabra et al. 2003), Mkn 78 (Whittle et al. 2005), 3C 299 (Feinstein et al. 1999), NGC 2110 and NGC 5929 (Ferruit et al. 1999).

Studies of individual objects make it obvious that higher dimensional modeling of the physical structures and radiation fields associated with shocks is necessary

in order to be able to more closely model these complex physical systems, and to be able to draw deeper conclusions. Indeed the 1-D, steady-flow nature of these models is acknowledged as their greatest limitation, since all fast shocks are subject to thermal instability, and the generation of secondary shocks within the cooling zone. To address these issues, much effort is being put into higher dimensional numerical simulations of radiative shocks, in particular in the area of understanding the role of local thermal and dynamical instabilities on both the shock structure and on the emergent spectrum (Sutherland et al. 2003). However, given the complexities inherent in their computation, and the large amount of supercomputer time required, complete grids of model predictions from full 3-D models are some time off, and until then, modeling will most likely favour simulations of individual and specific cases.

Thus, the simpler 1-D models remain a useful tool for comparing with observations of both individual objects and in the investigation of the mean parameters of groups of objects observed in surveys. Furthermore, these models serve as a stepping stone towards higher dimensional models. For example, under some simplifying assumptions the radiative properties of 1-D models may be mapped onto those of 3-D hydrodynamical models. In particular, thermally unstable shocks of a given velocity, v_s , behave similarly to steady-flow shocks with shock velocities $\sim \frac{2}{3}v_s$ (Sutherland et al. 2003). Bearing in mind these effects thermal instability, we advise that care should be taken in the use of 1-D models to derive physical parameters in individual cases, or at least allow for this factor of 2/3.

In this paper we present a new library of 1-D steady flow photoionizing shock models, calculated with an

updated version of the shock modeling code, MAPPINGS III. The library is an improvement upon and extension of the DS95 & DS96 models, and includes a range of chemical abundance sets, pre-shock densities from 0.01 to 1000 cm⁻³, velocities up to 1000 km s⁻¹, magnetic fields from 10⁻¹⁰ to 10⁻⁴ G, and magnetic parameters (B/\sqrt{n}) from 10⁻⁴ to 100 $\mu\text{G cm}^{3/2}$. These new model grids therefore supersede the previous models, and are designed to be of maximum utility to observers for comparing observations with photoionizing shock models.

As well as reiterating the technique used in MAPPINGS to create the shock models, we discuss in detail the radiation fields generated by shocks, and the resulting ionization, density and temperature structure of shocks for the range of parameters considered. We also present the resulting model grids on a range of ultraviolet, optical and infrared emission-line diagnostic diagrams, discussing the effects of the various parameters upon the grids, and demonstrate their usefulness and applicability by comparing these grids with emission-line galaxy sample from the Sloan Digital Sky Survey (SDSS).

We introduce the MAPPINGS III online shock library, the main access point for the results of the shock models, which includes both the resulting emission lines and column depths from the models, as well as the full results of the MAPPINGS III models for detailed analysis. Also included as part of the library are the analysis tools used within this work, providing a simple and easy mechanism to determine the shock diagnostic power of any emission-line ratios.

2. MODELING TECHNIQUE

The models presented here have been calculated with the MAPPINGS III shock and photoionization modeling code, version IIIq. This is an updated version of the MAPPINGS II code which was described in Sutherland & Dopita (1993). The main enhancements of version III include the use of a higher resolution radiation vector, and a more stable scheme for choosing time-steps which allows computation of higher velocity shocks. Other improvements include the explicit inclusion of all the He II emission lines, and a corrected computation of the neutral oxygen emission. Further details on the use of and the chronology of the development of MAPPINGS models may be found at the MAPPINGS Online web pages². Various improvements to the calculation of photoionization processes have been implemented in version III (Groves et al. 2004a, 2007) although the dust effects discussed there have not been considered in these shock models, which are fundamentally dust-free. This approximation is probably a physical one, since in the faster shocks dust will be effectively destroyed by grain-grain collisions, through both shattering and spallation, and by thermal sputtering. The physics of these processes have been discussed in detail Draine & Salpeter (1979); Dwek, Foster & Vancura (1996); Jones et al. (1994, 1996); Pineau de Fôrets & Flower (1997) and Perna & Lazati (2002). We have in any case run models with depleted abundances to facilitate comparison with the earlier DS96 high-velocity shock modeling, so our different model grids can be used to provide some estimate of the effect of dust depletion on the output spectra.

MAPPINGS III uses exactly the same computational recipe for calculating the flow solution of these one-dimensional radiative shock models as described in detail in DS96 for MAPPINGS II. Briefly, the hydrodynamics of the flow are derived from the Rankine-Hugoniot jump conditions including the magnetic field terms. The four Rankine-Hugoniot conditions, equations 1 - 4, represent the conservation of mass, conservation of momentum, the condition that the magnetic field is locked into the ionized plasma, and conservation of energy (see Heng et al. (2007) for a generalization of these conditions). These equations connect two points in the flow at times t and t_0 with density, velocity, pressure, internal energy, and transverse magnetic field ρ , V , P , U , B , and ρ_0 , V_0 , P_0 , U_0 , B_0 , respectively. $\bar{\Lambda}$ is the mean cooling rate of the plasma over the time step. As set out in DS96, by choosing the subscripted flow variables as the point immediately in front of the shock, the equations can be reduced to a quadratic expression for the flow velocity. By choosing appropriate fractions of the geometric mean of the plasma timescales, the physical conditions in the plasma can be followed smoothly.

$$\rho v = \rho_0 v_0 \quad (1)$$

$$\rho v^2 + P + \frac{B^2}{8\pi} = \rho_0 v_0^2 + P_0 + \frac{B_0^2}{8\pi} \quad (2)$$

$$\frac{B}{\rho} = \frac{B_0}{\rho_0} \quad (3)$$

$$\frac{v^2}{2} + U + \frac{P}{\rho} + \frac{B^2}{4\pi} + \bar{\Lambda}(t - t_0) = \frac{v_0^2}{2} + U_0 + \frac{P_0}{\rho_0} + \frac{B_0^2}{4\pi} \quad (4)$$

The main calculation to be performed at each time step in these shock models is that of the ionization balance and the corresponding mean cooling rate, $\bar{\Lambda}$. The cooling and radiative emission is calculated using a very large atomic data set which allows treatment of all ionization stages of cosmically abundant elements up to fully ionized nickel. Using this atomic data set, the rate equations for non-equilibrium ionization, recombination, excitation, and radiative transfer and cooling are solved at each time step of the flow. Details of the various collisional and radiative processes included in MAPPINGS are described in Sutherland et al. (1993).

Modeling of all fast radiative shocks is necessarily an iterative process because the detailed structure of the shock depends on the ionization state of the precursor gas entering the shock front. To calculate a fully self-consistent model of a radiative shock a number of iterations are required. Firstly an initial shock model is calculated using an estimate of the ionization state of the precursor. Then the photoionized precursor is calculated using the ionizing radiation field generated by the shock. This process is then repeated, updating the ionization state of the precursor gas at each iteration. The models presented here employ four such iterations, which was found to be sufficient to allow the temperature and ionization state of the precursor gas to stabilize at a constant value.

In the final iteration of each model, the computation of the shock structure is allowed to proceed until the gas

² <http://www.ifa.hawaii.edu/~kewley/Mappings>

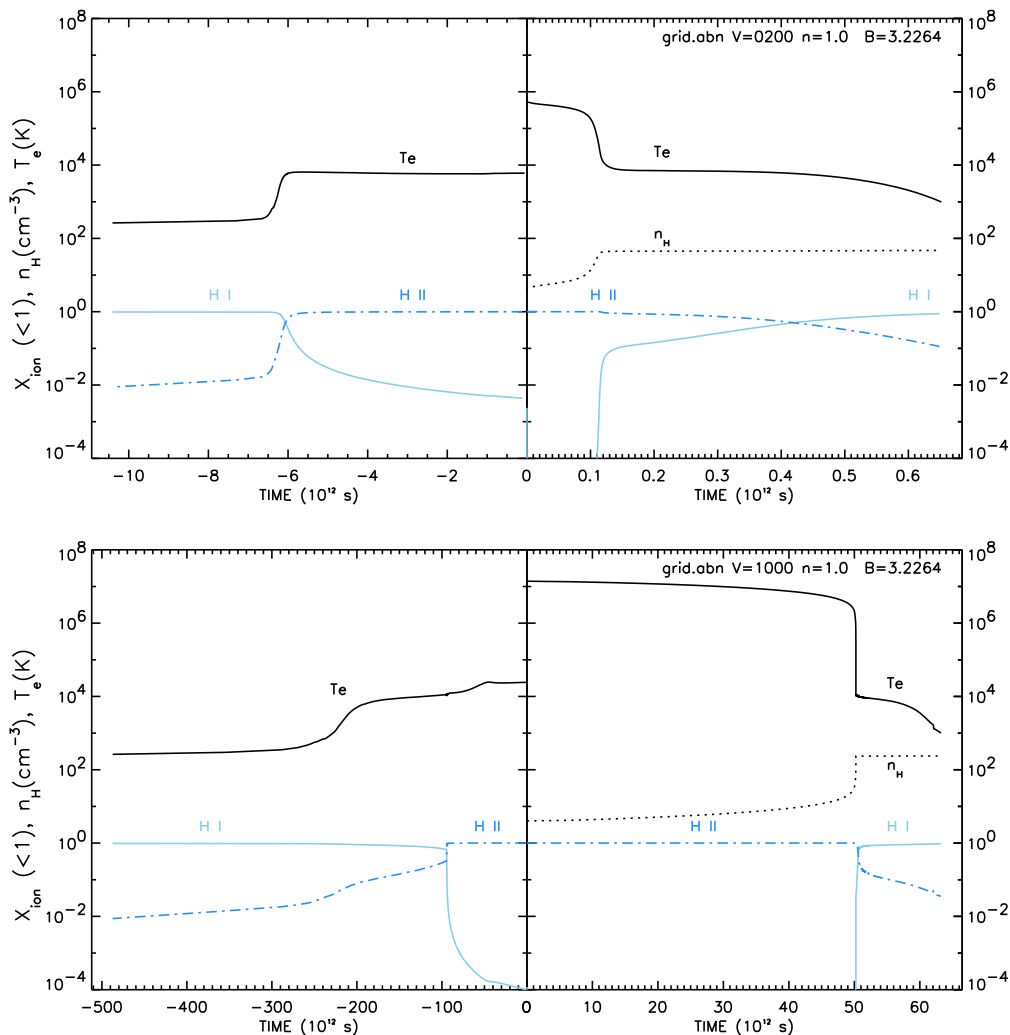


FIG. 4.— The hydrogen ionization structure, temperature profile and density profile of a shock and precursor for models with shock velocities of $v_s = 200$ and 1000 km s^{-1} and equipartition magnetic field. The axes are as described in Figure 3. See the electronic edition of the Journal for a color version of this figure.

has cooled to 1000 K , below which no further significant emission in the considered species is produced. The computation of the precursor structure is terminated when the ionized fraction of hydrogen falls to below 1 percent.

Precursor components were computed for each individual model, in contrast to DS96 who computed precursors only for each value of the shock velocity. The precursor ionization does not generally depend on the magnetic parameter but here we chose to compute each individual precursor to ensure full self consistency between the shock and its precursor.

2.1. Model Grid Input Parameters

Each individual model in our shock library is defined by five physical parameters; the pre-shock density, n , the shock velocity, v_s , the pre-shock transverse magnetic field, B and the set of atomic abundances. The library itself is organized into two main groups of model grids:

- First, complete grids of models calculated for five different atomic abundance sets; (depleted) Solar and $2 \times \text{Solar}$ as used by DS96 and which are based upon the older Anders & Grevesse (1989) abundance set; a Solar abundance set based upon the

Asplund, Grevesse & Sauval (2005) abundances as listed in Dopita et al. (2005), which is referred to here as the ‘dopita2005’ abundances; and an LMC and an SMC abundance set as given by Russell & Dopita (1992). The abundances of the individual elements (by number with respect to hydrogen) are listed for each of these abundance sets in Table 1. Each of these model grids assume a fixed pre-shock density of $n=1 \text{ cm}^{-3}$, and consists of a set of models with shock velocities covering the range 100 up to 1000 km s^{-1} in steps of 25 km s^{-1} , and magnetic fields of 10^{-4} , 0.5, 1.0, 2.0, 3.23, 4.0, 5.0 and $10.0 \mu\text{G}$. As the pre-shock density is unity, the corresponding magnetic parameters are $B/\sqrt{n} = 10^{-4}$, 0.5, 1.0, 2.0, 3.23, 4.0, 5.0 and $10.0 \mu\text{G cm}^{3/2}$.

- Second, grids of models with solar abundance (as used by DS96), calculated for densities of 0.01, 0.1, 1.0, 10, 100 and 1000 cm^{-3} . As with the first set, each of these model grids covers shock velocities of 100 up to 1000 km s^{-1} in steps of 25 km s^{-1} , and have the same magnetic parameters of 10^{-4} , 0.5, 1.0, 2.0, 3.23, 4.0, 5.0 and $10.0 \mu\text{G cm}^{3/2}$. However, as the magnetic field values required to obtain

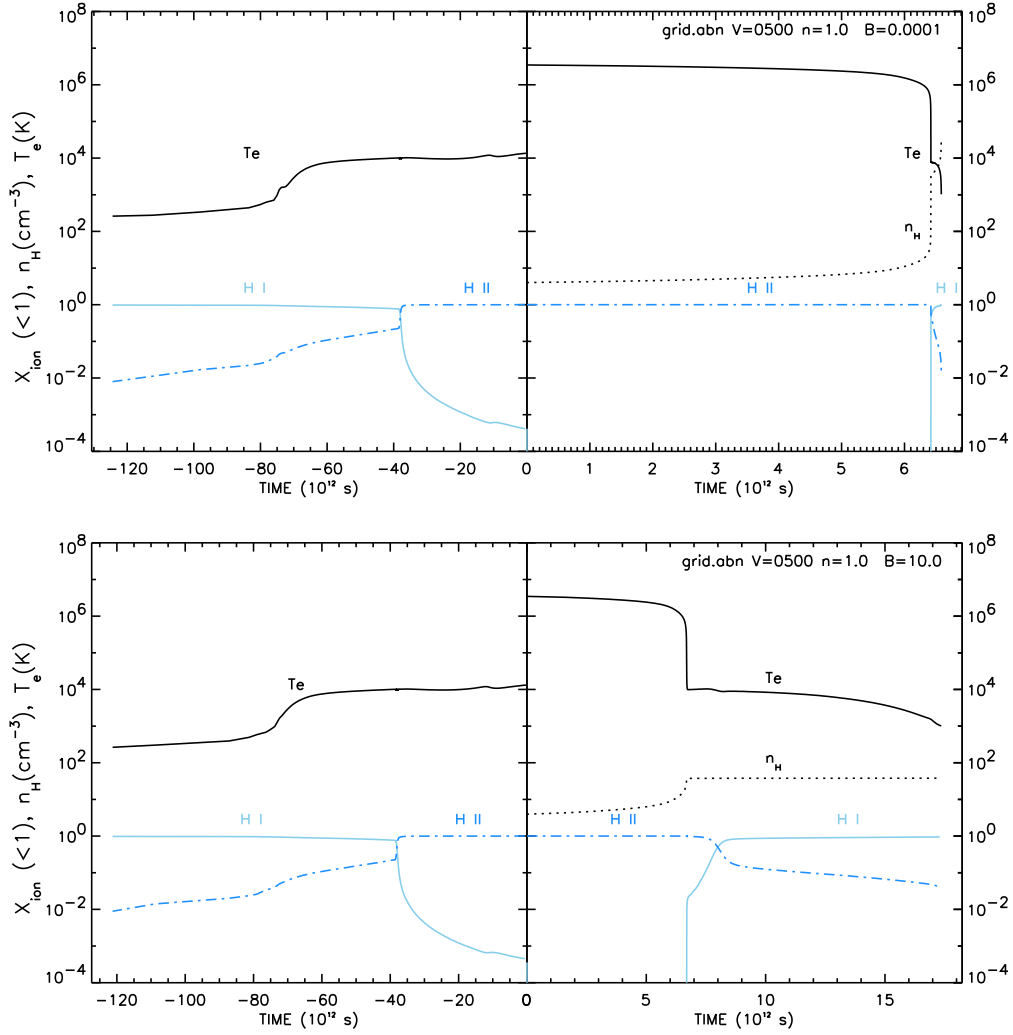


FIG. 5.— The hydrogen ionization structure, temperature profile and density profile of models with different magnetic parameter. Models of $v_s = 500 \text{ km s}^{-1}$ are shown for the magnetic parameters of 0.0001 and $10 \mu\text{G cm}^{3/2}$. The axes are the same as for Figure 3. See the electronic edition of the Journal for a color version of this figure.

these magnetic parameters are of course different for each density, additional models were computed in order to be able to also compare models of different densities with the same transverse magnetic field. These are $B \sim 10^{-3}$, $\sim 10^{-2}$, $\sim 10^{-1}$, 1.0, 10 and $100 \mu\text{G}$, calculated for each density.

The magnetic field, B , and magnetic parameter, B/\sqrt{n} , values are chosen so as to cover the extremes expected in the ISM, while also sampling more finely the magnetic field strengths which are near equipartition. Under equipartition conditions the magnetic pressure is equal to the thermal pressure, and the Alfvén speed is approximately equal to the gas sound speed. Pressure equipartition occurs for $B_0^2/4\pi \sim n_0 k T_0$ where B_0 is the transverse magnetic field, and n_0 , T_0 are the pre-shock densities and temperatures (Dopita & Sutherland 2003). This condition is satisfied for magnetic parameters $B/\sqrt{n} \sim 3 - 5$. The value $B/\sqrt{n} \sim 3.23$ was chosen as the nominal equipartition value.

The input parameters for the all of the models are provided in Table 3. Each row of the table represents a velocity sequence of models at a given abundance, density and magnetic field. The table is organized into ten sets

of models. The first five sets of models represent the model grids for the five different abundances, and the following 5 sets of models are the solar abundance models for different input densities and magnetic fields. The number and range of model input parameters allows the construction of various 2-D, or higher dimensional, grids of models.

3. IONIZING RADIATION GENERATED BY THE SHOCK

The ionizing radiation produced in the cooling zone behind the shock front shock is mostly composed of thermal bremsstrahlung (free-free) continuum and resonance lines arising from many different elements and ionic stages. The underlying exponential shape of the continuum is emphasized in Figure 1 where we show the ionizing spectra generated in the $n=1.0 \text{ cm}^{-3}$ solar abundance shock models. As can be seen, higher velocity shocks result in harder and more luminous ionizing spectra, with the spectral slope in the log-linear plot clearly flattening with increasing velocity. Note that the histogram nature of the figure also reveals the high energy (frequency) resolution of the MAPPINGS spectral vector. Figure 2 shows the ionizing spectra of 400 and 1000 km s^{-1} shocks on a νF_ν scale, illustrating both

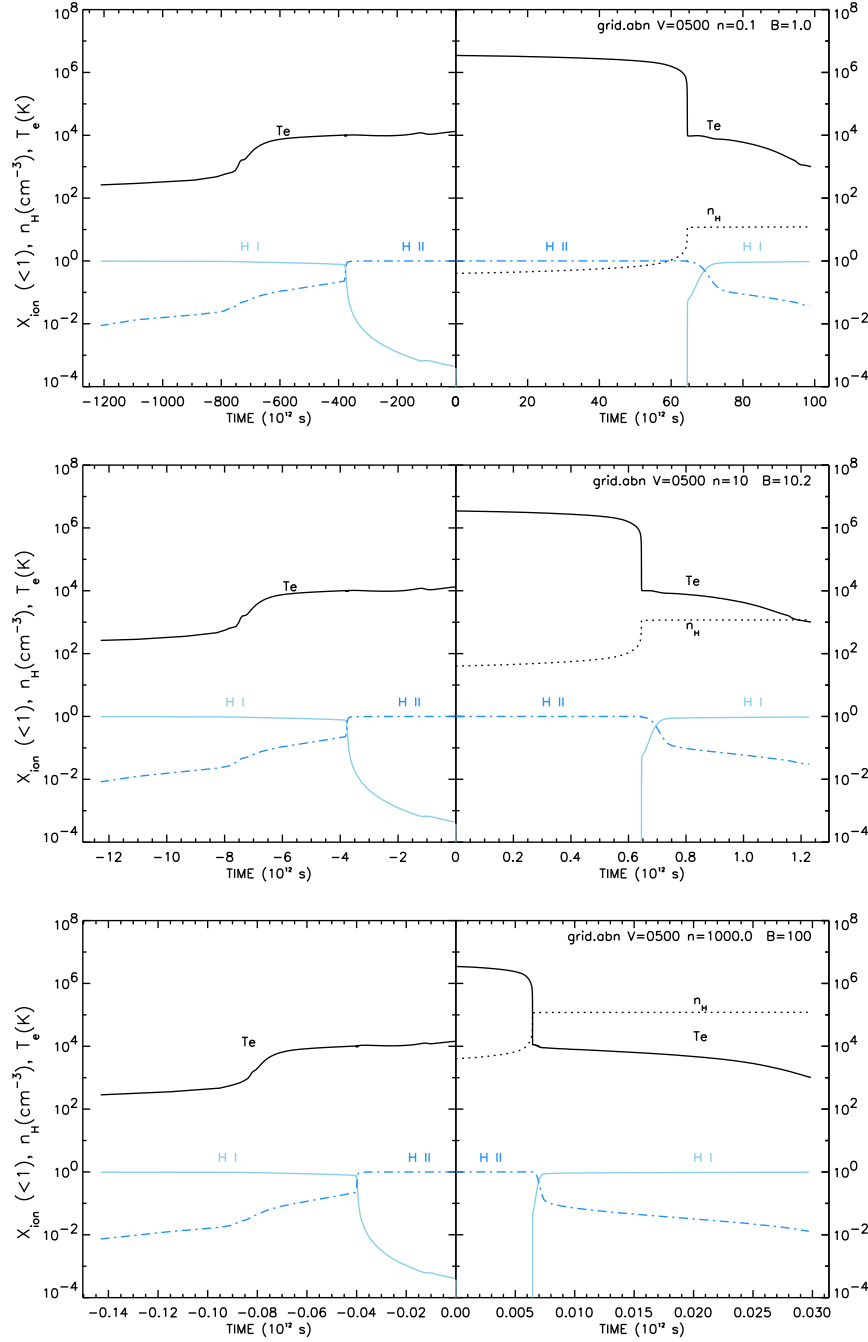


FIG. 6.— The hydrogen ionization structure, temperature profile and density profile of models with different pre-shock density. Models of $v_s = 500 \text{ km s}^{-1}$ and equipartition magnetic field are shown for pre-shock densities of 0.1, 10 and 1000 cm^{-3} . The axes are the same as for Figure 3. See the electronic edition of the Journal for a color version of this figure.

the stronger UV fluxes and harder X-ray spectra generated in high velocity shocks. This figure also shows a prominent low-temperature bound-free continuum of hydrogen, produced in the cool, partially-ionized zone of the recombination region of the shock, and the strong hydrogen two-photon continuum produced mostly by the down-conversion of Ly α photons trapped in this same region of the shock structure. Also present, though to a much weaker scale, is the bound-free continuum arising from the heavier elements, with the helium continuum the most obvious.

The strength of the ionizing field is a strong function of the shock velocity, but does not significantly depend

on either the atomic abundance or the magnetic field. This is because the ionizing field is dominated by the bremsstrahlung radiation, whose strength is controlled by the temperature and density of the radiative zone, which is determined by the shock velocity and pre-shock density. As magnetic field support in this cooling zone is negligible, it has little effect on the emission, and, as hydrogen dominates both electron and ion numbers for both the bremsstrahlung and free-bound emission, changes in metallicity have only a small impact.

The hydrogen ionizing radiation flux, L_{UV} , integrated for all energies $h\nu > 13.6 \text{ eV}$, and over $2\pi \text{ sr}$ is listed in Table 2. It is found to scale almost exactly as the

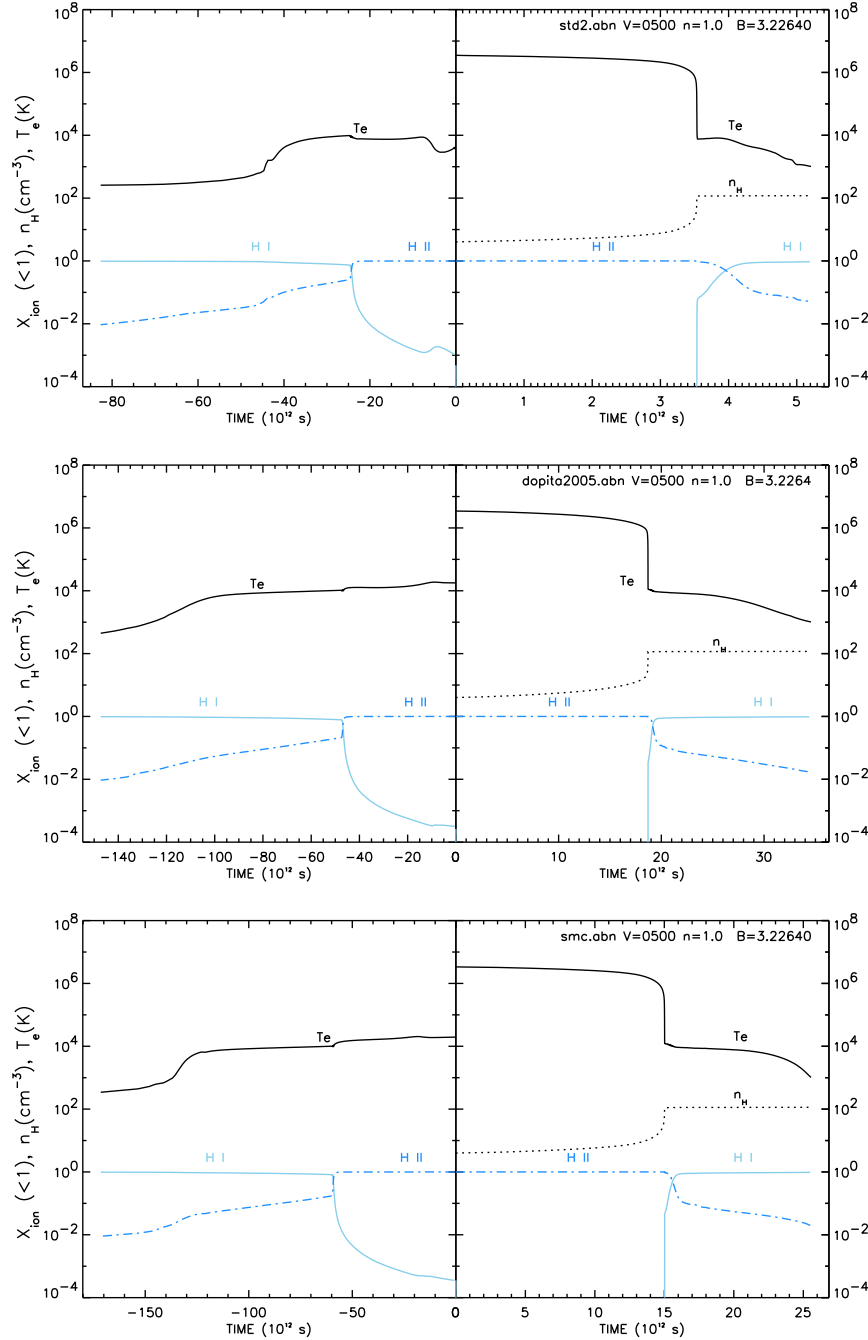


FIG. 7.— The hydrogen ionization structure, temperature profile and density profile of models with different atomic abundances. Models of $v_s = 500 \text{ km s}^{-1}$ and equipartition magnetic field are shown for the 2×solar, dopita2005 and SMC abundance sets. The axes are the same as for Figure 3. See the electronic edition of the Journal for a color version of this figure.

available enthalpy as:

$$L_{UV} = 2.44 \times 10^{-4} \left(\frac{v_s}{100 \text{ km s}^{-1}} \right)^{3.02} \times \left(\frac{n}{\text{cm}^{-3}} \right) \text{ ergs cm}^{-2} \text{ s}^{-1} \quad (5)$$

The ionizing fields may also be characterized in terms of their ionization parameter in the pre-shock gas. As in DS96 we give ionization parameters, Q , defined as the mean number of photons passing through unit area divided by the total pre-shock particle density; $Q = N_{\text{photons}}/n_T \text{ (cm s}^{-1}\text{)}$. Table 2 lists Q in the H I-ionizing $13.6 < h\nu < 24 \text{ eV}$ band, $Q(\text{H})$, the He I-ionizing $24 < h\nu < 54 \text{ eV}$ band, $Q(\text{HeI})$, and the He II-ionizing

band $h\nu > 54 \text{ eV}$, $Q(\text{HeII})$ as a function of shock velocity. We also provide the corresponding R -Type ionization front velocity v_{ion} and the equilibrium electron temperatures, T_e just ahead of the shock front.

4. SHOCK AND PRECURSOR STRUCTURES

We now consider the ionization structures and the physical scales of both the shock and precursor components. Figure 3 shows the ionized and neutral hydrogen structures (as labelled) of the shock and precursor components of the 500 km s^{-1} solar abundance model, along with the hydrogen density and electron temperature profiles. Note that the hydrogen density is not plot-

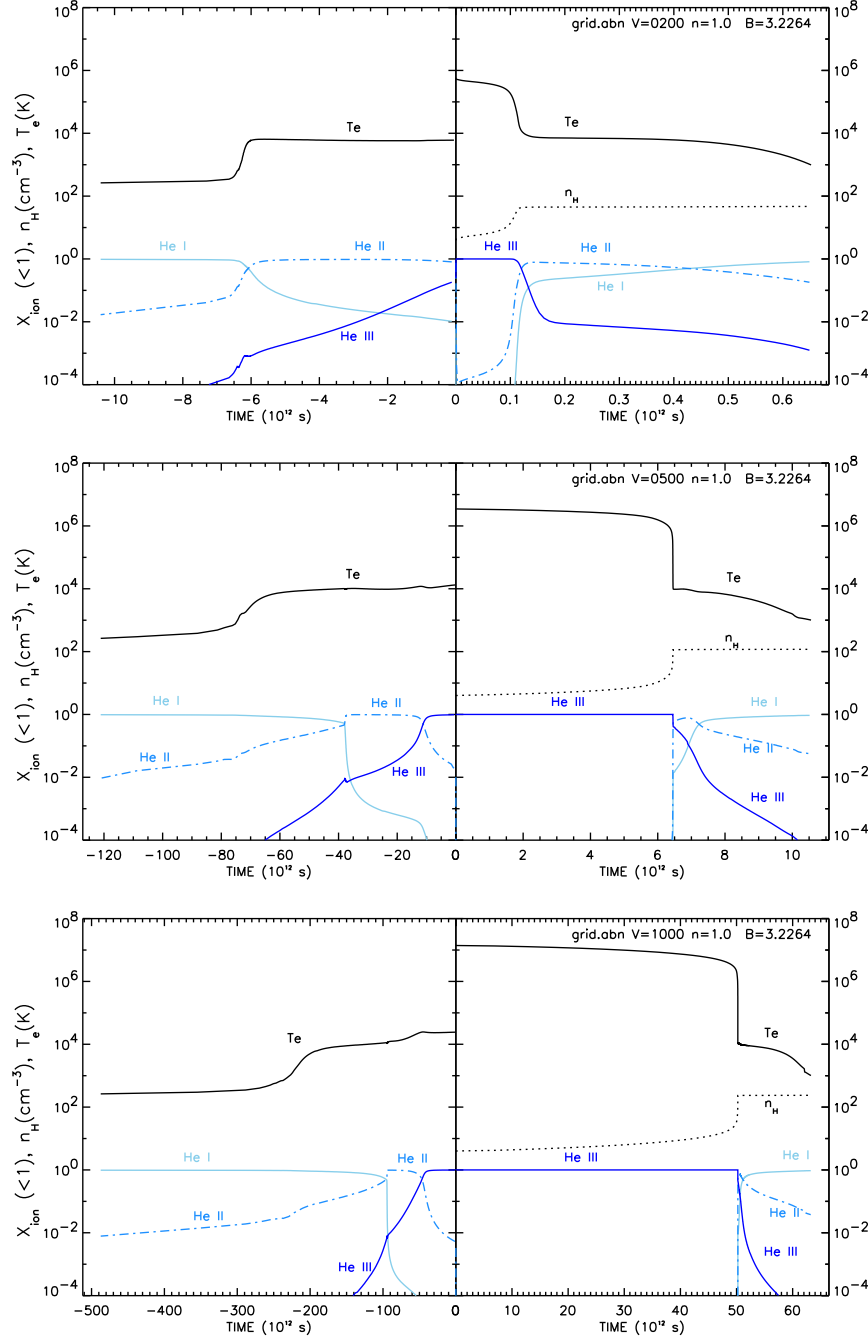


FIG. 8.— The helium ionization structure, temperature profile and density profile of models with solar abundance, equipartition magnetic field for shock velocities of $v_s = 200, 500$, and 1000 km s^{-1} . The axes are the same as for Figure 3. See the electronic edition of the Journal for a color version of this figure.

ted within the precursor region as it is set at the constant value of $n_H = 1.0 \text{ cm}^{-3}$. The profiles are plotted in the frame of the shock front, considered with respect to the time axis. This axis represents time since (or prior to) the passage of the shock front, and can be converted into a physical distance from the shock front via the shock velocity.

In Figure 3 (and subsequent ionization structure Figures 4–12), the structure of the precursor is shown in the left panel and the shock structure is shown in the right panel. The shock front is located at time $t = 0$. The time taken to reach equipartition in the electrons, ions, and un-ionized gas is assumed to be negligible, so that

the shock is therefore unresolved and the density and electron temperature jump discontinuously at the shock front. Note also that the time axes are shown in units of 10^{12}s , but the scales and ranges are necessarily different for the shock and precursor panels of these diagrams, as well as between the diagrams with different parameters.

As described in DS96 a number of zones can be identified in the shock structures. These are indicated in Figure 3 and are, respectively:

1. *The ionization region.* This region, just after the shock front, is in an ionization state below that appropriate for the electron temperature assuming

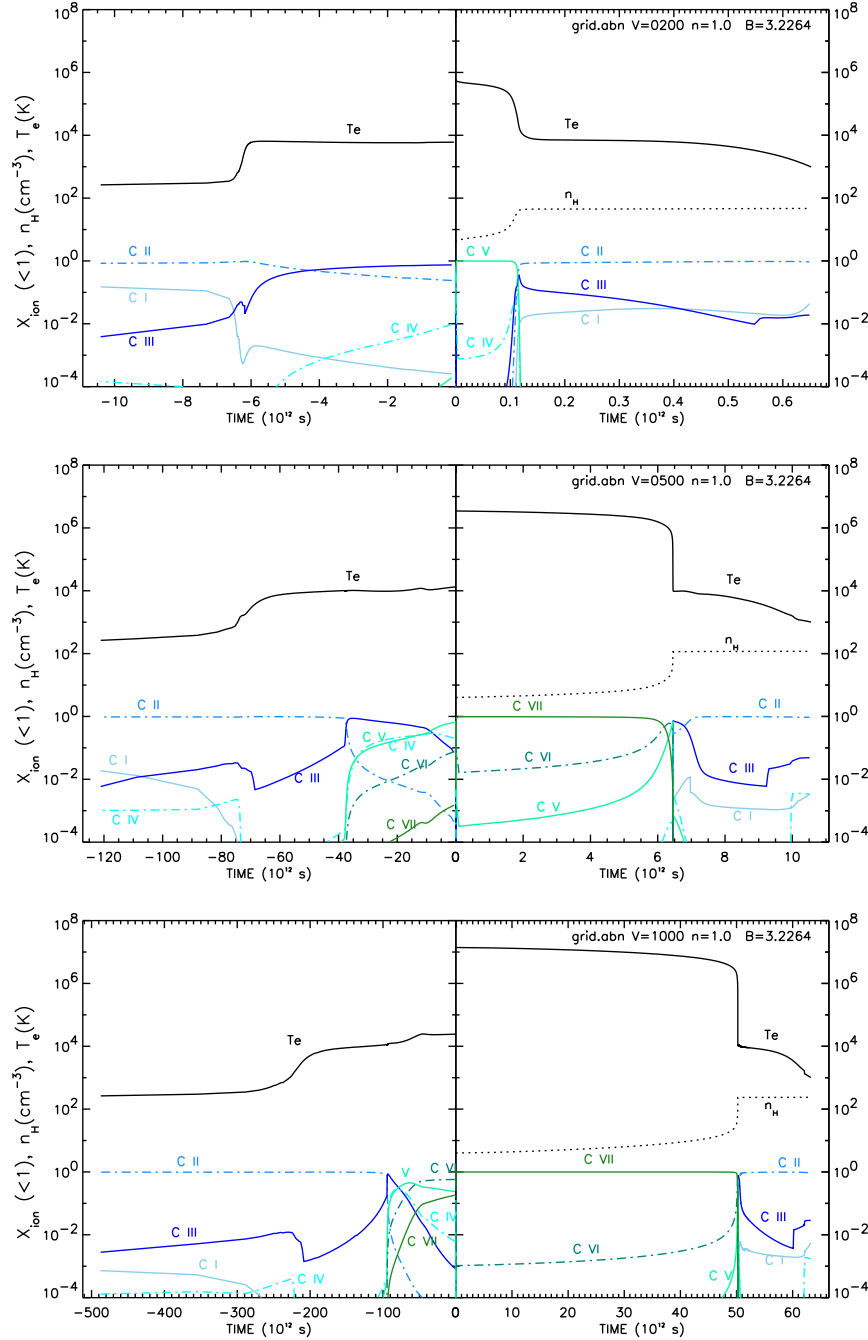


FIG. 9.— The carbon ionization structure, temperature profile and density profile of models with solar abundance, equipartition magnetic field for shock velocities of $v_s = 200, 500$, and 1000 km s^{-1} . The axes are the same as for Figure 3. See the electronic edition of the Journal for a color version of this figure.

collisional ionization equilibrium (CIE), due to discontinuous temperature jump at the front. After the passing of the front, the gas rapidly (barely resolved in the figures) adjusts from the pre-shock ionization state to the appropriate CIE state for the post-shock temperature. The rate at which it adjusts depends upon the collisional ionization rates of these species. As discussed in DS96, this region has strong line emission due to this state of high temperature and relatively low-ionization.

2. *The high temperature radiative zone.* This is the zone in which most of the EUV and soft X-ray flux

is emitted. The ionization state is approximately in coronal equilibrium for the temperature of the region. Even though the cooling rate of this region is low due to the high temperature, it is the dominant contributor to the radiation field of the shock, assisted by the high-ionization, optically-thin state of the gas.

3. *The non-equilibrium cooling zone.* Once the temperature of the post shock gas drops below $\sim 10^6 \text{ K}$, the cooling rate becomes very high and the recombination timescales of a large number of ions becomes longer than the local cooling timescale. As

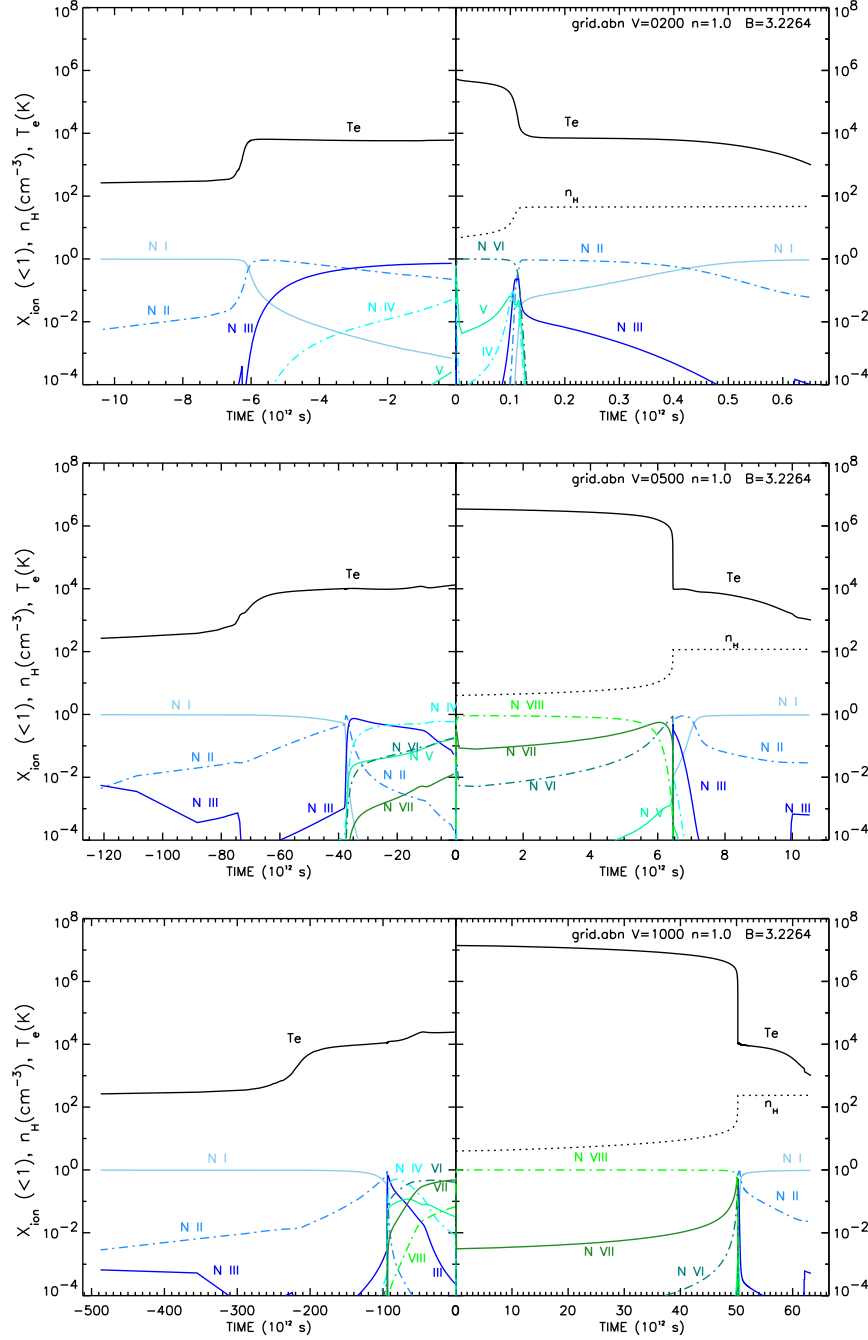


FIG. 10.— The nitrogen ionization structure, temperature profile and density profile of models with solar abundance, equipartition magnetic field for shock velocities of $v_s = 200, 500$, and 1000 km s^{-1} . The axes are the same as for Figure 3. See the electronic edition of the Journal for a color version of this figure.

a result, the ionization state lags and the plasma is in a higher degree of ionization than collisional ionization equilibrium would suggest. The relatively high ionization state for the temperature means that the collisional line emission is weak for these intermediate ionization species, and that the gas remains optically thin to the diffuse radiation of the previous region.

4. *The super-cooled zone* is the region where photoionization starts to become important in determining the ionization balance. Initially, however, the ionization state is still too high to efficiently absorb

the ionizing photons. This leads to an over-cooling, and the temperature falls below the value given by photoionization equilibrium. The width of this region is dependent upon both the recombination and photoionization timescales of the ions.

5. *The photoabsorption and recombination zone.* This is essentially an equilibrium plane-parallel H II region illuminated by the downstream EUV photon field. The density in this region is much higher than the pre-ionized region ahead of the shock, so that the effective ionization parameter in this zone is much lower, and the H II region is very much thin-

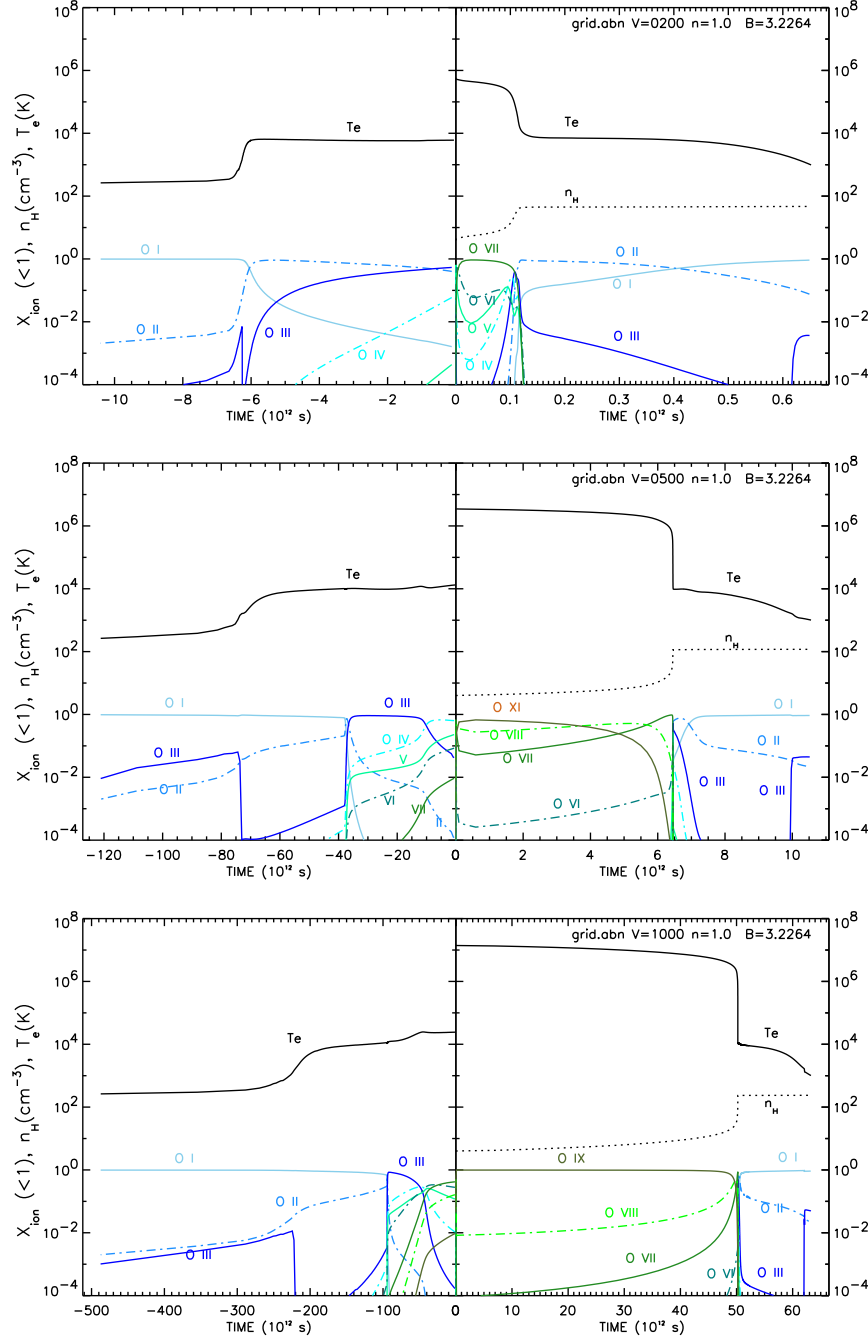


FIG. 11.— The oxygen ionization structure, temperature profile and density profile of models with solar abundance, equipartition magnetic field for shock velocities of $v_s = 200, 500$, and 1000 km s^{-1} . The axes are the same as for Figure 3. See the electronic edition of the Journal for a color version of this figure.

ner. Eventually the EUV photons are absorbed, and hydrogen finally recombines. However, there is a cool, partially ionized region behind the main recombination front. This has a temperature of a few thousand degrees, and is ionized by the hard penetrating X-rays which undergo Auger processes and these lead to the emission of fast electrons which in turn produce secondary ionization cascades.

4.1. Hydrogen ionization structures

Figures 4 - 7 show, respectively, the effects of changing velocity, magnetic field, pre-shock density and abun-

dance on the structures of the hydrogen ionization fraction, hydrogen number density, n_H , and the electron temperature, T_e , in the shock and precursor regions. Note that in each diagram the time scale changes due to the effects of the changing parameters. In each diagram the parameters of the model (abundance set, velocity, density, and magnetic field respectively) are listed in the top right corner for clarity.

The dominant parameter of the shock (and precursor) structure and emission is the velocity, as is seen in Figure 4. This figure shows our fiducial $n = 1.0 \text{ cm}^{-3}$, $B/\sqrt{n} = 3.23 \text{ } \mu\text{G cm}^{3/2}$, solar abundance model with two velocities; $v_s = 200$ and 1000 km s^{-1} (three includ-

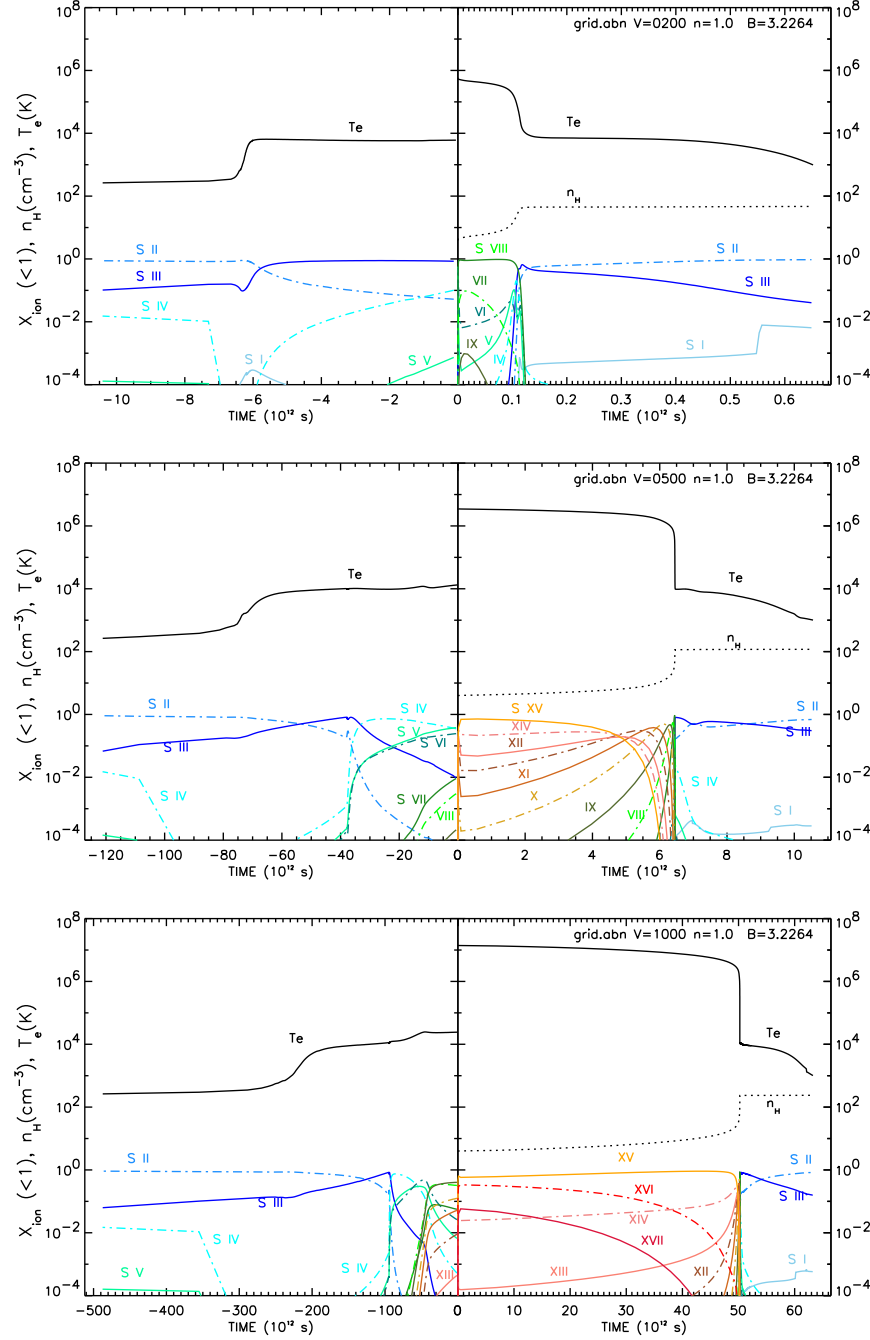


FIG. 12.— The sulfur ionization structure, temperature profile and density profile of models with solar abundance, equipartition magnetic field for shock velocities of $v_s = 200, 500$, and 1000 km s^{-1} . The axes are the same as for Figure 3. See the electronic edition of the Journal for a color version of this figure.

ing the $v_s = 500 \text{ km s}^{-1}$ shown in Figure 3). There is a clear increase of both the extent and temperature of the radiative zone as the velocity increases due to the greater shock strength, leading to the changes in the ionizing radiation field shown in Figures 1 and 2. This increase of both the hardness and luminosity of the radiation field leads to the greater extent and ionization in the precursor region, visible through the increased temperature in this figure and the higher ionization species seen in Figures 8–12. The increased radiation field also affects the ionization of the post-shock recombination region. This is mollified somewhat however by the density increase associated with the faster shock, which leads to a smaller

increase in the ionization parameter, though the effects of the harder radiation are still visible.

Figure 5 shows models with $n=1.0 \text{ cm}^{-3}$, $v_s = 500 \text{ km s}^{-1}$, and solar abundance for differing magnetic fields. The top panel shows a model with the magnetic parameter set to $B/\sqrt{n} = 0.0001 \mu\text{G cm}^{3/2}$, and the bottom panel has $B/\sqrt{n} = 10.0 \mu\text{G cm}^{3/2}$, which can be compared with the equipartition model with $B/\sqrt{n} = 3.23 \mu\text{G cm}^{3/2}$ model in Figure 3. In all three cases the precursor structure is almost unchanged, as the radiation field and luminosity arising from the shock are little affected by changes in B (except at extremely high values), as dis-

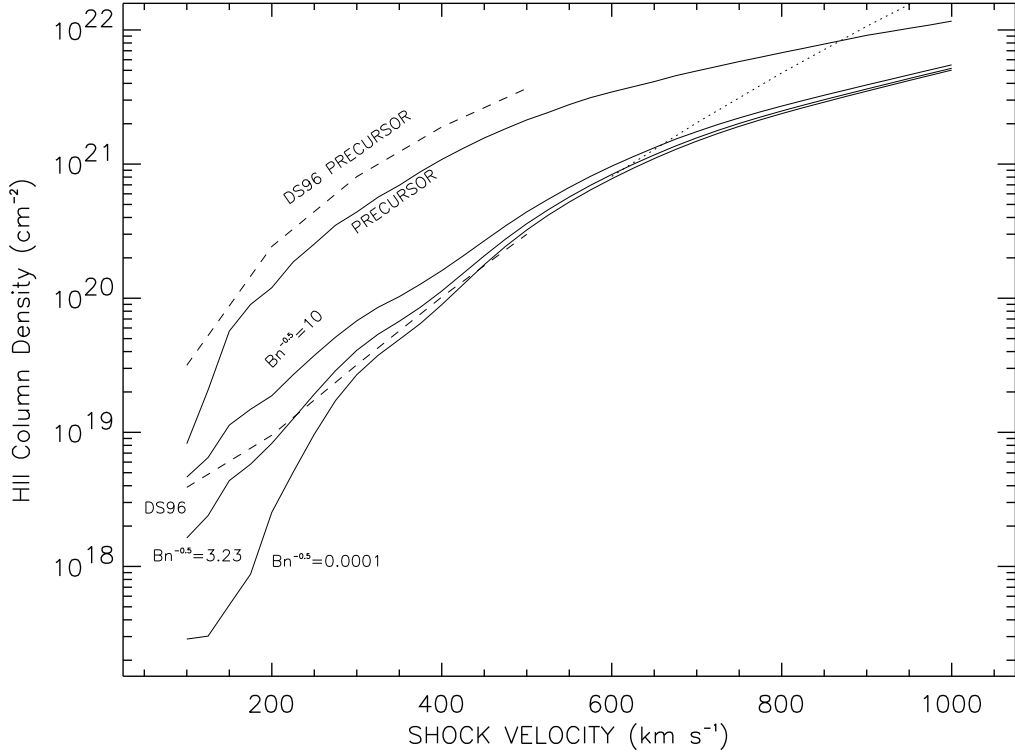


FIG. 13.— Integrated hydrogen column densities for the shock and the precursor structures. The column densities of the shock structure are shown for magnetic parameters $B/\sqrt{n}=0.0001, 3.23$ and 10 . The curve labelled ‘PRECURSOR’ shows the column density of the precursor gas which does not depend on the magnetic parameter. The dashed curves show the shock and precursor column densities for the DS96 models, and the dotted curve shows the extrapolation of the column density scaling relation for the shock column density of DS96.

TABLE 2
SHOCK IONIZING PROPERTIES

v_s (km s ⁻¹)	L_{UV} (ergs cm ⁻² s ⁻¹)	$Q(\text{H I})$ (km s ⁻¹)	$Q(\text{He I})$ (km s ⁻¹)	$Q(\text{H II})$ (km s ⁻¹)	v_{ion} (km s ⁻¹)	T_e (K)
200	8.041E-4	209.1	43.0	4.9	214.2	7033
300	3.519E-3	430.8	312.1	83.1	688.3	10288
400	9.106E-3	664.3	598.7	513.2	1480.0	12145
500	1.751E-2	985.2	1195.0	602.2	2318.3	15435
600	2.968E-2	1158.2	1628.2	800.7	2989.2	18486
700	4.631E-2	1559.2	1986.0	1094.0	3865.8	20516
800	6.815E-2	1958.8	2362.3	1542.7	4885.8	21934
900	9.645E-2	2375.0	2920.4	2206.6	6251.7	23389
1000	1.318E-1	2740.6	3262.7	2786.8	7325.0	24760

cussed in sections §3 and §4.4. The insensitivity of the radiation field to B can be seen in this figure through the similarity of the radiative zone between the models. This similarity, a result of the insensitivity of the temperature jump to the magnetic field, means that the ionizing bremsstrahlung radiation that dominates the energetics is practically the same. However, what is sensitive to the transverse magnetic field is the density in the recombination zone behind the shock front. As discussed in DS96, the maximum compression in this post-shock region is driven by the ratio of the post- to pre-shock magnetic fields. Thus a higher initial magnetic field results in a lower density post-shock gas, and therefore, given the similarity in radiation field, a higher effective post-shock ionization parameter. This results in a significantly different ionization and emission structure in the post-shock gas, leading to the strong diagnostics seen in DS95 and

in this work (§5).

Figure 6 shows the effect of changing the pre-shock density. We plot our fiducial solar abundance models, with $v_s = 500$ km s⁻¹ and $B/\sqrt{n} = 3.23$ $\mu\text{G cm}^{3/2}$, for each of the densities $n=0.1, 10$, and 1000 cm⁻³, from top to bottom (with the $n=1.0$ cm⁻³ case shown in Figure 3). Note that the magnetic field, B , is also varied in order to keep the magnetic parameter constant for the models shown. This figure demonstrates that at a given shock velocity, the region influenced by the shock scales with density (to the extent that collision de-excitation effects are unimportant), proving explicitly that to first order the product $n_0 t$ is an invariant with changing density, as asserted by DS96.

Changes in the atomic abundances directly affect the cooling rate. Figure 7 shows the equipartition case,

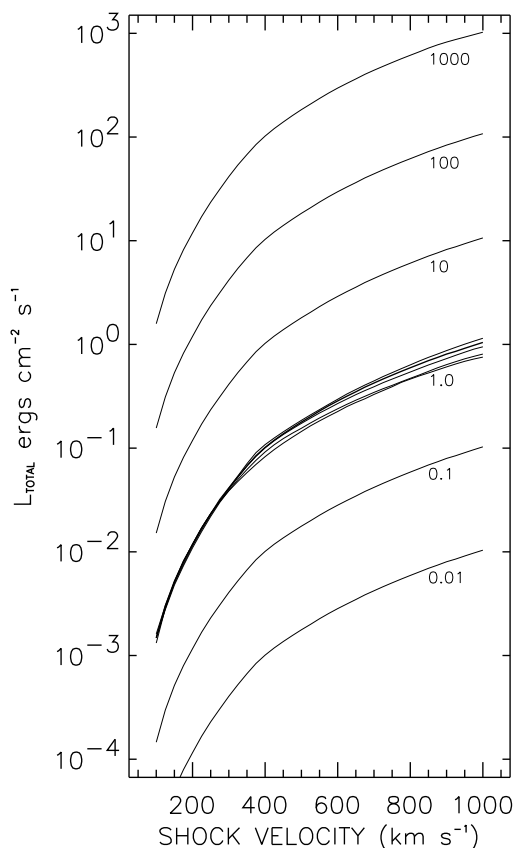


FIG. 14.— Total radiative fluxes of shocks as a function of shock velocity and various values of the pre-shock densities. The bold line is for the standard model having a solar abundance set, a density $n = 1 \text{ cm}^{-3}$, and an equipartition pre-shock magnetic field. The thinner lines near the bold line show the luminosities of the $n = 1 \text{ cm}^{-3}$, equipartition models with abundances of twice solar, LMC and SMC abundance sets.

$B/\sqrt{n} = 3.23 \mu\text{G cm}^{3/2}$, with $n = 1.0 \text{ cm}^{-3}$ and $v_s = 500 \text{ km s}^{-1}$ for models using the 2×Solar, dopita2005, and SMC abundances. All three models differ in structure, with the expected clear progression in cooling efficiency as we increase in metallicity from the SMC abundances to the twice Solar. This difference in efficiency leads to the changes visible in the spatial and temporal extent of the models, in both the precursor and shock regions. The changes in metallicity also affect the ionizing radiation from the shock due to the weakening of the heavy element free-bound features. However, as discussed in section 3, the effect is minimal.

4.2. Ionization Structures of Abundant Elements

The shock model library includes the full fractional ionization structure of all elements listed in Table 1. In Figures 8–12 we show the ionization structures of helium, carbon, nitrogen, oxygen and sulfur for three velocities (200, 500 and 1000 km s^{-1}) of the solar abundance,

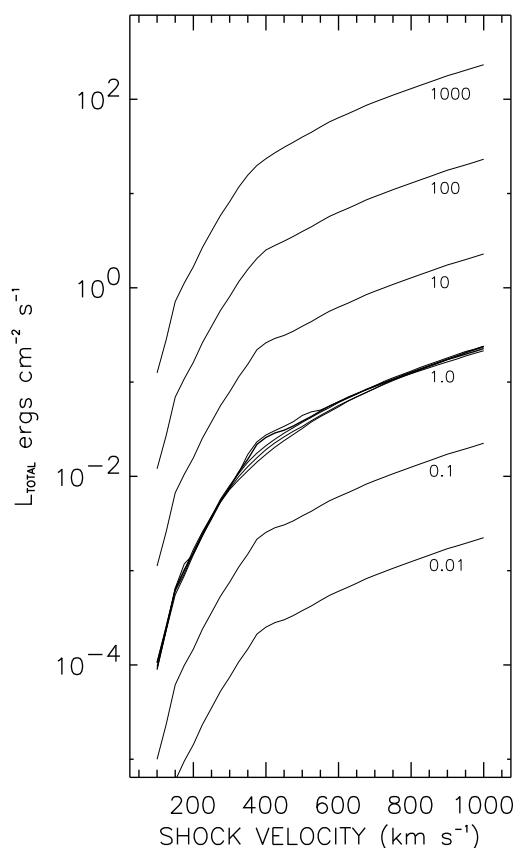


FIG. 15.— As for Figure 14, but showing the precursor total radiative fluxes.

$n = 1.0 \text{ cm}^{-3}$ models with the equipartition magnetic parameter. The associated hydrogen structures are shown in Figures 3 and 4. In each figure, the ionization fraction, X_{ion} , is shown at the bottom (with values ≤ 1), with each ionization state labelled and the odd and even ionization states shown as the solid and dot-dashed curves respectively for clarity. Also included in each diagram is the hydrogen density, n_{H} , and electron temperature structure, T_e , to trace the different shock and precursor zones.

Together, these figures elucidate further what has been discussed in the previous sections; faster shocks lead to a higher temperature, and therefore higher ionization, radiative zone. This in turn leads to a more luminous and harder ionizing spectrum as can be traced within the precursor zone. Similarly this figure allows one to trace the more complex ionization structure of the post-shock recombination region, affected both by the increased ionizing spectrum and increased density that results from faster shocks.

However the true strength of these figures, and the library in general, is their diagnostic ability, allowing the reader to trace exactly where each ionization state arises,

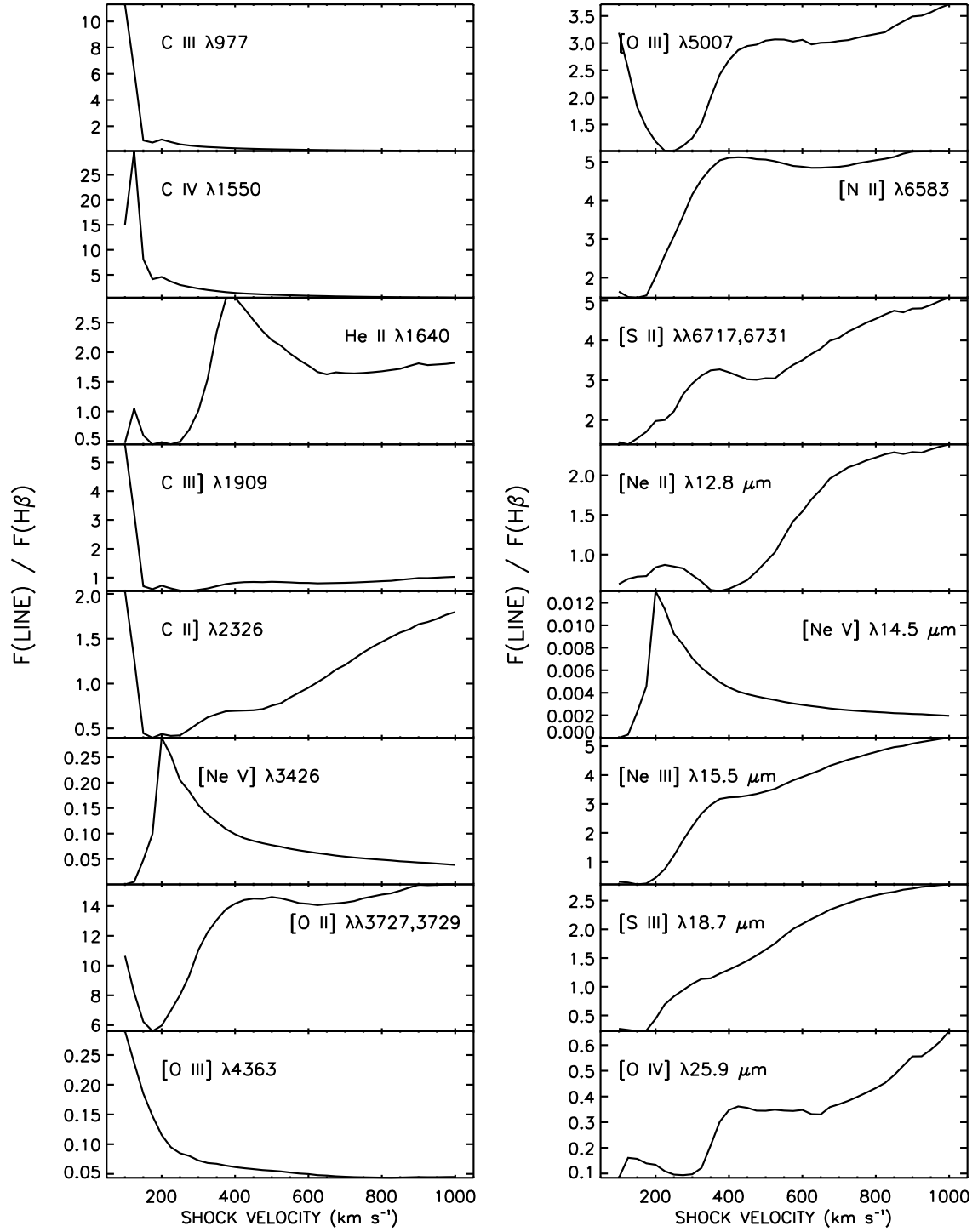


FIG. 16.— Line strength relative to $\text{H}\beta$ for 16 strong emission lines between the Lyman Limit and $26\mu\text{m}$ as a function of shock velocity. These are computed for the shock component only, and are for the fiducial model with solar abundance, $n = 1.0 \text{ cm}^{-3}$ and $B = 3.23 \mu\text{G}$.

which is especially interesting given the X-ray ionized regions that occur far from the ionization front in both the precursor and post-shock regions.

4.3. Column Densities

The column densities of the shock and precursor components of the models inevitably increase with shock velocity, and can be as large as $N(\text{H})=4 \times 10^{21} \text{ cm}^{-2}$ in the shock itself for the highest velocity solar models. The precursor column densities range from between 3 and 20 times larger than the corresponding shock component, with this ratio decreasing for the higher velocity shocks.

Figure 13 displays the integrated H II column density of the shock as a function of shock velocity. This is shown for the solar abundance $n=1.0 \text{ cm}^{-3}$ models with equipartition magnetic parameter, as well as the for maximum and minimum magnetic parameters of 0.0001 and 10.0. The dashed line shows the scaling relation given by DS96, and the dotted line shows the extrapolation of this beyond shock velocities of 500 km s^{-1} . The diagram shows a weak dependence of the column density on the magnetic parameter, and a decrease in the slope beyond shock velocities of 700 km s^{-1} .

The column density of the precursor does not depend on the magnetic parameter. All solar abundance, $n=1.0 \text{ cm}^{-3}$ models fall on the same curve, marked ‘PRECURSOR’ in Figure 13. There is however a systematic difference in the precursor column density compared to the DS96 models, with the newer models having a $\sim 10\%$ decrease in column density, consistent with the slightly lower fraction of ionizing flux compared with total flux produced in the cooling plasma in the newer models.

Tables of the column densities for all species for every library model are available on-line (see section 6). These columns are a function of both the hydrogen column density and the ionization structures seen in the previous figures. Example tables giving the column densities of the shock and precursor components of the $n=1.0 \text{ cm}^{-3}$ solar abundance models at velocities of 200, 500 and 1000 km s^{-1} models are presented in Tables 4 and 5.

4.4. Radiative fluxes of Shock and Precursor Components

A fully-radiative shock will, by definition, radiatively dissipate all of the energy flux through the shock. Thus the total radiative flux, L_{Tot} , is equal to $0.5 \rho v_s^3$. DS96 provided scaling relations for the total luminosity of a shock, and showed a similar scaling exists for the total luminosity of the precursor emission. This follows because, in the precursor, all of the radiation emitted in the pre-shock direction is eventually processed.

In Figures 14 and 15 we show the total radiative fluxes generated in the shock and in the precursor respectively, in the MAPPINGS III models with solar abundance and equipartition magnetic fields. Here we cover the full range of pre-shock density ($0.01 - 1000 \text{ cm}^{-3}$). To illustrate the relatively minor adjustments to the total radiated flux due to different abundances we also show the luminosities for the models with $2 \times \text{Solar}$, Dopita2005, SMC and LMC abundance sets for $n=1.0 \text{ cm}^{-3}$. Changing the magnetic field from the equipartition value produces too small an effect on the total radiative flux to be visible on the scale of these plots.

5. SPECTRAL SIGNATURES OF THE SHOCK AND PRECURSOR GAS

While the total luminosities of the shock effectively depends only upon the density and the shock velocity, the detailed emission line spectra depend strongly on the physical and ionization structure of the shock. This is determined primarily by the shock velocity and the magnetic parameter. However, at the higher pre-shock densities (and at lower values of the magnetic parameter) the density close to the photoionized tail and the recombination zone of the shock becomes sufficiently high for collisional de-excitation of forbidden lines to become important. In these circumstances, the emission line spectrum of the shock becomes dependent upon the density as well.

Shocks are characterized by regions of high electron temperature and ionization state. As a consequence, they display a rich spectrum of collisionally excited UV lines. The shock velocity controls the shape of the ionizing spectrum produced by the shock, and the magnetic parameter controls the effective ionization parameter in the photoionized tail of the shock. Higher ionization parameters yield a higher mean ionization in the plasma, so therefore faster shocks give an (optical) spectrum of somewhat higher ionization.

The emission line ratios (with respect to $\text{H}\beta=1$) of a selection of lines for the shock, precursor and shock+precursor components of the solar abundance, $n=1.0 \text{ cm}^{-3}$ models are shown separately in Figures 16-18 as a function of shock velocity.

As discussed before, the precursor emission can be considered as an H II region with high ionization parameter. In this region strong cooling lines, like $[\text{O III}]\lambda 5007$, are strong and generally increase in strength with shock velocity as the spectrum produced by the cooling plasma becomes harder, and its flux increases. Eventually, as the shock velocity is increased, the average state of ionization in the precursor region becomes high and the relative intensity of the lines produced by lower ionization turn over, flattening and even decreasing at the higher velocities. For example, in Figure 17 $[\text{O III}]\lambda 5007$ can be seen to flatten out around 600 km s^{-1} , and even decrease at 1000 km s^{-1} .

In addition the emission line ratios of 40 strong lines are tabulated for shock, precursor and shock+precursor in Tables 6, 7, and 8 respectively. Complete tables of emission line ratios of all lines, for all models are available electronically (see section 6).

5.1. Line Ratio Diagrams

Diagnostic emission line ratio diagrams are well established as a powerful and practical way to investigate the physics of emission line gas. At a basic level they can be used empirically to identify the key excitation mechanism, and divide active galaxies from their star-formation dominated counterparts. At a deeper level, grids of theoretical models can be used to determine chemical abundances and derive physical parameters such as electron temperature, density, ionization parameter or shock velocity. Various sets of diagnostic diagrams have been proposed and used - Baldwin et al. (1981) (optical), Veilleux & Osterbrock (1987) (optical-IR), Allen et al. (1998) (near-UV) and Groves et al. (2004b) (UV, optical, IR). These 2-D diagrams remain useful alongside

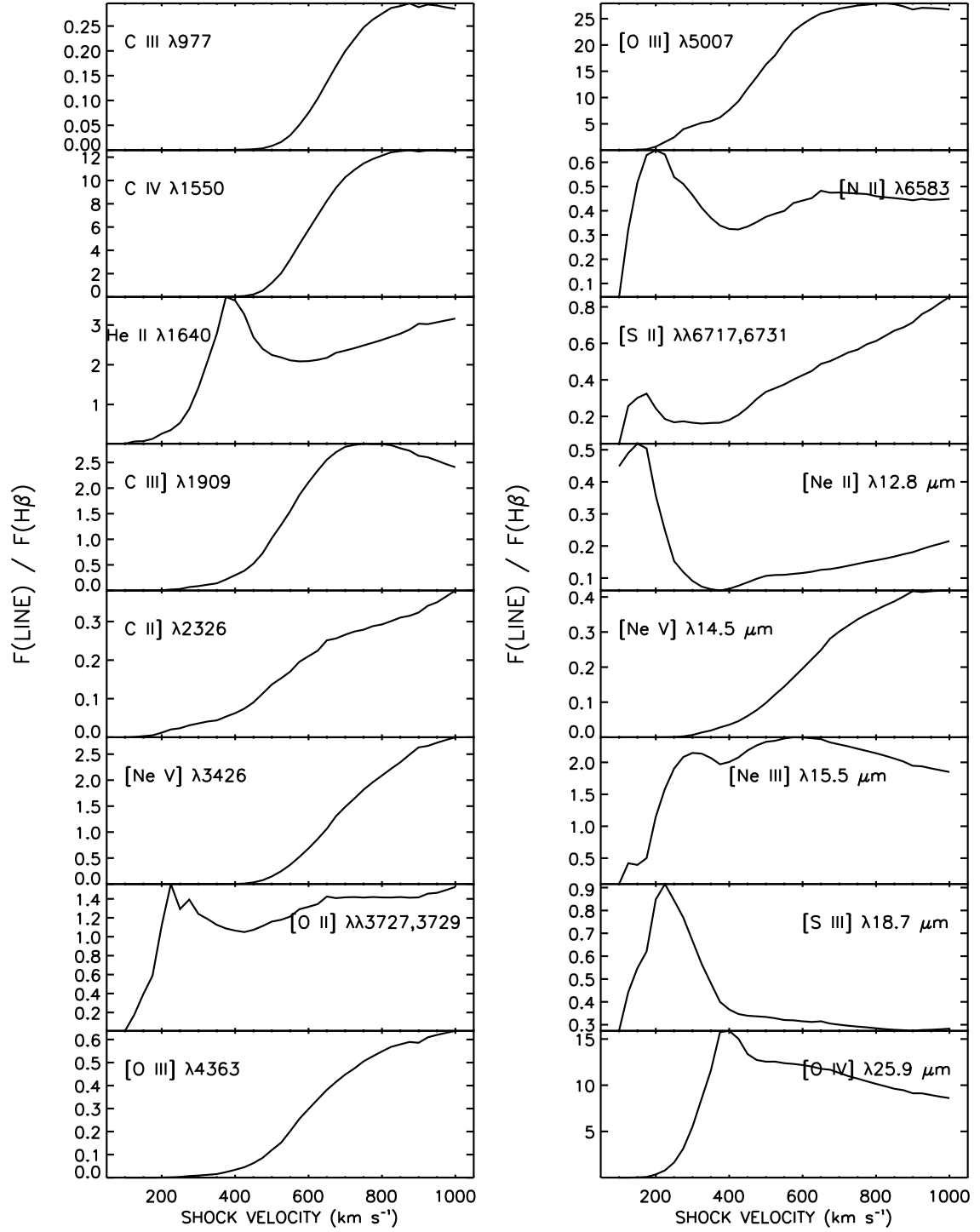


FIG. 17.— As Figure 16 but for the precursor component of the models only.

multi-dimensional methods for comparing data to models because the ratios can be chosen to be independent of reddening, and tuned to be sensitive to particular physical properties of interest. For example, Dopita et al. (2006) have provided theoretical strong emission line diagnostics for ensembles of H II regions to enable more accurate measurement of chemical abundances in unresolved starburst galaxies, and Kewley et al. (2006) combined standard line ratio diagrams with velocity dispersion measurement to help refine the classification of active galaxies.

As part of the shock model library available online, we include interactive plotting tools to plot diagnostic diagrams, such as the examples presented in the following sections. These tools enable a much clearer picture of these diagnostics than possible within the paper, especially with those grids that twist and fold upon themselves in the 2-D diagrams. In addition, many other diagnostic ratios than those presented here can be formed to gain insights into what diagnostics can be used when only a limited sample of lines are available.

5.2. Optical Diagnostics

As a first example, we plot the new shock model grids on a number of the standard optical diagnostic diagrams to reveal the general shape of the model grids, and the sensitivity of the diagnostics to the parameters of shock velocity, magnetic parameter and chemical abundance set. Figure 19 shows the perhaps the most frequently used of the diagnostic diagrams, the Veilleux & Osterbrock (1987) plot of $[\text{O III}]\lambda 5007/\text{H}\beta$ versus $[\text{N II}]\lambda 6583/\text{H}\alpha$, also commonly known as the BPT diagram (Baldwin et al. 1981). For clarity, the shock and shock+precursor grids for the solar abundance $n = 1 \text{ cm}^{-3}$ models are plotted separately but on the same scale, as is the case in most of the following diagrams, due to the overlap of the two grids. These two grids represent the physical extremes of having little or no gas ahead of the shock (shock-only), and having an extensive, radiation bounded, precursor region ahead of the shock. As in DS95, the two grids show the range in shock velocity and magnetic parameter, as labelled in the diagram. The lines of constant velocity are plotted at 50 km s^{-1} intervals as the thin lines. The lines of constant magnetic parameter are plotted as the thick lines in the grid, with the value of the magnetic parameter as marked. For a clearer picture of this and all other diagnostic diagrams in the paper we provide color figures in the online journal.

This figure reveals a similar picture to that in DS95 (their Fig. 2b), with the shock-only and shock+precursor grids occupying different regions of the diagram, a result of the different processes discussed in the previous sections. Both grids shows broad steps in velocity up to a velocity of $\sim 550 \text{ km s}^{-1}$, at which the grids begin to compress and turn upon themselves, becoming degenerate. However, for the shock-only grid an increase in velocity causes an increase in the $[\text{N II}]/\text{H}\alpha$ ratio, while for the shock+precursor models in results in an increase of the $[\text{O III}]/\text{H}\beta$ ratio. The situation is reversed for an increase of the magnetic parameter, causing the spread observed in the grids, though the shock+precursor models tend to be degenerate in this parameter at high values. The spread of the grids and their separation indicate the

diagnostic power of these figures, allowing the determination of the physical parameters in known shock-ionized plasmas.

Improvements to the MAPPINGS III code compared to the MAPPINGS II code used by DS96 means that there are some significant and systematic differences compared to the DS95 grids. Figure 20 shows a direct comparison of the DS95 shock and shock+precursor model grids overlaid on our new solar abundance shock and shock+precursor models for the same diagnostic diagram. The improvement of our new models in terms of parameter space is clear, with DS95,96 models limited to 500 km s^{-1} in velocity space, and only covering magnetic parameters of $0\text{--}4 \mu\text{G cm}^{3/2}$. The shock component of the models agree reasonably well over the common parameter ranges, although appears somewhat offset. However the shock+precursor grid shows a difference of up to 0.5 dex in the $[\text{O III}]\lambda 5007/\text{H}\beta$ and $[\text{N II}]\lambda 6583/\text{H}\alpha$ ratios. We note again that on this diagram the new shock+precursor models turn over at high shock velocity. One consequence of this is that some active galaxies such as high-redshift radio galaxies, which have been confirmed as being excited by shocks and which were interpreted as matching $400\text{--}500 \text{ km s}^{-1}$ shock+precursor models, may in fact be characterized by higher shock velocities. This would help resolve the mis-match between radial velocity dispersions and shock velocities inferred by line ratios as inferred, for example, by Reuland et al. (2007).

Figure 21 shows the same diagram for the different chemical abundance sets which we have used. Each grid covers the same range in shock velocity and magnetic parameter. In both shock and shock+precursor models the $[\text{O III}]\lambda 5007/\text{H}\beta$ ratio is only weakly affected by abundance, as the increased temperatures within the models from the reduced cooling counteracts somewhat the effects of the drop in oxygen abundance on this ratio (see Figure 7). The $[\text{N II}]\lambda 6583/\text{H}\alpha$ ratio however changes significantly with abundance, predominantly as a consequence of the larger relative abundance differences in nitrogen due to its secondary nucleosynthesis component. In the shock models, the $[\text{O III}]/\text{H}\beta$ does not change significantly in range either, but the $[\text{N II}]/\text{H}\alpha$ ratio becomes compressed, meaning the diagrams are totally degenerate in velocity at low metallicity, predominantly due to the changes photoionized and recombination regions of the shock with metallicity. The case is similar for the shock+precursor, with the grids becoming generally more “compressed” with decreasing metallicity, and decreasing the diagnostic power of the diagrams. Note that for each abundance set the shock-only and shock+precursor models still tend to be discrete grids, and do not significantly overlap.

In Figure 22 we investigate the effect of changing the pre-shock densities on this Veilleux & Osterbrock (1987) diagnostic. For the solar abundance grid, we display the results for the two extreme values of density $n = 0.01 \text{ cm}^{-3}$ and $n = 1000 \text{ cm}^{-3}$ for both the shock and shock+precursor models. Note the change in scale between this figure and Figure 19, necessary due to the changes in the grids.

As discussed in section 2.1, the models with varying density were computed not only with the standard mag-

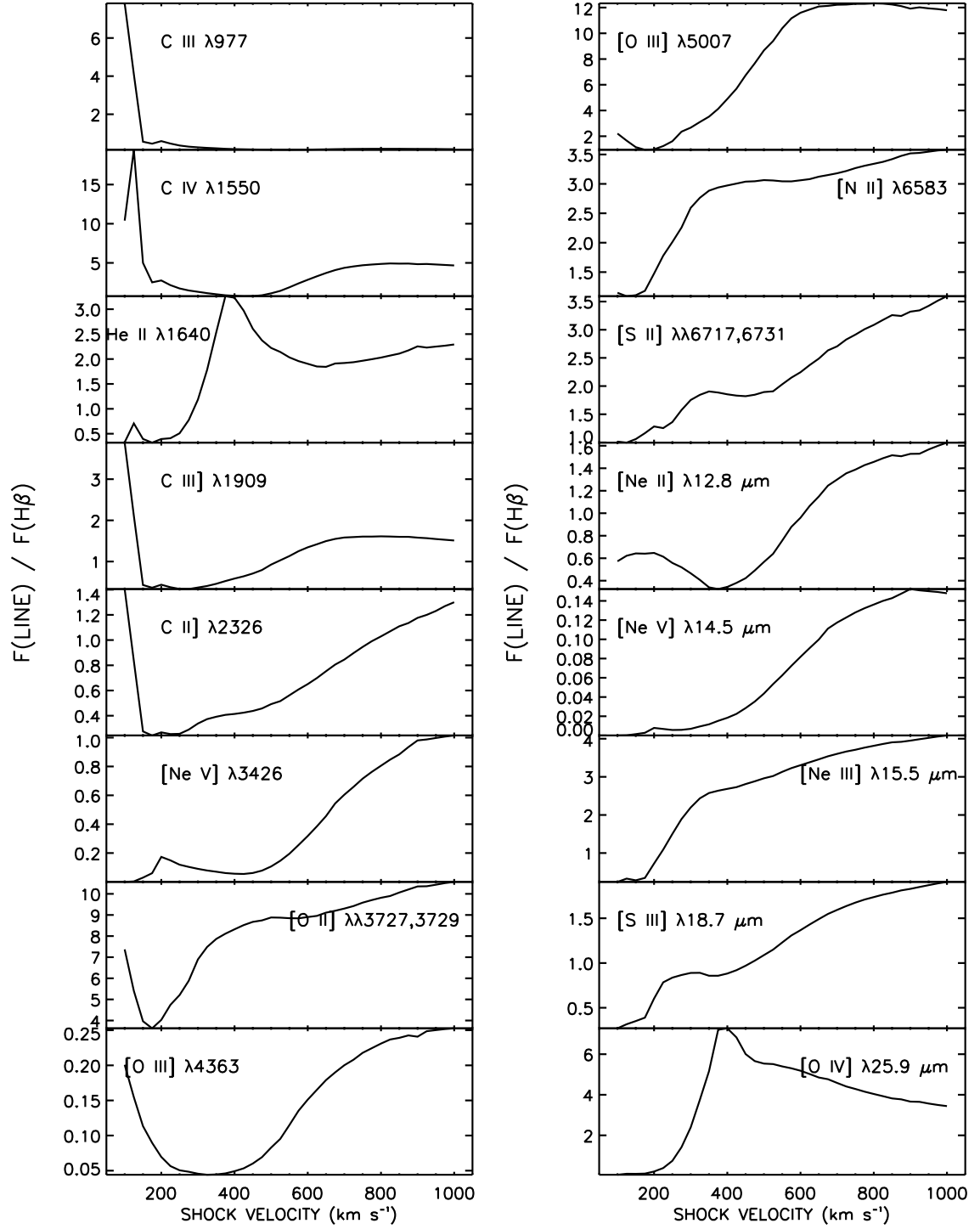


FIG. 18.— As Figure 16 but for the the full shock+precursor model.

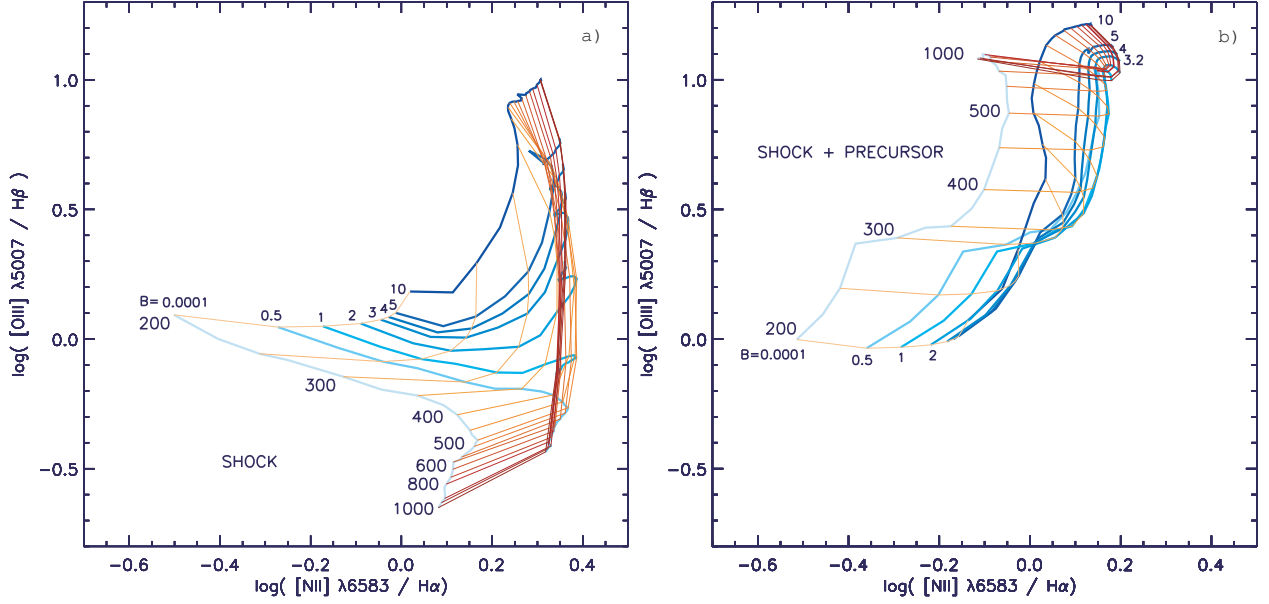


FIG. 19.— The classic Veilleux & Osterbrock (1987) $[\text{O III}]\lambda 5007/\text{H}\beta$ versus $[\text{N II}]\lambda 6583/\text{H}\alpha$ diagnostic diagram for the solar abundance $n = 1 \text{ cm}^{-3}$ models. The left figure shows the shock-only models, and the right figure shows the shock+precursor models. The grid is comprised of lines of constant magnetic parameter shown with a bold linestyle, and lines of constant shock velocity shown as the thin lines. The lines of constant shock velocity are shown at 50 km s^{-1} intervals (and are color coded with increasing red intensity for higher shock velocities in the electronic edition). The velocity sequences are shown for all values of the magnetic parameter (and are color coded with increasing blue intensity for higher magnetic parameters in the electronic edition). Both the shock-only and shock+precursor grids are shown for the shock velocities of 200–1000 km s^{-1} , for which all the models have a fully ionized precursor. See the electronic edition of the Journal for a color version of this figure.

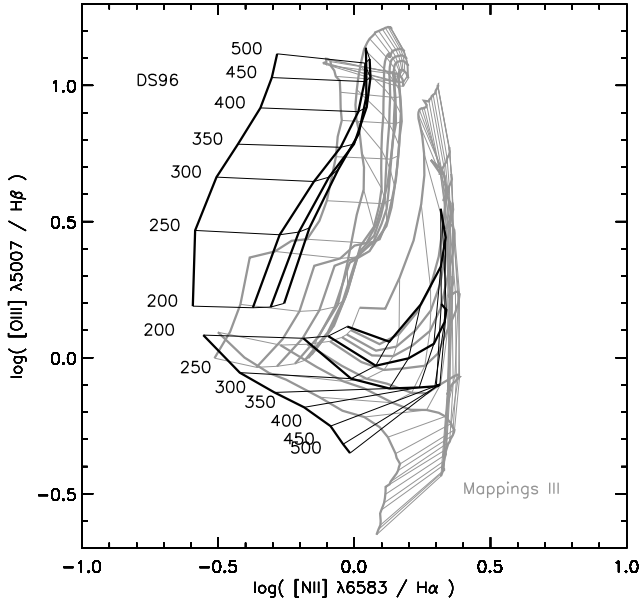


FIG. 20.— Comparison of the new MAPPINGS III models with the DS96 on the $[\text{O III}]\lambda 5007/\text{H}\beta$ versus $[\text{N II}]\lambda 6583/\text{H}\alpha$ diagram. The DS96 models are shown in black, they are labelled with the shock velocity in km s^{-1} , and include velocity sequences for magnetic parameters of 0, 1, 2 and $4 \mu\text{G cm}^{3/2}$ which increase from left to right in both the shock-only (lower) and shock+precursor (upper) grids. The new MAPPINGS III models are shown in greyscale and cover the same range in shock velocity and magnetic field as shown in Figure 19. Note that the new diagrams show systematic changes with respect to the earlier ones, and that the new models show that these ratios become insensitive to shock velocity for $v_s > 500 \text{ km s}^{-1}$.

netic parameter set, but also a range of magnetic fields to allow for the comparison of both B and B/\sqrt{n} between the model grids. The range of both B and B/\sqrt{n} for these models are given in Table 3. We include all these

models in Figure 22 for completeness, meaning that the grids sample more finely and extend further both the low and high values of the magnetic parameter than seen in Figures 19–21.

The low-density model grids are in most respects exactly the same as the $n = 1 \text{ cm}^{-3}$ grids seen in Figure 19, with the only difference arising due to the extended B/\sqrt{n} range sampled. This similarity is not surprising, as while the luminosity decreases linearly with the decreased density, as seen in Equation 5, the ionization parameter is inversely proportional to density and therefore remains approximately the same in both the shock recombination region and the precursor region. One interesting thing to note is how degenerate the grids become upon the introduction of the very high magnetic parameters.

However, at high pre-shock densities there are clear changes in both the shock and shock+precursor grids. In the shock-only grid the low magnetic parameter models extend to lower values in the both $[\text{O III}]/\text{H}\beta$ and $[\text{N II}]/\text{H}\alpha$ ratios by up to 1 dex, while in the shock+precursor grid only the $[\text{N II}]/\text{H}\alpha$ ratio is reduced. This is caused by collisional de-excitation of the forbidden lines in the photoionized and recombination regions of the shock, where the electron densities are very high. The shock+precursor does not change significantly in $[\text{O III}]/\text{H}\beta$ as most of the emission of the $[\text{O III}]$ line arises from the precursor, which is not high enough density to collisionally de-excite this transition. There is less of a difference between the grids at high magnetic parameters and at low to intermediate velocities, because lower velocities lead to smaller compression factors, and because magnetic pressure support helps to lessen the degree of gas compression in the tail end of the shock, meaning that the high density needed to collisionally de-

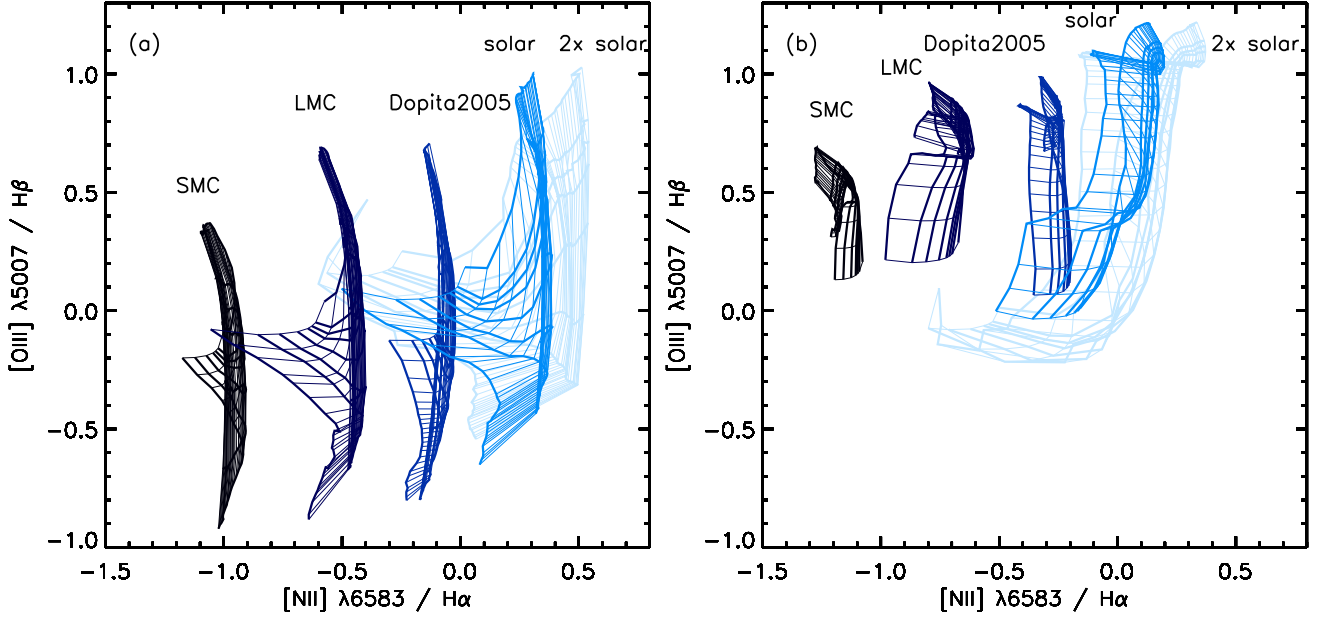


FIG. 21.— Shock and shock+precursor model grids for the five different atomic abundance sets used in the shock model library for the $[\text{O III}]\lambda 5007/\text{H}\beta$ versus $[\text{N II}]\lambda 6583/\text{H}\alpha$ diagram. The shock-only models are shown in (a), and the shock+precursor models are shown in (b). All model grids are shown for v_s 200–1000 km s^{-1} , with lines of constant shock velocity drawn at intervals of 50 km s^{-1} . Each grid is labelled with the abundance set used, and generally moves from left to right as the total metallicity increases. See the electronic edition of the Journal for a color version of this figure.

excite these transitions is not reached.

Another commonly used Veilleux & Osterbrock (1987) diagnostic is the $[\text{O III}]\lambda 5007/\text{H}\beta$ versus $[\text{S II}]\lambda\lambda 6716, 6731/\text{H}\alpha$ diagram. In Figure 23 we plot the new grids for this diagram, with the shock and shock+precursor models plotted separately for clarity, as the overlap between the grids makes distinguishing them difficult. As with the previous diagnostic diagram, both the shock and shock+precursor models turn over at high velocities, becoming twisted and with little separation between the velocities. Similarly the magnetic parameters show a similar range in spread in both models, and become more spread with increasing velocity in the shock-only model. The shape of the shock+precursor grid on this diagram is again rather different compared to DS95. Like in Figure 20, the new shock+precursor model covers a wider range in $[\text{O III}]/\text{H}\beta$, with a lower value at $v_s = 200 \text{ km s}^{-1}$, while it appears somewhat offset to higher values of $[\text{S II}]/\text{H}\alpha$, though not significantly. It also does not appear to show the degenerate nature seen in DS95 (their Figure 2a). The shock models are harder to compare due to the wider parameter range in the model, but in general show the same features of increased $[\text{S II}]/\text{H}\alpha$ with velocity, with the turn over around $\sim 500 \text{ km s}^{-1}$. The greater range in magnetic parameter of the new models also means that the spread in $[\text{O III}]/\text{H}\beta$ is much greater at higher velocities as well.

Figure 24 is a plot of the well-known temperature-sensitive ratio $[\text{O III}]\lambda 4363/[\text{O III}]\lambda 5007$ (also known as R_{OIII}) versus the $[\text{O III}]\lambda 5007/\text{H}\beta$ ratio, with again the shock-only and shock+precursor spectra plotted separately. Considering first the shock-only grid, at low magnetic parameter the electron temperature in the O^{2+} zone is consistently high, with only the $[\text{O III}]\lambda 5007/\text{H}\beta$ ratio decreasing with increasing shock velocity. However, as the magnetic parameter rises, the decreased compres-

sion in the photoionized tail of the shock leads to a higher ionization parameter in this zone, and greater dominance of $[\text{O III}]$ in the photoionized zone, which has an electron temperature close to 10000K. As a consequence, the electron temperature decreases and the $[\text{O III}]\lambda 5007/\text{H}\beta$ ratio increases with increasing shock velocity. Together this leads to the fan shape observed in the diagram. The shock+precursor grid is dominated by the bright $[\text{O III}]$ emission of the precursor region, and as the precursor is not sensitive to the magnetic parameter, this grid covers a reduced area of the parameter space in the diagram. In terms of velocity, the curve increases in $[\text{O III}]\lambda 5007/\text{H}\beta$ and decreases in R_{OIII} up to a velocity of $\sim 500 \text{ km s}^{-1}$, then turns over and begins to increase in temperature again. The shock+precursor grid at velocities less than $\sim 450 \text{ km s}^{-1}$ and the high magnetic parameter shock-only grid overlap, meaning this diagnostic is degenerate in this range. This diagram is very similar to the DS95, with only the extension to higher velocities and magnetic parameter range differentiating it. However, this similarity also indicates that the well-known “Temperature Problem”, discussed in DS95 and many other papers, still exists. A comparison of our models with the observations used in DS95 or larger datasets like SDSS show that the R_{OIII} ratio is too low, and even different abundance sets are unable to fully solve this issue.

5.3. UV Diagnostics

In Allen et al. (1998) we emphasized the use of UV line ratio diagrams for the discrimination between shocks and photoionization models for the NLR. These diagrams use relatively bright emission lines and reddening-insensitive ratios. One of the most useful diagrams involves the various ionization stages of carbon $\text{C II}]\lambda 2326/\text{C III}]\lambda 1909$ vs. $\text{C IV}]\lambda 1550/\text{C III}]\lambda 1909$. This diagram is shown in Figure 25 with the new solar abundance $n = 1 \text{ cm}^{-3}$ shock models. There is significantly more overlap

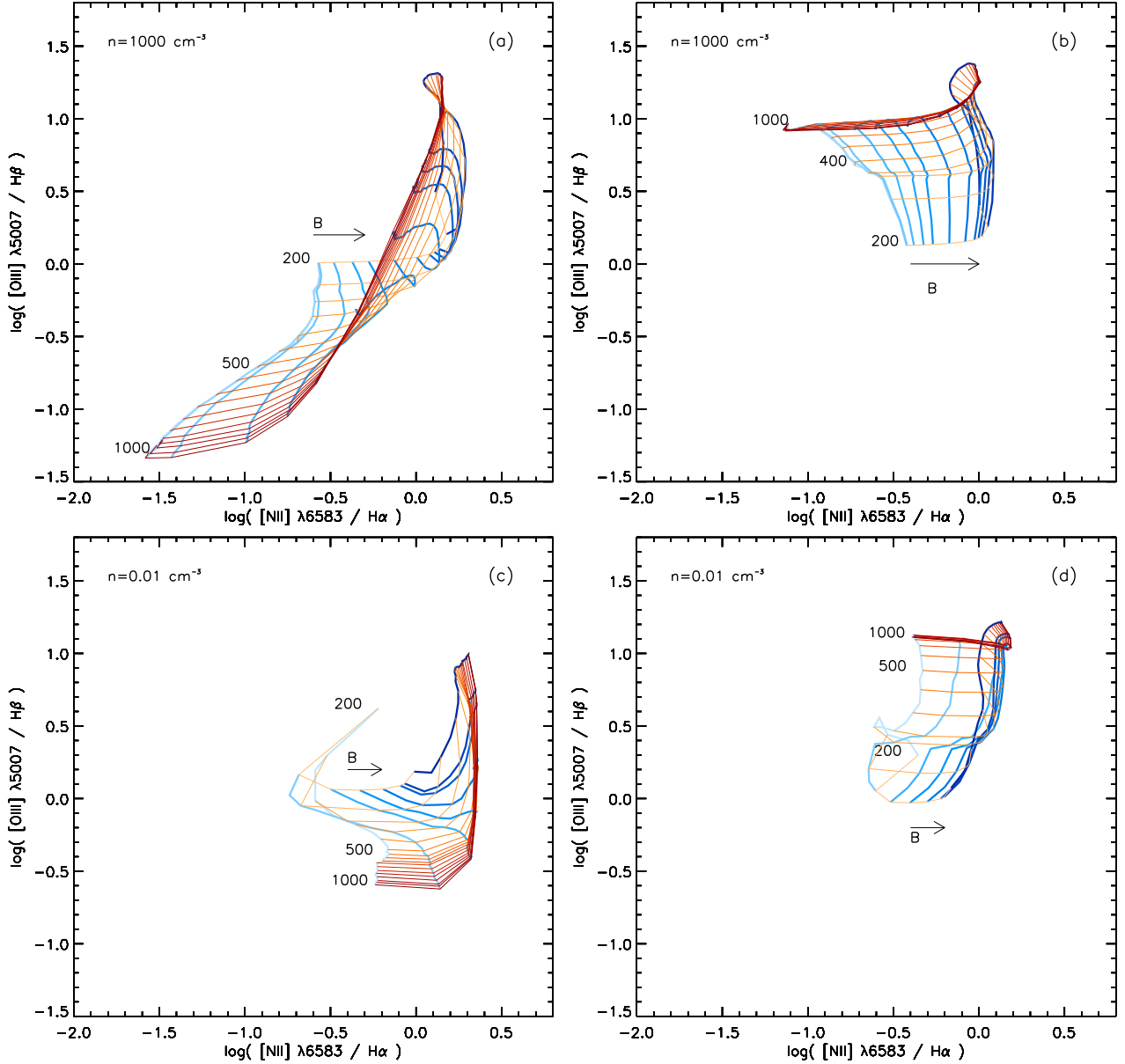


FIG. 22.— Shock and shock+precursor model grids of solar abundance models for two different pre-shock densities on the $[\text{O III}]\lambda 5007/\text{H}\beta$ versus $[\text{N II}]\lambda 6583/\text{H}\alpha$ diagram. The top figures show the high density case and the lower figures the low density case, with a) The $n = 1000 \text{ cm}^{-3}$ shock model grid, b) the $n = 1000 \text{ cm}^{-3}$ shock+precursor models, c) The $n = 0.01 \text{ cm}^{-3}$ shock model grid, and d) the $n = 0.01 \text{ cm}^{-3}$ shock+precursor models. The grids show shock velocities over the range $v_s = 200\text{--}1000 \text{ km s}^{-1}$ with lines of constant magnetic parameter shown as thick lines (and colored with increasing blue intensity for higher magnetic parameter in the electronic edition). The thin lines represent constant shock velocity and these are plotted for the full range of magnetic parameters for each density as listed in Table 2 (and are shown colored with increasing red intensity for higher shock velocities in the electronic edition). See the electronic edition of the Journal for a color version of this figure.

between the new shock and shock+precursor grids than with the DS96 models because the higher magnetic parameter shock models form a fan-like grid on these axes, which almost completely encompasses the region covered by the shock+precursor models. The shock+precursor grid is twisted on these axes making it multi-valued at most positions, hence not good for assessing shock parameters. This diagram does however remain of great use for separating shock and photoionization models.

Another useful diagram combines the UV carbon ratio of $\text{C III} \lambda 1909 / \text{C II} \lambda 2326$ with $[\text{Ne III}] \lambda 3869 / [\text{Ne V}] \lambda 3426$. This has been used by Best et al. (2000) and Inskip et al. (2002) to identify shocks and photoionization in the emission line gas of 3CR and 6C

radio galaxies. They show that the ionization state of the gas varies with radio size such that large radio sources ($> 120 \text{ kpc}$) are consistent with AGN photoionization, while smaller sources are consistent with shocks associated with the expanding radio source. Furthermore the extreme gas kinematics in the smaller radio sources, and detailed consideration of the energetics and observability of shocks in Inskip et al. (2002) supports the interpretation of shock excitation.

As described in Inskip et al. (2002), there is a continuous sequence of objects which fall in between the shock dominated and photoionization dominated groups. In these, both mechanisms are likely to play a role and the balance between shocks and photoionization is may

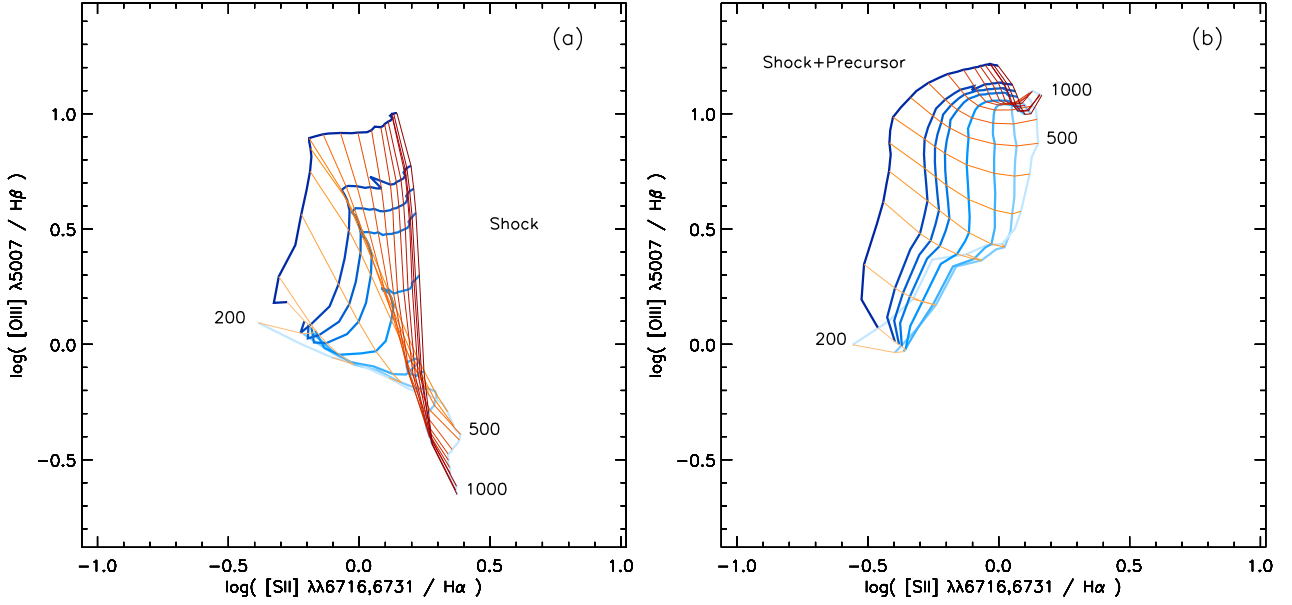


FIG. 23.— The Veilleux & Osterbrock (1987) plot of $[\text{O III}]\lambda 5007/\text{H}\beta$ versus $[\text{S II}]\lambda\lambda 6716,6731/\text{H}\alpha$ diagram for a) the shock and b) the shock + precursor models with $n = 1 \text{ cm}^{-3}$ and solar abundance. The range and step size of the shock velocity and magnetic parameter for these grids are the same as in Figure 19. See the electronic edition of the Journal for a color version of this figure.

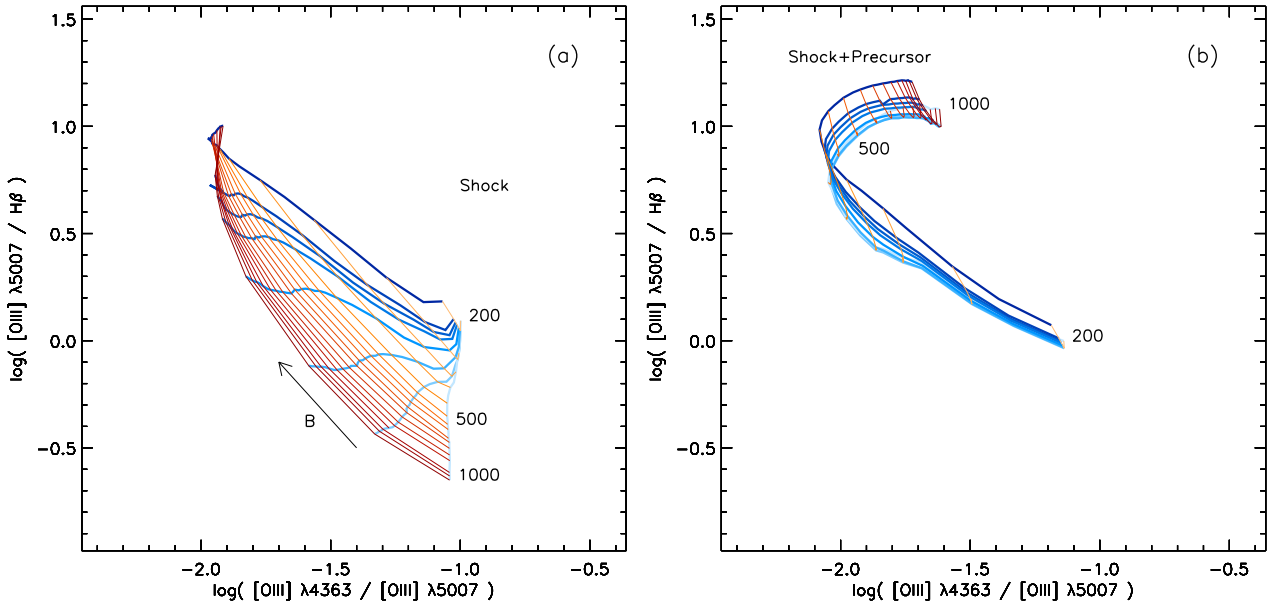


FIG. 24.— The temperature sensitive $[\text{O III}]\lambda 4363 / [\text{O III}]\lambda 5007$ ratio (R_{OIII}) versus the $[\text{O III}]\lambda 5007/\text{H}\beta$ line ratio diagram for the solar abundance $n = 1 \text{ cm}^{-3}$ models. Panel (a) shows the shock grid, and panel (b) shows the shock+precursor grid. The range and step size of the shock velocity and magnetic parameter for these grids are the same as in Figure 19. See the electronic edition of the Journal for a color version of this figure.

be linked to the radio source size. As the definition of the shock and photoionization groups relies on the coverage of the respective model grids, it is important that these grids are complete. In Figure 26 we reconstruct the same $\text{C III}] \lambda 1909 / \text{C II}] \lambda 2326$ versus $[\text{Ne III}] \lambda 3869 / [\text{Ne V}] \lambda 3426$ diagram as used by Best et al. (2000) and Inskip et al. (2002) using the data tabulated in those papers. We overlay the new shock model grids to demonstrate how these relate to, and possibly help explain, these previously-made conclusions. For comparison, we also plot the set of new and updated AGN photoionization models from Groves et al. (2004b) as well as the $A_{M/I}$ models from Binette et al. (1996) that combine

matter- and ionization-bounded clouds to create the observed sequence.

The shock and shock+precursor models are those for new solar abundance $n = 1 \text{ cm}^{-3}$. As in the previous diagram, the shock models define a fan shaped grid, and the shock+precursor grid turns over in both ratios. With the wider range in shock velocity and magnetic parameter the new models cover a greater region of this diagram than the DS96 models used by Best et al. (2000) and Inskip et al. (2002). Indeed a number of 6C sources which have $\text{C III}] \lambda 1909 / \text{C II}] \lambda 2326$ ratios intermediate between the main shock and photoionization groups, fall within the higher velocity shock+precursor

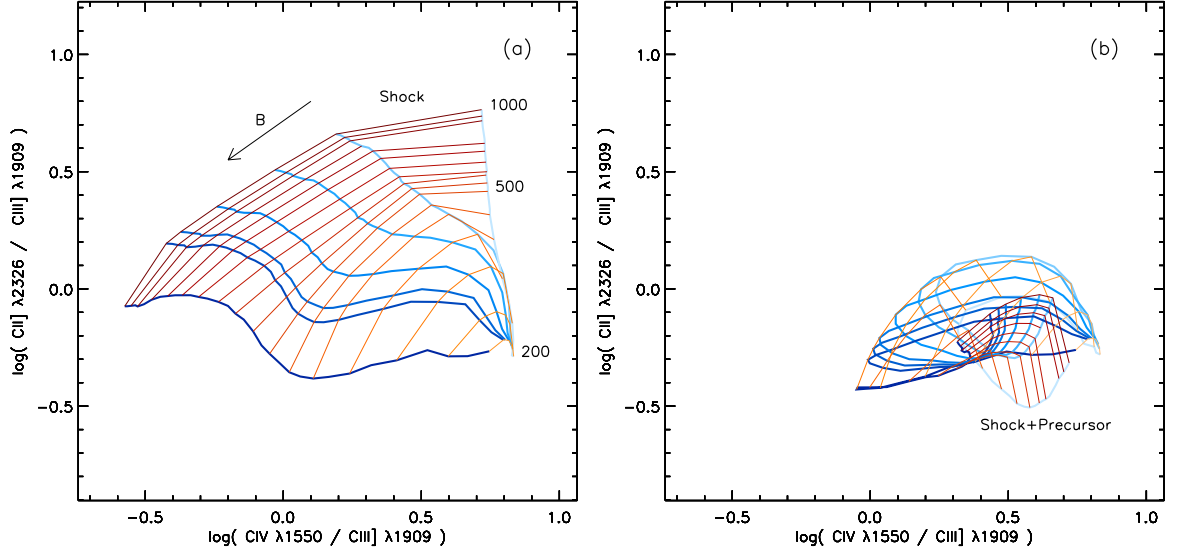


FIG. 25.— The ultraviolet carbon line ratio diagnostic plot for the solar abundance $n = 1 \text{ cm}^{-3}$ shock (a) and shock+precursor models (b). The shock only grid enables both the shock velocity and the magnetic parameter to be independently determined, but the shock + precursor grid is multi-valued at many positions. The range and step size of the shock velocity and magnetic parameter for these grids are the same as in Figure 19. See the electronic edition of the Journal for a color version of this figure.

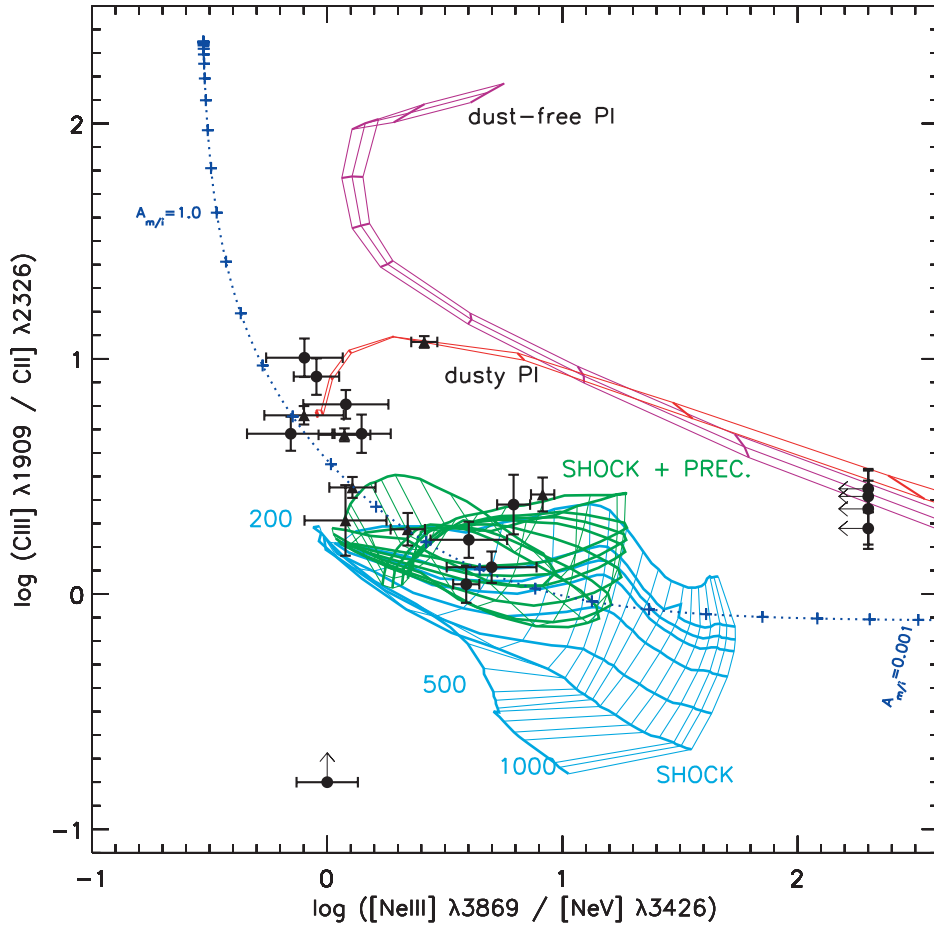


FIG. 26.— The $\text{C III} \lambda 1909 / \text{C II} \lambda 2326$ with $\text{Ne III} \lambda 3869 / \text{Ne V} \lambda 3426$ diagram. The shock model grid is shown in light gray (cyan in the electronic edition) and is labelled with the shock velocity. The shock+precursor grid is shown in dark gray (green in the electronic edition), and displays a twisted shape on these axes, and also overlaps the shock grid. The dusty and dust-free models of Groves et al. (2004b) are also shown with the ionization parameter increasing to the left of the diagram before the turn-over in these curves. The $A_{M/I}$ models from Binette et al. (1996) are shown as a dotted line with the + symbols indicating increments of 0.25 dex. The data points are those from Best et al. (2000) and Inskip et al. (2002) as indicated in the text.

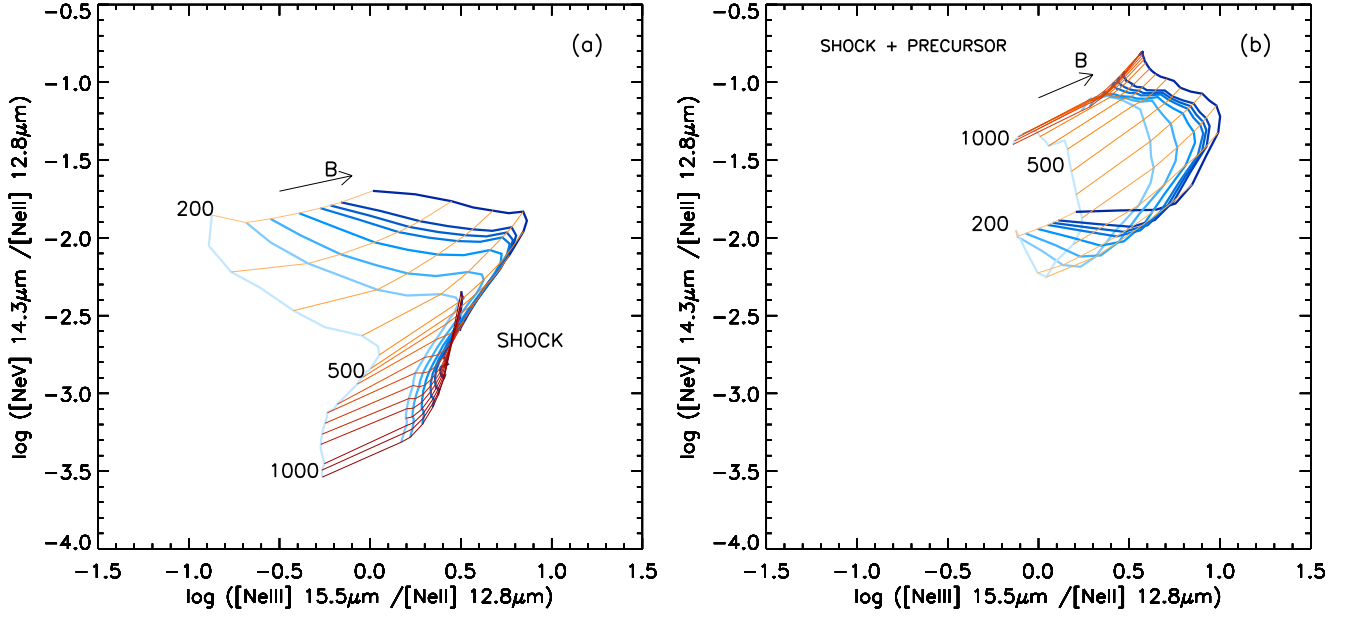


FIG. 27.— IR diagnostic diagram of $[\text{Ne V}]14.3\mu\text{m}/[\text{Ne II}]12.8\mu\text{m}$ versus $[\text{Ne III}]15.5\mu\text{m}/[\text{Ne II}]12.8\mu\text{m}$. Panels (a) and (b) show respectively the shock and shock+precursor model grids for the solar abundance $n = 1 \text{ cm}^{-3}$ models. The range and step size of the shock velocity and magnetic parameter for these grids are the same as in Figure 19. See the electronic edition of the Journal for a color version of this figure.

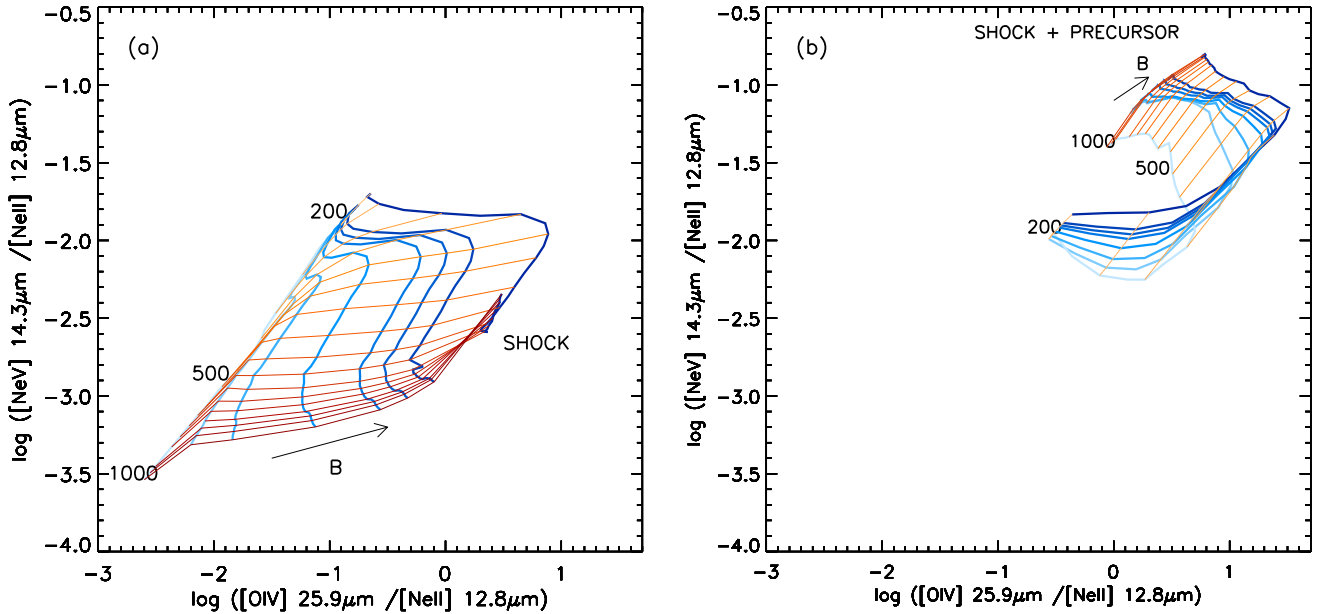


FIG. 28.— IR diagnostic diagram of $[\text{Ne V}]14.3\mu\text{m}/[\text{Ne II}]12.8\mu\text{m}$ versus $[\text{O IV}]25.9\mu\text{m}/[\text{Ne II}]12.8\mu\text{m}$. Panels (a) and (b) show respectively the shock and shock+precursor model grids for the solar abundance $n = 1 \text{ cm}^{-3}$ models. The range and step size of the shock velocity and magnetic parameter for these grids are the same as in Figure 19. See the electronic edition of the Journal for a color version of this figure.

grid (6C 1017, 6C 1256, 6C 0943, 6C 1019).

The dust-free and dusty photoionization models from Groves et al. (2004b) demonstrate the other extreme of ionization, where the emission arises totally from gas excited by the ionizing radiation emitted by the accretion of gas onto the central black hole of the AGN. The dust-free models represent MAPPINGS III photoionization models that have been calculated for a sequence of ionization parameters and densities. The $1Z_{\odot}$, $\alpha = -1.4$, $n_{\text{H}} = 10^2$ - 10^4 models shown here behave in a similar way to the MAPPINGS II models described in Allen et al. (1998) (and

used by Best et al. (2000) and Inskip et al. (2002)). The dusty models incorporate the effect of radiation pressure and result in a stagnation of the ionization parameter at high values, offering an explanation for the similarity of Seyfert NLR spectra. Figure 26 shows that the dusty photoionization models can produce line ratios as observed in the larger 3CR and 6C radio sources. The dusty photoionization model plotted here is the $1Z_{\odot}$, $\alpha = -1.4$, $n_{\text{H}} = 10^2$ and $n_{\text{H}} = 10^4$ model, and a discussion of these models in terms of the Best et al. (2000) and Inskip et al. (2002) data, as well as a full grid of such models on

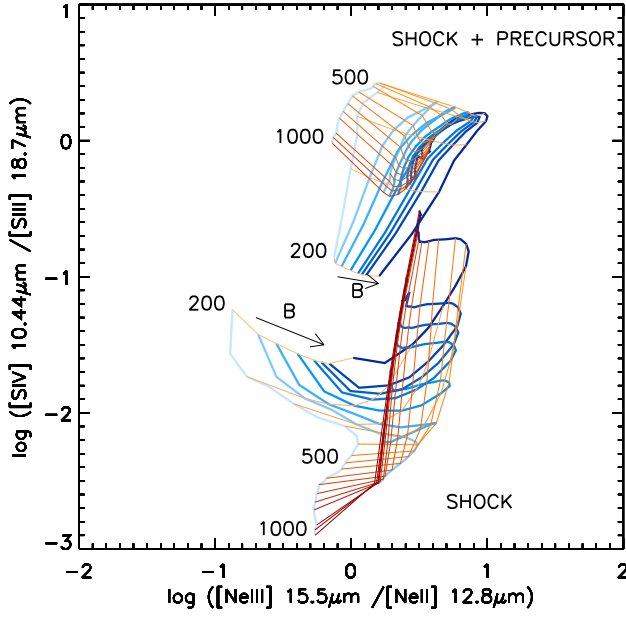


FIG. 29.— IR diagram of $[S\text{ IV}]10.44\mu\text{m}/[S\text{ III}]18.7\mu\text{m}$ versus $[Ne\text{ III}]15.5\mu\text{m}/[Ne\text{ II}]12.8\mu\text{m}$ showing the shock and shock+precursor grids of the solar abundance $n = 1\text{ cm}^{-3}$ models, as labelled. The range and step size of the shock velocity and magnetic parameter for these grids are the same as in Figure 19. See the electronic edition of the Journal for a color version of this figure.

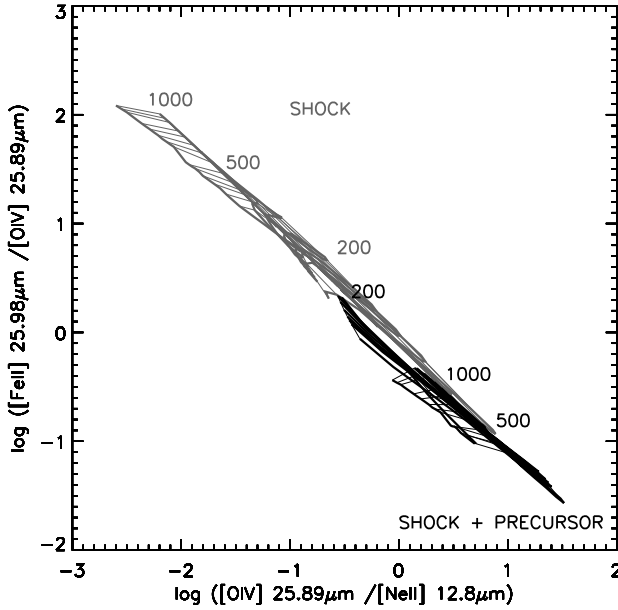


FIG. 30.— IR diagram $[Fe\text{ II}]26.0\mu\text{m}/[O\text{ IV}]25.9\mu\text{m}$ versus $[O\text{ IV}]25.9\mu\text{m}/[Ne\text{ II}]12.8\mu\text{m}$ as introduced by Lutz et al. (2003), overlaid with the shock and shock+precursor model grids.

the same diagram can be found in Groves et al. (2004b).

5.4. IR Diagnostics

The mid- and far-IR emission from galaxies is dominated by the emission of dust that is heated by UV radiation. IR spectra contain PAH and dust features and are also rich in atomic fine structure emission lines. These spectral features, as observed by ISO and Spitzer offer a wealth of information for studying the nature of the circumnuclear dust, and the contributions of the AGN,

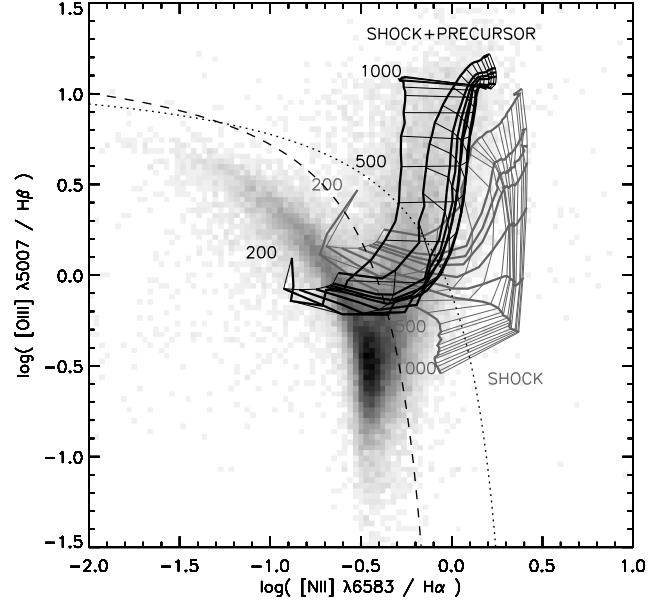


FIG. 31.— Comparison of the shock and shock+precursor models to SDSS line ratios on the $[O\text{ III}]\lambda 5007/H\beta$ versus $[N\text{ II}]\lambda 6583/H\alpha$ diagram. The model grids are those with $2\times$ solar abundance. The dotted and dashed curved lines represent the Kewley et al. (2001a) and Kauffmann et al. (2003) classification lines respectively which divide H II regions (lower left) from the region occupied by AGN.

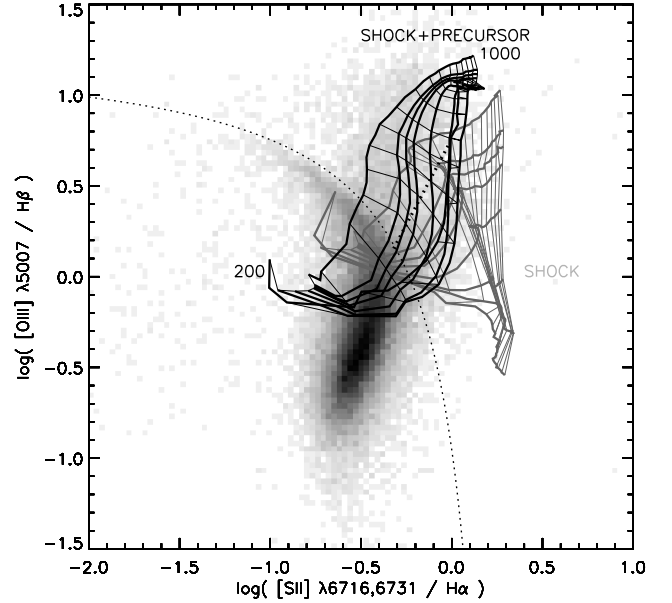


FIG. 32.— Comparison to SDSS line ratios to the $2\times$ solar abundance model grids. The thin dotted line represents the Kewley et al. (2001a) starburst/AGN classification line, while the thick straight dotted line represents the Seyfert-LINER division described by Kewley et al. (2006).

shocks and starbursts to the total IR emission.

Genzel et al. (1998) introduced infrared diagnostic diagrams using ratios of $[Ne\text{ V}]14.3\mu\text{m} / [Ne\text{ II}]12.8\mu\text{m}$ and $[O\text{ IV}]25.9\mu\text{m} / [Ne\text{ II}]12.8\mu\text{m}$ to investigate starbursts, ULIRGs and AGNs. They used these line ratios, combined with PAH strengths to place limits on the percentage contribution of AGN and starburst contributions to the IR emission of ULIRGs. Mid-IR diagnostics for LINERs are described by Sturm et al. (2006), where they use the high ionization $[O\text{ IV}]25.9\mu\text{m}$ and $[Ne\text{ V}]14.3\mu\text{m}$

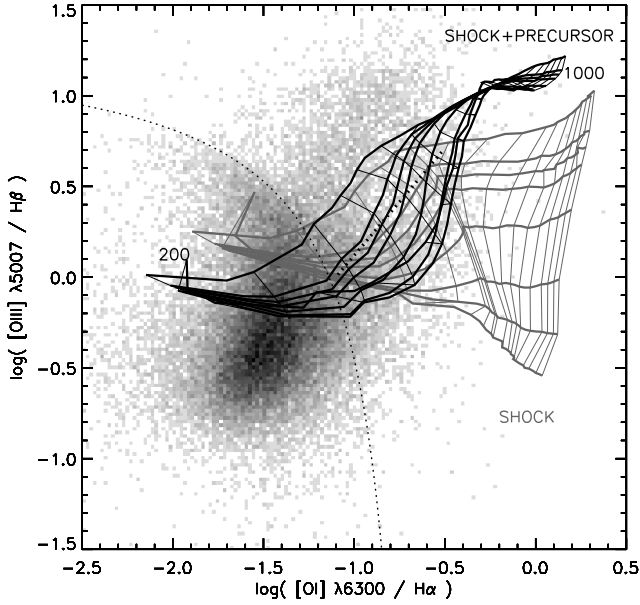


FIG. 33.— Comparison to SDSS line ratios to the $2\times$ solar abundance model grids. The thin dotted line represents the Kewley et al. (2001a) starburst/AGN classification line, while the thick straight dotted line represents the Seyfert-LINER division described by Kewley et al. (2006).

lines to identify the presence of AGN in $\sim 90\%$ of LINERs. They confirm the differences in properties between IR-faint and IR-luminous LINERs, and identify the need to disentangle the various stellar, H II region and AGN processes at work in these objects.

Groves et al. (2006) investigated the IR emission of the NLR distinct from the emission of the torus, showing that the NLR emission can contribute up to $\sim 10\%$ of the IRAS $25\mu\text{m}$ flux. They emphasize the fact that high ionization lines like $[\text{Ne V}]14.3\mu\text{m}$ arises only in the NLR, and their diagnostic diagram which utilizes only IR lines of neon provides a very useful indicator of AGN and starburst contributions.

Here we present a set of IR diagnostic diagrams drawn from these previous works, overlaid with the solar abundance shock and shock + precursor model grids. Figure 27 ($[\text{Ne V}]14.3\mu\text{m} / [\text{Ne II}]12.8\mu\text{m}$ versus $[\text{Ne III}]15.5\mu\text{m} / [\text{Ne II}]12.8\mu\text{m}$) combines three different ionization stages of neon removing any abundance dependence. Figure 28, $[\text{Ne V}]14.3\mu\text{m} / [\text{Ne II}]12.8\mu\text{m}$ versus $[\text{O IV}]25.9\mu\text{m} / [\text{Ne II}]12.8\mu\text{m}$, utilizes two high ionization species of O IV and Ne V whose ratios to Ne II provide strong discriminants of AGN versus starburst processes. Figure 29 displays the model results for $[\text{S IV}]10.44\mu\text{m} / [\text{S III}]18.7\mu\text{m}$ versus $[\text{Ne III}]15.5\mu\text{m} / [\text{Ne II}]12.8\mu\text{m}$.

Lutz et al. (2003) used the ratios of $[\text{Fe II}]26.0\mu\text{m} / [\text{O IV}]25.9\mu\text{m}$ versus $[\text{O IV}]25.9\mu\text{m} / [\text{Ne II}]12.8\mu\text{m}$ to distinguish between gas ionized by early-type stars, AGN and shocks. Sturm et al. (2006) showed how the same diagram separates starburst galaxies, Seyfert galaxies and supernova remnants. Figure 30 shows how the shock and shock + precursor model grids form relatively tight shock velocity sequences in this diagram. The slope of these sequences is similar to the distribution of observed ratios in Sturm et al. (2006) but the models predict systematically higher ratios than observed, except for some LINER objects which fall in the region of the lower velocity shock

model grid.

5.5. Comparison with SDSS Observations

We now compare the new shock and shock+precursor models to emission line ratios of AGN and star-forming galaxies observed in the Sloan Digital Sky Survey (SDSS). To do this we have adopted the sample of narrow emission line galaxies compiled by Hao et al. (2005). The classification of the sample into broad- and narrow-line AGN, and star-forming galaxies is considered in detail in Hao et al. (2005). Here we choose to use the complete narrow emission line galaxies sample of ~ 42000 sources, and use the AGN/star-forming galaxy separation schemes of Kewley et al. (2001a), Kauffmann et al. (2003), and Kewley et al. (2006) in order to emphasize where our model grids lie with respect to these different classes of objects.

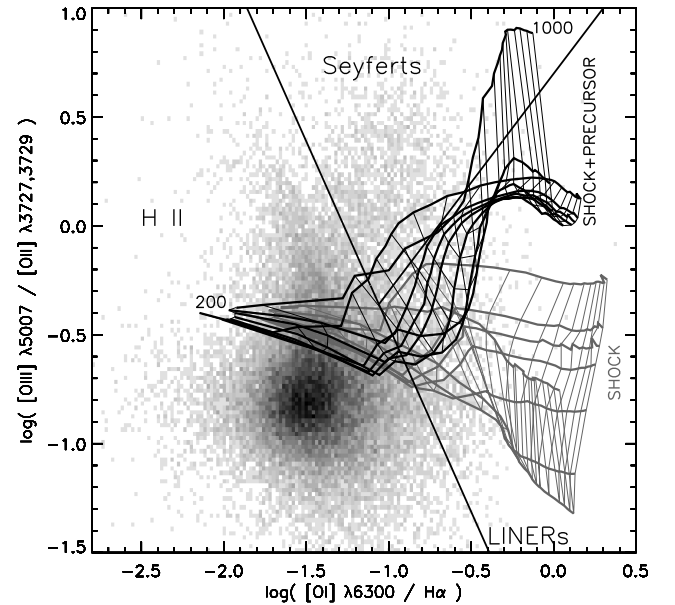


FIG. 34.— Comparison to SDSS line ratios to an oxygen excitation diagnostic in which the regions identified as being excited by H II regions, Seyferts and LINERs are labelled. Note that shock-only spectra may characterize some LINERs, but that the Seyfert galaxies are not well fit by shock+precursor models on this particular diagram.

Figure 31 shows the first of the familiar Veilleux & Osterbrock (1987) diagnostics; $[\text{O III}]\lambda 5007 / \text{H}\beta$ versus $[\text{N II}]\lambda 6583 / \text{H}\alpha$. We have overlaid as a density plot the line ratios observed in the SDSS the narrow emission line sample.

The distribution of emission line galaxies shows two main branches. The star forming galaxy branch sweeps in a curve showing relatively small scatter from upper left to lower right. This is largely an abundance sequence, with abundances increasing towards the lower right (Dopita et al. 2000; Kewley et al. 2001b; Dopita et al. 2006). The AGN are mostly distributed in an arm which extends from the base of the star-forming sequence up towards the upper right of the diagram. AGN generally have higher values of $[\text{N II}]\lambda 6583 / \text{H}\alpha$, and the distribution extends to higher values of $[\text{O III}]\lambda 5007 / \text{H}\beta$. The dotted and dashed curved lines represent the Kewley et al. (2001a) and Kauffmann et al. (2003) classification lines

respectively. The Kewley et al. (2001a) classification is based on the theoretical maximum line ratios possible by pure stellar photoionization. Galaxies above this line are most likely dominated by AGN. The Kauffmann et al. (2003) line is a purely empirical dividing line between pure star-forming galaxies, and Seyfert-HII composite objects.

For comparison, we show in Figure 31 the shock and shock+precursor grids for the 2×solar metallicity models. This choice of metallicity is driven by the work of Groves et al. (2004) and Groves et al. (2006), who find that super-solar metallicity photoionization models best reproduce the observed narrow-line ratios in AGN, and the work of Kauffmann et al. (2003), who find that AGN are typically hosted in galaxies more massive than $10^{10} M_{\odot}$, and therefore likely to contain high metallicity gas (e.g. Tremonti et al. 2004)

Figure 31 reveals that both the shock and shock+precursor models are generally located in the AGN region of this diagram, lying mostly above the Kewley et al. (2001a) classification curve. The shock+precursor grid overlaps well with the strong AGN or Seyfert branch, lying above the Kewley et al. (2006) LINER/Seyfert dividing line, and extends along the branch with increasing shock velocity. The high shock velocity portion of the grid extends roughly to the limit of the observed distribution before folding over on itself at the highest velocities. At lower velocities, the shock+precursor models extend into the “composites” region and even into the starformation or HII region below the Kauffmann et al. (2003) curve at the lowest velocities and magnetic parameters.

The lower velocity shock-only models also overlap the AGN branch, but are predominantly located in the LINER region, simultaneously extending out and spreading out (with magnetic parameter) at the higher shock velocities.

The emission-line galaxies form similar distributions on the other two Veilleux & Osterbrock (1987) diagnostic diagrams; $[O III]\lambda 5007/H\beta$ versus $[S II]\lambda\lambda 6716, 6731/H\alpha$, and the plot of $[O III]\lambda 5007/H\beta$ versus $[O I]\lambda 6300/H\alpha$ (see Figures 32 and 33). The Kewley et al. (2001a) division between AGN and H II region excitation is shown as dotted lines on these figures.

In these figures, the AGN branches show a bifurcation, that has been used by Kewley et al. (2006) to distinguish between Seyfert and LINER galaxies, and so provide a general classification scheme for AGN host galaxies. The Seyfert-LINER dividing line is shown in Figures 32 and 33 as a thick dotted line. The shock and shock+precursor grids overlap the AGN distributions, but tend to fall in the region of the Seyfert-LINER division. The shock-only models mostly fall in the LINER region of these diagnostic plots, but tend to extend to higher values of $[S II]\lambda\lambda 6716, 6731/H\alpha$, and $[O I]\lambda 6300/H\alpha$ than is observed. There is also more overlap with the shock+precursor models than in seen in Figure 31.

Figure 34 shows the $[O III]\lambda 5007/[O II]\lambda\lambda 3726, 3729$ versus $[O I]\lambda 6300/H\alpha$ diagnostic diagram over-plotted with the classification scheme from Kewley et al. (2006). This diagram provides the cleanest separation between the two AGN branches. In photoionized plasmas, the $[O III]\lambda 5007/[O II]\lambda\lambda 3726, 3729$ is sensitive to the specific

intensity of the radiation field, and the $[O I]\lambda 6300/H\alpha$ ratio to the hardness or spectral index of the radiation field. As pointed out by Kewley et al. (2006) this diagram provides a simple method for classification, but is more sensitive to reddening correction of the $[O III]\lambda 5007/[O II]\lambda\lambda 3726, 3729$ ratio. Once again, the shock+precursor grids fall predominantly close to the Seyfert-LINER dividing line, and so describe neither the Seyferts or the LINERs particularly well. The pure shock models are a much better fit to the LINER sequence, provided that the shock velocities are not too great. The highest shock velocities have too strong $[O I]\lambda 6300/H\alpha$ ratios.

In conclusion, Seyfert galaxies are not well described by the shock + precursor models. For these, the radiation-pressure dominated photoionization models (Dopita et al. 2002; Groves et al. 2004a,b) provide a much better description of the spectra. The LINERs, on the other hand, fit better to shock only models, and it is likely that at least some of these objects are in fact shock-excited. A good example of a LINER which is known to be shock-excited is the nuclear disk of M87 (Dopita et al. 1997).

6. THE ON-LINE LIBRARY

The complete electronic files that comprise the MAPPINGS III Library of Fast Shock Models are available via the Shock Model Portal of the MAPPINGS online web pages at <http://cdsweb.u-strasbg.fr/~allen/shock.html>. The original MAPPINGS III output files are available for each model in the library. We also provide tables of emission line ratios, and column densities. These files are organized into the various model sets characterized by a given chemical abundance and pre-shock density and then into velocity sequences for a given magnetic field. The files are listed on the online pages using the model names shown in Table 3.

The emission line ratio tables are wavelength ordered lists of the flux ratios of all the emission lines calculated in MAPPINGS III, and are given with respect to $H\beta=1$. Each table contains the ratios for a velocity sequence of models, 100-1000 km s⁻¹, for a given abundance set, density and magnetic field. Shock and precursor components are tabulated separately and we also provide tables of the emission line ratios for the combination of shock+precursor. Each emission line ratio table also includes the absolute luminosity of the $H\beta$ line in units of $\text{Log}_{10}(\text{erg cm}^{-2} \text{s}^{-1})$.

The column density tables contain the integrated model column densities for all of the ionic stages of each of the elements in the corresponding abundance list. Each table includes the column densities for a velocity sequence of models in units of cm^{-2} . Column densities for the shock and precursor components are tabulated separately.

In addition to the tabulated model data, we also provide programs for accessing the library of models, and for generating various plots. These programs are coded using IDL³ and can be used as interactive graphical user interface widgets, and also via the IDL command line. The SHOCKPLOT package allows plotting the models on 2-D line ratio diagrams using any linear combina-

³ <http://www.ittviz.com/idl/>

tion of line ratios. SHOCKPLOT enables quick browsing through the many grids of models, and can also be used as a procedure call from other IDL programs to over-plot model grids on observed line ratio data.

7. SUMMARY

We have presented an extensive library of radiative shock models covering a wide range of shock velocities, magnetic fields, densities and abundances. The shock model predictions for the ionizing radiation, temperatures, and luminosities generated by shocks will be applicable in a wide range of astrophysical situations. The solar abundance models supersede the models of DS96, with model code improvements leading to some differences in the predictions of nitrogen species, and also for models with very low magnetic parameter. Differences in the input abundances result in the most significant variations between the grids of models, and the range and sampling of the shock velocity and magnetic field provides much a more detailed and complete set of model predictions than previously available. The extension to higher shock velocities is important for the analysis of emission line regions of active galaxies where shocks of this speed are expected in jet-cloud interactions (Saxton et al. 2005). At these shock velocities some of the commonly used line ratios such as $[\text{O III}]\lambda 5007/\text{H}\beta$ turn over and do not follow simple extrapolations from the DS96 model grids.

Included as a part of this library, the physical structure of the shocks and their precursors give insight into how the physical parameters of the shock lead to the resulting continuum and line emission. We have included in this paper examples of these, exploring the range of the parameters and demonstrating the effects of these of the density, temperature and ionization structure.

We have presented the model grids on a set of standard UV, optical and IR line ratio diagrams, and we have compared of the new models to the example data sets of radio galaxies and the SDSS sample of narrow emission line galaxies. The updated version of the $\text{C III}\lambda 1909 / [\text{C II}]\lambda 2326$ vs. $[\text{Ne III}]\lambda 3869 / [\text{Ne V}]\lambda 3426$ diagram used by Best et al. (2000) and Inskip et al. (2002) for the analysis of emission line regions of radio galaxies,

shows that some of the 6C sources fall within the new higher velocity shock+precursor grid. This supports the interpretation that the emission line regions in smaller radio sources are excited by shocks. The new library of models presented here, and a more complete set of emission line observations of these sources will allow a much more detailed analysis of the contributions of shock and photoionization in these sources.

Large samples of emission line ratios such as now available from the SDSS provide an extremely valuable resource for classifying and analyzing the emission line excitation mechanisms in active and star-forming galaxies. The comparison of the narrow emission line galaxies sample (compiled by Hao et al. (2005)) to the shock models shows that shocks do predict line ratios in the observed range, and that shocks may indeed provide the best explanation for LINER spectra. This library of shock models, combined with detailed grids of (AGN and star-formation) photoionization models now available should allow a new statistical approach to analyzing the contributions of shocks, star-formation and AGN photoionization to excitation of emission lines in galaxies.

The complete set of electronic files that comprise the library are available on-line, along with tools to assist in the comparison of observations to the model predictions line ratio diagrams. Together this library provides one of the largest databases of radiative shock models and a unique tool in the interpretation and diagnosis of fast shocks.

We thank the anonymous referee for comments which have improved the clarity of this paper. BG would like to thank the Observatoire Astronomique de Strasbourg for their financial support and hospitality. MAD acknowledges the support of both the Australian National University and of the Australian Research Council (ARC) through his (2002-2006) ARC Australian Federation Fellowship, and also under the ARC Discovery projects DP0208445 and DP0342844. Both Dopita and Sutherland acknowledge support under the ARC Discovery project DP0664434.

REFERENCES

- Allen, M. G., Dopita, M. A., & Tsvetanov, Z. I. 1998, *ApJ*, 493, 571
- Allen, M. G., Dopita, M. A., Tsvetanov, Z. I., & Sutherland, R. S. 1999, *ApJ*, 511, 686
- Anders, E. & Grevesse, N. 1989, *Geochimica et Cosmochimica Acta*, 53, 197
- Asplund, M., Grevesse, N., & Sauval, A. J. 2005, in *ASP Conference Series*, Vol. 336 "Cosmic Abundances as Records of Stellar Evolution and Nucleosynthesis", eds. Thomas G. Barnes III and Frank N. Bash. San Francisco: Astronomical Society of the Pacific, p.25
- Baldwin, J. A., Phillips, M. M., & Terlevich, R. 1981, *PASP*, 93, 5
- Best, P. N., Röttgering, H. J. A., & Longair, M. S. 2000, *MNRAS*, 311, 23
- Binette, L., Wilson, A. S., & Storchi-Bergmann, T. 1996, *A&A*, 312, 365
- Bradley, L. D., Kaiser, M. E., & Baan, W. A. 2004, *ApJ*, 603, 463
- De Breuck, C., Röttgering, H., Miley, G., van Breugel, W., & Best, P. 2000, *A&A*, 362, 519
- Dopita, M. A. 1977, *ApJS*, 56, 437
- Dopita, M. A., & Sutherland, R. S. 1995, *ApJ*, 455, 468 (DS95)
- Dopita, M. A., & Sutherland, R. S. 1996, *ApJS*, 102, 161 (DS96)
- Dopita, M. A., Koratkar, A. P., Allen, M. G., Tsvetanov, Z. I., Ford, H. C., Bicknell, G. V., & Sutherland, R. S. 1997, *ApJ*, 490, 202
- Dopita, M. A., Kewley, L. J., & Sutherland, R. S. 2000, *ApJ*, 542, 224
- Dopita, M. A., & Groves, B. A., Sutherland, R. S., Binette, L. & Cecil, G. 2002, *ApJ*, 572, 753
- Dopita, M. A., & Sutherland, R. S. 2003, *Astrophysics of the diffuse universe*, Berlin, New York: Springer, 2003. *Astronomy and astrophysics library*, ISBN 3540433627
- Dopita, M. A., et al. 2005, *ApJ*, 619, 755
- Dopita, M. A., et al. 2006, *ApJS*, 167, 177
- Draine, B. T., & Salpeter, E. E. 1979, *ApJ*, 231, 77
- Dwek, E., Foster, S. M., & Vancura, O. 1996, *ApJ*, 457, 244
- Evans, I., Koratkar, A., Allen, M., Dopita, M., & Tsvetanov, Z. 1999, *ApJ*, 521, 531
- Feinstein, C., Macchetto, F. D., Martel, A. R., Sparks, W. B., & McCarthy, P. J. 1999, *ApJ*, 526, 623
- Ferruit, P., Wilson, A. S., Whittle, M., Simpson, C., Mulchaey, J. S., & Ferland, G. J. 1999, *ApJ*, 523, 147
- Fox, A. J., Savage, B. D., Wakker, B. P., Richter, P., Sembach, K. R., & Tripp, T. M. 2004, *ApJ*, 602, 738
- Genzel, R., et al. 1998, *ApJ*, 498, 579

- Groves, B., Dopita, M., & Sutherland, R. 2006, *A&A*, 458, 405
- Groves, B. A., Cecil, G., Ferruit, P., & Dopita, M. A. 2004, *ApJ*, 611, 786
- Groves, B. A., Dopita, M. A., & Sutherland, R. S. 2004a, *ApJS*, 153, 9
- Groves, B. A., Dopita, M. A., & Sutherland, R. S. 2004b, *ApJS*, 153, 75
- Groves, B. A., et al. in preparation.
- Hao, L., et al. 2005, *AJ*, 129, 1783
- Heng, K., van Adelsberg, M., McCray, R., & Raymond, J. C. 2007, *ApJ*, 668, 275
- Inskip, K. J., Best, P. N., Rawlings, S., Longair, M. S., Cotter, G., Röttgering, H. J. A., & Eales, S. 2002, *MNRAS*, 337, 1381
- Iwamuro, F., et al. 2003, *ApJ*, 598, 178
- Jones, A. P., Tielens, A. G. G. M., Hollenbach, D. J., & McKee, C. F. 1994, *ApJ*, 433, 797
- Jones, A. P., Tielens, A. G. G. M., & Hollenbach, D. J. 1996, *ApJ*, 469, 740
- Kauffmann, G., et al. 2003, *MNRAS*, 346, 1055
- Kewley, L. J., Dopita, M. A., Sutherland, R. S., Heisler, C. A., & Trevena, J. 2001, *ApJ*, 556, 121
- Kewley, L. J., Heisler, C. A., Dopita, M. A., & Lumsden, S. 2001, *ApJS*, 132, 37
- Lutz, D., Sturm, E., Genzel, R., Spoon, H. W. W., Moorwood, A. F. M., Netzer, H., & Sternberg, A. 2003, *A&A*, 409, 867
- Kewley, L. J., Groves, B., Kauffmann, G., & Heckman, T. 2006, *MNRAS*, 372, 961
- Leitherer, C., et al. 1996, *PASP*, 108, 996
- McKee, C. F., & Hollenbach, D. J. 1980, *ARA&A*, 18, 219
- Maxfield, L., Spinrad, H., Stern, D., Dey, A., & Dickinson, M. 2002, *AJ*, 123, 2321
- Nelson, C. H., Weistrop, D., Hutchings, J. B., Crenshaw, D. M., Gull, T. R., Kaiser, M. E., Kraemer, S. B., & Lindler, D. 2000, *ApJ*, 531, 257
- Perna, R., & Lazzati, D. 2002, *ApJ*, 580, 261
- Pineau de Fôrets, G. & Flower, D. 1997, in *IAU Symp.* 178, *Molecules in Astrophysics: Probes & Processes*, ed. E. F. van Dishoeck, (Kluwer:Dordrecht), p113
- Raymond, J. C. 1979, *ApJS*, 39, 1
- Reuland, M. A. et al. 2007, *AJ*, 133, 2607
- Russell, S. C. & Dopita, M. A. 1992, *ApJ*, 384, 508
- Sabra, B. M., Shields, J. C., Ho, L. C., Barth, A. J., & Filippenko, A. V. 2003, *ApJ*, 584, 164
- Saxton, C. J., Bicknell, G. V., Sutherland, R. S., & Midgley, S. 2005, *MNRAS*, 359, 781
- Shull, J. M., Tumlinson, J., & Giroux, M. L. 2003, *ApJ*, 594, L107
- Sturm, E., et al. 2006, *ApJ*, 653, L13
- Sutherland, R. S., Bicknell, G. V., & Dopita, M. A. 1993, *ApJ*, 414, 510
- Sutherland, R. S., & Dopita, M. A. 1993, *ApJS*, 88, 253
- Sutherland, R. S., Bisset, D. K., & Bicknell, G. V. 2003, *ApJS*, 147, 187
- Sutherland, R. S., Bicknell, G. V., & Dopita, M. A. 2003, *ApJ*, 591, 238
- Taniguchi, Y., et al. 2001, *ApJ*, 559, L9
- Tremonti, C. A., et al. 2004, *ApJ*, 613, 898
- Veilleux, S., & Osterbrock, D. E. 1987, *ApJS*, 63, 295
- Villar-Martin, M., Tadhunter, C., & Clark, N. 1997, *A&A*, 323, 21
- Villar-Martin, M., Vernet, J., di Serego Alighieri, S., Fosbury, R., Humphrey, A., & Pentericci, L. 2003, *MNRAS*, 346, 273
- Whittle, M., Rosario, D. J., Silverman, J. D., Nelson, C. H., & Wilson, A. S. 2005, *AJ*, 129, 104

TABLE 3
MODEL PARAMETERS

Model name	B (μG)	B/\sqrt{n} ($\mu\text{G cm}^3/2$)
Solar abundance, $n=1.0$, $v=100,125,\dots,1000$		
M_n1_b0	1.0e-04	1.0e-04
M_n1_b0.5	0.50	0.50
M_n1_b1	1.00	1.00
M_n1_b2	2.00	2.00
M_n1_be	3.23	3.23
M_n1_b4	4.00	4.00
M_n1_b5	5.00	5.00
M_n1_b10	10.0	10.0
Solar $\times 2$ abundance, $n=1.0$, $v=100,125,\dots,1000$		
R_n1_b0	1.0e-04	1.0e-04
R_n1_b0.5	0.50	0.50
R_n1_b1	1.00	1.00
R_n1_b2	2.00	2.00
R_n1_be	3.23	3.23
R_n1_b4	4.00	4.00
R_n1_b5	5.00	5.00
R_n1_b10	10.0	10.0
Dopita 2005 abundance, $n=1.0$, $v=100,125,\dots,1000$		
J_n1_b0	1.0e-04	1.0e-04
J_n1_b0.5	0.50	0.50
J_n1_b1	1.00	1.00
J_n1_b2	2.00	2.00
J_n1_be	3.23	3.23
J_n1_b4	4.00	4.00
J_n1_b5	5.00	5.00
J_n1_b10	10.0	10.0
SMC abundance, $n=1.0$, $v=100,125,\dots,1000$		
P_n1_b0	1.0e-04	1.0e-04
P_n1_b0.5	0.50	0.50
P_n1_b1	1.00	1.00
P_n1_b2	2.00	2.00
P_n1_be	3.23	3.23
P_n1_b4	4.00	4.00
P_n1_b5	5.00	5.00
P_n1_b10	10.0	10.0
LMC abundance, $n=1.0$, $v=100,125,\dots,1000$		
Q_n1_b0	1.0e-04	1.0e-04
Q_n1_b0.5	0.50	0.50
Q_n1_b1	1.00	1.00
Q_n1_b2	2.00	2.00
Q_n1_be	3.23	3.23
Q_n1_b4	4.00	4.00
Q_n1_b5	5.00	5.00
Q_n1_b10	10.0	10.0
solar abundance, $n=0.01$, $v=100,125,\dots,1000$		
T_n0.01_b0.001	0.001	0.010
T_n0.01_b0.01	0.010	0.10
T_n0.01_b0.05	0.050	0.50
T_n0.01_b0.1	0.10	1.00
T_n0.01_b0.2	0.20	2.00
T_n0.01_b0.4	0.40	4.00
T_n0.01_b0.5	0.50	5.00
T_n0.01_b1	1.0	10.0
T_n0.01_b10	10.0	100
solar abundance, $n=0.1$, $v=100,125,\dots,1000$		
U_n0.1_b0.0001	1.0e-04	0.000316
U_n0.1_b0.001	0.001	0.00316
U_n0.1_b0.01	0.01	0.0316
U_n0.1_b0.05	0.05	0.158
U_n0.1_b0.1	0.10	0.316
U_n0.1_b0.2	0.20	0.632
U_n0.1_b0.32	0.32	1.01
U_n0.1_b0.4	0.40	1.26

TABLE 3 — *Continued*

Model name	B (μG)	B/\sqrt{n} ($\mu\text{G cm}^{3/2}$)
U_n0.1_b0.5	0.50	1.58
U_n0.1_b0.632	0.63	2.00
U_n0.1_b1.0	1.00	3.16
U_n0.1_b1.26	1.26	4.00
U_n0.1_b1.58	1.58	5.00
U_n0.1_b2.0	2.00	6.32
U_n0.1_b3.16	3.16	10.0
U_n0.1_b4.0	4.00	12.6
U_n0.1_b5.0	5.00	15.8
U_n0.1_b10	10.0	31.6
solar abundance, n=10.0, v=100,125,...1000		
V_n10_b0.001	0.001	0.000316
V_n10_b0.01	0.01	0.00316
V_n10_b0.1	0.10	0.0316
V_n10_b1	1.00	0.316
V_n10_b1.58	1.58	0.500
V_n10_b3.16	3.16	1.00
V_n10_b5	5.00	1.58
V_n10_b6.32	6.32	2.00
V_n10_b10	10.0	3.16
V_n10_b10.2	10.2	3.23
V_n10_b12.65	12.6	4.00
V_n10_b15.8	15.8	5.00
V_n10_b20	20.0	6.32
V_n10_b30	30.0	9.49
V_n10_b40	40.0	12.6
V_n10_b50	50.0	15.8
V_n10_b100	100	31.6
solar abundance, n=100, v=100,125,...1000		
L_n100_b0.001	0.001	0.0001
L_n100_b0.01	0.01	0.001
L_n100_b0.1	0.10	0.010
L_n100_b1	1.00	0.10
L_n100_b5	5.0	0.50
L_n100_b10	10.0	1.00
L_n100_b20	20.0	2.00
L_n100_b40	40.0	4.00
L_n100_b50	50.0	5.00
L_n100_b100	100	10.0
solar abundance, n=1000, v=100,125,...1000		
S_n1000_b0.01	0.01	0.000316
S_n1000_b0.1	0.1	0.00316
S_n1000_b1	1.0	0.0316
S_n1000_b5	5.00	0.158
S_n1000_b10	10.0	0.316
S_n1000_b16	16.0	0.51
S_n1000_b32	32.00	1.01
S_n1000_b63	63.00	2.00
S_n1000_b100	100.0	3.16
S_n1000_b126	126.0	4.00
S_n1000_b160	160.0	5.06
S_n1000_b316	316.0	10.0
S_n1000_b1000	1000	31.6

TABLE 4
INTEGRATED COLUMN DENSITIES FOR SOLAR ABUNDANCE MODELS, N=1.0,
B=3.23

V=200	H	He	C	N	O	Ne	Mg	Al	Si	S	Ar	Ca	Fe
I	4.771E+18	4.745E+17	9.812E+13	5.334E+14	4.286E+15	2.376E+14	9.506E+13	7.978E+11	3.265E+12	3.178E+11	3.083E+12	5.587E+12	7.278E+12
II	8.275E+18	5.560E+17	3.604E+15	6.686E+14	4.875E+15	9.445E+14	1.954E+14	2.849E+13	3.708E+14	1.361E+14	2.913E+13	5.947E+12	1.803E+14
III	0.	2.444E+17	2.138E+14	9.468E+12	8.270E+13	1.640E+14	1.223E+14	1.836E+12	7.185E+12	3.884E+13	7.223E+12	2.812E+12	5.884E+13
IV	0.	0.	9.258E+12	3.141E+12	7.130E+13	3.353E+13	1.062E+13	1.090E+12	6.375E+11	5.825E+11	3.989E+11	3.556E+11	6.636E+12
V	0.	0.	8.096E+14	8.003E+12	9.384E+13	9.124E+13	2.490E+13	2.312E+12	1.639E+13	4.817E+11	4.554E+11	5.272E+11	5.019E+12
VI	0.	0.	1.466E+12	2.411E+14	2.154E+14	9.982E+13	3.827E+13	2.780E+12	5.026E+13	8.279E+11	5.534E+11	8.970E+11	1.850E+13
VII	0.	0.	2.691E+07	3.517E+09	1.479E+15	3.349E+13	8.895E+12	1.143E+12	1.346E+13	3.285E+13	7.710E+11	7.485E+11	2.034E+13
VIII	0.	0.	0.	392.	7.578E+07	6.668E+11	4.744E+11	5.668E+10	8.241E+11	1.546E+12	6.290E+11	2.732E+11	8.302E+12
IX	0.	0.	0.	0.	0.	9.882E+10	4.098E+09	4.896E+08	5.974E+09	1.080E+10	5.118E+12	4.342E+10	5.829E+11
X	0.	0.	0.	0.	0.	9.599E-03	1.339E+07	5.513E+05	6.303E+06	1.028E+07	2.164E+09	4.174E+09	1.049E+10
XI	0.	0.	0.	0.	0.	0.	1.731E+04	0.346	3.483E-10	458.	1.245E+05	2.375E+09	1.145E+08
XII	0.	0.	0.	0.	0.	0.	0.	0.	0.	0.	0.	7.354E+03	3.437E+05
XIII	0.	0.	0.	0.	0.	0.	0.	0.	0.	0.	0.	0.	691.
XIV	0.	0.	0.	0.	0.	0.	0.	0.	0.	0.	0.	0.	0.
V=500	H	He	C	N	O	Ne	Mg	Al	Si	S	Ar	Ca	Fe
I	1.691E+20	1.393E+19	1.645E+14	1.868E+16	1.447E+17	3.288E+15	5.336E+14	2.179E+12	1.214E+13	7.472E+11	1.272E+14	6.354E+12	4.911E+13
II	3.595E+20	5.446E+18	6.777E+16	4.060E+15	2.670E+16	1.283E+16	4.240E+15	5.956E+14	7.183E+15	1.690E+15	5.393E+14	4.291E+13	4.081E+15
III	0.	3.228E+19	6.639E+15	3.179E+14	3.496E+15	9.174E+15	3.040E+15	5.101E+12	7.374E+13	1.639E+15	7.958E+13	2.074E+14	5.038E+14
IV	0.	0.	5.160E+13	8.445E+12	1.630E+14	2.742E+13	7.505E+12	3.520E+12	2.195E+13	3.829E+12	5.183E+11	1.360E+13	1.671E+14
V	0.	0.	1.582E+15	8.530E+12	3.537E+13	3.987E+13	1.218E+13	1.532E+12	8.400E+12	4.092E+11	2.159E+11	1.179E+12	2.069E+13
VI	0.	0.	7.674E+15	2.059E+15	3.511E+14	7.120E+13	4.045E+13	2.269E+12	3.645E+13	4.455E+11	1.948E+11	4.021E+11	1.167E+13
VII	0.	0.	1.080E+17	6.578E+15	5.399E+16	1.276E+14	7.112E+13	6.610E+12	6.678E+13	3.404E+13	2.149E+11	5.050E+11	3.001E+13
VIII	0.	0.	0.	2.760E+16	1.009E+17	3.080E+14	9.916E+13	1.173E+13	1.598E+14	5.995E+13	3.221E+11	4.466E+11	7.183E+13
IX	0.	0.	0.	0.	1.196E+17	2.941E+16	9.537E+13	1.530E+13	3.196E+14	1.190E+14	3.318E+13	3.413E+11	8.945E+13
X	0.	0.	0.	0.	0.	9.101E+15	4.634E+14	1.409E+13	7.834E+14	2.558E+14	4.313E+13	7.012E+11	1.012E+14
XI	0.	0.	0.	0.	0.	6.612E+14	1.125E+16	6.150E+13	2.222E+15	3.424E+14	8.267E+13	3.582E+13	1.236E+14
XII	0.	0.	0.	0.	0.	0.	2.397E+14	8.369E+14	7.505E+14	4.629E+14	2.018E+14	5.329E+13	1.442E+14
XIII	0.	0.	0.	0.	0.	0.	7.814E+11	3.668E+12	7.111E+15	4.898E+14	2.720E+14	9.393E+13	2.019E+14
XIV	0.	0.	0.	0.	0.	0.	0.	2.310E+09	6.598E+12	1.086E+15	2.349E+14	1.259E+14	2.027E+14
XV	0.	0.	0.	0.	0.	0.	0.	0.	7.767E+08	2.389E+15	1.205E+14	7.731E+13	3.087E+14
XVI	0.	0.	0.	0.	0.	0.	0.	0.	0.	6.630E+10	1.146E+14	2.961E+13	6.709E+14
XVII	0.	0.	0.	0.	0.	0.	0.	0.	0.	2.104E+05	6.890E+13	5.633E+12	4.895E+15
XVIII	0.	0.	0.	0.	0.	0.	0.	0.	0.	0.	5.618E+07	1.329E+12	6.709E+14
XIX	0.	0.	0.	0.	0.	0.	0.	0.	0.	0.	0.	1.834E+11	4.623E+13
XX	0.	0.	0.	0.	0.	0.	0.	0.	0.	0.	0.	2.735E+03	1.513E+12
XXI	0.	0.	0.	0.	0.	0.	0.	0.	0.	0.	0.	0.	1.668E+10
XXII	0.	0.	0.	0.	0.	0.	0.	0.	0.	0.	0.	0.	1.074E+08
XXIII	0.	0.	0.	0.	0.	0.	0.	0.	0.	0.	0.	0.	4.021E+05
XXIV	0.	0.	0.	0.	0.	0.	0.	0.	0.	0.	0.	0.	631.
XXV	0.	0.	0.	0.	0.	0.	0.	0.	0.	0.	0.	0.	0.748
V=1000	H	He	C	N	O	Ne	Mg	Al	Si	S	Ar	Ca	Fe
I	1.155E+21	1.037E+20	1.239E+15	1.294E+17	9.895E+17	1.790E+16	2.886E+15	7.454E+12	5.299E+13	7.066E+12	1.046E+15	2.790E+13	2.490E+14
II	5.182E+21	2.248E+19	4.561E+17	1.648E+16	1.113E+17	8.702E+16	3.268E+16	3.832E+15	4.600E+16	1.263E+16	3.563E+15	3.042E+14	2.670E+16
III	0.	4.931E+20	1.707E+16	7.406E+14	1.104E+16	5.579E+16	1.411E+16	8.313E+12	1.966E+14	8.538E+15	1.363E+14	1.327E+15	3.314E+15
IV	0.	0.	1.306E+14	2.681E+13	6.054E+14	1.092E+14	2.608E+13	6.004E+12	1.209E+14	2.059E+13	9.671E+11	5.413E+13	3.245E+14
V	0.	0.	7.762E+14	8.459E+12	7.118E+13	3.062E+13	9.145E+12	3.753E+12	9.651E+12	1.603E+12	1.651E+11	9.494E+12	4.767E+13
VI	0.	0.	7.591E+15	9.491E+14	1.772E+14	4.771E+13	2.410E+13	1.630E+12	2.513E+13	9.129E+11	1.695E+11	5.678E+11	1.022E+13
VII	0.	0.	1.818E+18	7.068E+15	2.644E+16	5.922E+13	3.919E+13	3.621E+12	3.753E+13	1.955E+13	2.838E+11	3.288E+11	1.781E+13
VIII	0.	0.	0.	5.564E+17	1.392E+17	2.570E+14	5.023E+13	5.999E+12	8.105E+13	3.215E+13	2.036E+11	2.867E+11	3.898E+13
IX	0.	0.	0.	0.	4.115E+18	3.012E+16	4.592E+13	7.334E+12	1.521E+14	5.775E+13	1.649E+13	1.944E+11	4.592E+13
X	0.	0.	0.	0.	0.	8.210E+16	8.303E+14	7.369E+12	3.740E+14	1.172E+14	2.059E+13	3.205E+11	4.982E+13
XI	0.	0.	0.	0.	0.	5.062E+17	3.787E+16	1.427E+14	1.990E+15	1.511E+14	3.660E+13	1.593E+13	5.858E+13
XII	0.	0.	0.	0.	0.	0.	5.653E+16	4.898E+15	2.956E+15	2.058E+14	8.579E+13	2.392E+13	6.610E+13

TABLE 4 — *Continued*

XIII	0.	0.	0.	0.	0.	0.	9.584E+16	5.155E+15	8.485E+16	3.104E+14	1.259E+14	4.419E+13	9.124E+13
XIV	0.	0.	0.	0.	0.	0.	0.	4.623E+15	6.004E+16	3.959E+15	1.494E+14	8.034E+13	9.065E+13
XV	0.	0.	0.	0.	0.	0.	0.	0.	2.796E+16	6.014E+16	1.810E+14	9.811E+13	1.469E+14
XVI	0.	0.	0.	0.	0.	0.	0.	0.	0.	1.489E+16	1.731E+15	1.292E+14	4.983E+14
XVII	0.	0.	0.	0.	0.	0.	0.	0.	0.	1.691E+15	1.480E+16	1.803E+14	6.596E+15
XVIII	0.	0.	0.	0.	0.	0.	0.	0.	0.	0.	1.088E+15	1.033E+15	7.854E+15
XIX	0.	0.	0.	0.	0.	0.	0.	0.	0.	0.	2.805E+13	4.900E+15	1.071E+16
XX	0.	0.	0.	0.	0.	0.	0.	0.	0.	0.	0.	1.231E+14	1.434E+16
XXI	0.	0.	0.	0.	0.	0.	0.	0.	0.	0.	0.	7.223E+11	1.477E+16
XXII	0.	0.	0.	0.	0.	0.	0.	0.	0.	0.	0.	0.	1.458E+16
XXIII	0.	0.	0.	0.	0.	0.	0.	0.	0.	0.	0.	0.	1.996E+16
XXIV	0.	0.	0.	0.	0.	0.	0.	0.	0.	0.	0.	0.	1.466E+16
XXV	0.	0.	0.	0.	0.	0.	0.	0.	0.	0.	0.	0.	1.334E+16
XXVI	0.	0.	0.	0.	0.	0.	0.	0.	0.	0.	0.	0.	3.648E+12
XXVII	0.	0.	0.	0.	0.	0.	0.	0.	0.	0.	0.	0.	1.857E+08

TABLE 5
INTEGRATED COLUMN DENSITIES FOR THE PRECURSOR COMPONENT OF SOLAR
ABUNDANCE MODELS, N=1.0, B=3.23

V=200	H	He	C	N	O	Ne	Mg	Al	Si	S	Ar	Ca	Fe
I	8.836E+19	8.699E+18	4.030E+15	9.792E+15	7.582E+16	8.448E+15	1.350E+14	2.057E+11	1.271E+12	1.935E+11	1.637E+14	3.158E+12	1.500E+12
II	1.198E+20	1.127E+19	4.675E+16	7.516E+15	7.372E+16	9.629E+15	4.418E+15	3.741E+14	5.617E+15	1.536E+15	2.199E+14	2.774E+13	2.343E+15
III	0.	3.756E+17	2.471E+16	5.905E+15	2.685E+16	7.473E+15	3.305E+15	1.799E+14	1.247E+15	1.765E+15	3.684E+14	2.278E+14	1.594E+15
IV	0.	0.	1.052E+14	1.471E+14	8.204E+14	6.430E+13	5.709E+13	5.960E+13	5.124E+14	7.515E+13	4.014E+12	1.520E+13	9.311E+14
V	0.	0.	9.281E+11	4.191E+11	4.332E+12	2.582E+11	1.521E+11	6.680E+11	9.974E+12	4.006E+11	5.185E+09	5.757E+11	1.105E+13
VI	0.	0.	1.429E+05	9.819E+08	3.015E+09	1.112E+08	1.138E+08	5.264E+08	1.494E+10	1.158E+10	1.928E+07	1.834E+09	6.478E+10
VII	0.	0.	0.	0.	0.	0.	0.	2.240E+04	3.348E+05	8.522E+05	2.597E+04	6.880E+05	1.057E+08
V=500	H	He	C	N	O	Ne	Mg	Al	Si	S	Ar	Ca	Fe
I	3.923E+21	3.676E+20	9.843E+15	4.300E+17	3.322E+18	2.010E+17	3.353E+14	3.900E+11	2.609E+12	4.559E+11	6.127E+15	8.244E+11	1.177E+13
II	2.134E+21	1.688E+20	1.490E+18	4.651E+16	2.496E+17	2.103E+17	1.361E+17	1.280E+16	1.510E+17	4.937E+16	9.052E+15	4.467E+13	9.166E+16
III	0.	5.563E+19	3.977E+17	8.208E+16	1.088E+18	2.747E+17	5.874E+16	1.473E+14	1.658E+15	2.348E+16	2.249E+15	6.091E+15	8.385E+15
IV	0.	0.	1.280E+17	9.142E+16	3.732E+17	4.007E+16	1.562E+16	1.884E+15	1.431E+16	1.683E+16	3.971E+15	1.158E+15	3.125E+16
V	0.	0.	1.596E+17	1.415E+16	8.908E+16	1.707E+16	1.177E+16	1.954E+15	2.236E+16	4.867E+15	5.156E+14	5.959E+14	8.587E+15
VI	0.	0.	1.412E+16	1.475E+16	3.122E+16	2.027E+15	5.601E+15	9.322E+14	1.997E+16	3.629E+15	7.041E+13	8.656E+13	1.861E+15
VII	0.	0.	2.303E+14	7.781E+14	2.508E+15	9.202E+12	1.897E+15	1.379E+14	5.318E+15	4.522E+13	8.022E+12	7.946E+12	2.311E+14
VIII	0.	0.	0.	3.292E+12	2.088E+13	2.861E+11	2.077E+14	2.284E+13	3.325E+14	1.316E+13	9.636E+10	5.233E+11	1.628E+13
IX	0.	0.	0.	0.	1.810E+10	6.851E+09	4.352E+12	8.903E+11	1.887E+13	8.379E+11	7.297E+08	1.572E+10	6.101E+11
X	0.	0.	0.	0.	0.	0.	5.528E+10	8.765E+09	3.715E+11	1.191E+10	5.742E+07	8.657E+07	2.423E+10
XI	0.	0.	0.	0.	0.	0.	2.444E+08	4.969E+07	1.768E+09	2.439E+08	1.302E+06	1.864E+05	9.224E+07
XII	0.	0.	0.	0.	0.	0.	0.	1.431E+05	5.939E+06	2.380E+06	8.874E+03	4.899E+03	4.744E+04
XIII	0.	0.	0.	0.	0.	0.	0.	0.	1.078E+04	5.912E+03	69.6	23.8	78.0
XIV	0.	0.	0.	0.	0.	0.	0.	0.	0.	11.5	0.132	2.108E-02	9.953E-02
XV	0.	0.	0.	0.	0.	0.	0.	0.	0.	0.	0.	2.409E-05	0.
V=1000	H	He	C	N	O	Ne	Mg	Al	Si	S	Ar	Ca	Fe
I	3.711E+22	3.599E+21	5.026E+15	4.214E+18	3.187E+19	2.568E+18	1.684E+14	2.034E+11	1.355E+12	1.640E+11	7.177E+16	5.669E+09	6.059E+12
II	1.165E+22	6.939E+20	1.415E+19	2.041E+17	1.591E+18	1.583E+18	1.272E+18	1.167E+17	1.394E+18	5.163E+17	7.005E+16	9.875E+12	8.638E+17
III	0.	4.722E+20	6.107E+17	8.576E+16	2.672E+18	1.105E+18	2.865E+17	1.564E+14	2.784E+15	1.231E+17	3.955E+15	5.201E+16	5.999E+16
IV	0.	0.	3.272E+17	2.090E+17	1.041E+18	1.308E+17	4.236E+16	3.643E+15	1.659E+16	4.578E+16	1.681E+16	4.763E+15	1.064E+17
V	0.	0.	1.055E+18	8.139E+16	1.134E+18	2.714E+17	3.561E+16	5.219E+15	5.125E+16	1.984E+16	2.512E+15	1.945E+15	1.720E+16
VI	0.	0.	1.284E+18	3.894E+17	1.525E+18	3.198E+17	4.021E+16	4.439E+15	7.136E+16	2.582E+16	3.146E+15	1.468E+15	1.826E+16
VII	0.	0.	2.683E+17	2.619E+17	1.260E+18	1.640E+16	7.340E+16	3.461E+15	7.833E+16	4.853E+15	7.444E+15	1.755E+15	3.025E+16
VIII	0.	0.	0.	2.588E+16	3.918E+17	4.008E+15	7.667E+16	5.970E+15	5.138E+16	2.269E+16	9.964E+14	1.680E+15	2.729E+16
IX	0.	0.	0.	0.	1.916E+16	1.325E+15	2.119E+16	3.668E+15	4.620E+16	2.376E+16	1.095E+14	6.088E+14	1.274E+16
X	0.	0.	0.	0.	0.	3.607E+13	5.216E+15	6.005E+14	1.639E+16	6.145E+15	1.663E+14	3.904E+13	6.620E+15
XI	0.	0.	0.	0.	0.	1.792E+11	4.759E+14	7.096E+13	1.380E+15	2.123E+15	7.028E+13	1.185E+12	4.243E+14
XII	0.	0.	0.	0.	0.	0.	2.139E+12	3.989E+12	9.250E+13	3.101E+14	8.348E+12	8.244E+11	4.262E+12
XIII	0.	0.	0.	0.	0.	0.	1.609E+09	4.506E+09	3.189E+12	1.289E+13	1.452E+12	1.142E+11	1.425E+11
XIV	0.	0.	0.	0.	0.	0.	0.	0.	1.494E+09	6.780E+11	8.089E+10	4.113E+09	4.040E+09
XV	0.	0.	0.	0.	0.	0.	0.	0.	0.	1.078E+10	1.054E+09	1.893E+08	6.014E+07
XVI	0.	0.	0.	0.	0.	0.	0.	0.	0.	0.	1.465E+07	3.442E+06	1.810E+04
XVII	0.	0.	0.	0.	0.	0.	0.	0.	0.	0.	7.387E+04	1.705E+04	28.9
XVIII	0.	0.	0.	0.	0.	0.	0.	0.	0.	0.	0.	58.0	0.290
XIX	0.	0.	0.	0.	0.	0.	0.	0.	0.	0.	0.	5.533E-02	7.180E-04
XX	0.	0.	0.	0.	0.	0.	0.	0.	0.	0.	0.	0.	5.351E-07
XXI	0.	0.	0.	0.	0.	0.	0.	0.	0.	0.	0.	0.	5.694E-10

TABLE 6
 LINE RATIOS FOR SHOCK COMPONENTS OF SOLAR ABUNDANCE MODELS, $n=1.0$,
 $B=3.23$

Line	Shock Velocity (km s ⁻¹)									
	100	200	300	400	500	600	700	800	900	1000
C III $\lambda 977$	11.300	0.987	0.463	0.314	0.244	0.194	0.161	0.139	0.121	0.107
N III $\lambda 991$	2.919	0.620	0.348	0.225	0.174	0.140	0.116	0.099	0.085	0.074
O VI $\lambda\lambda 1032, 1037$	0.000	51.100	28.835	22.357	18.281	14.626	11.860	10.072	8.643	7.506
Ly α $\lambda 1215$	43.570	28.720	28.820	33.040	34.360	37.500	42.800	49.360	55.710	60.000
N V $\lambda 1240$	0.012	1.349	0.777	0.522	0.382	0.298	0.242	0.207	0.177	0.154
Si IV + O IV $\lambda 1400$	4.681	2.411	1.298	0.924	0.703	0.574	0.477	0.416	0.370	0.332
N IV $\lambda 1486$	0.208	0.122	0.064	0.048	0.035	0.028	0.022	0.020	0.017	0.016
C IV $\lambda 1550$	15.032	4.593	2.262	1.398	1.044	0.825	0.677	0.578	0.498	0.436
He II $\lambda 1640$	0.469	0.479	1.010	2.921	2.204	1.774	1.647	1.678	1.812	1.822
O III] $\lambda 1664$	1.735	0.711	0.425	0.304	0.252	0.214	0.182	0.162	0.149	0.137
N III $\lambda 1750$	0.400	0.084	0.051	0.038	0.032	0.027	0.024	0.022	0.021	0.021
C III] $\lambda 1909$	5.621	0.722	0.574	0.816	0.854	0.814	0.820	0.875	0.985	1.027
C II] $\lambda 2326$	2.031	0.438	0.559	0.696	0.754	0.955	1.207	1.464	1.661	1.797
Mg II $\lambda 2800$	0.584	0.563	1.343	1.744	1.952	2.492	2.926	3.463	3.846	4.326
[Ne V] $\lambda 3426$	2.074e-5	0.288	0.156	0.099	0.077	0.064	0.055	0.048	0.043	0.038
[Ne III] $\lambda 3869$	0.612	0.309	0.694	1.253	1.312	1.414	1.577	1.767	1.956	2.058
[O II] $\lambda\lambda 3727, 3729$	10.652	5.964	11.045	14.156	14.601	14.141	14.230	14.770	15.428	15.446
[S II] $\lambda\lambda 4067, 4076$	0.066	0.057	0.109	0.138	0.133	0.144	0.160	0.177	0.189	0.200
[O III] $\lambda 4363$	0.290	0.115	0.073	0.061	0.055	0.050	0.045	0.044	0.045	0.045
He II $\lambda 4686$	0.039	0.060	0.154	0.452	0.337	0.269	0.249	0.253	0.273	0.274
H β $\lambda 4861$	1.000	1.000	1.000	1.000	1.000	1.000	1.000	1.000	1.000	1.000
[O III] $\lambda 5007$	3.190	1.188	1.253	2.688	3.045	3.060	3.039	3.167	3.490	3.714
[N I] $\lambda 5200$	0.109	0.080	0.242	0.292	0.462	0.968	1.428	1.793	2.005	2.206
[Fe VII] $\lambda 6085$	0.000	0.013	0.015	0.010	0.008	0.006	0.005	0.004	0.004	0.003
[O I] $\lambda 6300$	0.145	0.242	0.896	1.225	1.531	2.467	3.365	4.112	4.599	4.998
H α $\lambda 6563$	3.214	3.010	2.938	2.936	2.947	2.968	2.999	3.029	3.060	3.082
[N II] $\lambda 6583$	1.641	2.024	4.155	5.103	5.056	4.871	4.870	5.040	5.265	5.269
[S II] $\lambda\lambda 6716, 6731$	1.445	1.975	2.919	3.200	3.050	3.504	4.066	4.543	4.801	5.074
[O II] $\lambda\lambda 7318, 7324$	0.449	0.170	0.195	0.247	0.264	0.261	0.272	0.292	0.318	0.326
[S III] $\lambda\lambda 9069, 9532$	0.751	0.840	2.421	3.227	3.896	4.871	5.672	6.311	6.763	7.046
Br α $\lambda 4.051\mu\text{m}$	0.112	0.096	0.087	0.084	0.085	0.086	0.087	0.087	0.086	0.086
[Ar VI] $\lambda 4.530\mu\text{m}$	0.000	0.000	0.000	0.000	9.454e-5	7.785e-5	6.537e-5	5.679e-5	4.948e-5	4.345e-5
[Ar II] $\lambda 6.983\mu\text{m}$	0.089	0.092	0.080	0.080	0.107	0.171	0.222	0.252	0.267	0.280
[Ar III] $\lambda 6.983\mu\text{m}$	0.038	0.114	0.300	0.339	0.334	0.302	0.273	0.256	0.248	0.239
[Ne VI] $\lambda 7.652\mu\text{m}$	0.000	0.014	0.011	0.007	0.005	0.004	0.004	0.003	0.003	0.002
[S IV] $\lambda 10.44\mu\text{m}$	0.022	0.011	0.016	0.041	0.053	0.064	0.077	0.093	0.112	0.129
[Ne II] $\lambda 12.8\mu\text{m}$	0.628	0.840	0.741	0.569	0.907	1.543	2.028	2.224	2.293	2.390
[Ne V] $\lambda 14.5\mu\text{m}$	0.000	0.013	0.007	0.004	0.004	0.003	0.003	0.002	0.002	0.002
[Ne III] $\lambda 15.5\mu\text{m}$	0.310	0.446	2.230	3.229	3.435	3.936	4.427	4.799	5.088	5.291
[S III] $\lambda 18.7\mu\text{m}$	0.269	0.440	1.052	1.298	1.647	2.094	2.402	2.594	2.712	2.783
[O IV] $\lambda 25.9\mu\text{m}$	0.083	0.134	0.097	0.347	0.344	0.348	0.370	0.433	0.556	0.655
log ₁₀ H β (erg cm ⁻² s ⁻¹)	-5.317	-4.444	-3.996	-3.675	-3.469	-3.303	-3.155	-3.032	-2.918	-2.814

TABLE 7
LINE RATIOS FOR PRECURSOR COMPONENTS OF SOLAR ABUNDANCE MODELS,
N=1.0, B=3.23

Line	Shock Velocity (km s ⁻¹)								
	200	300	400	500	600	700	800	900	1000
C III λ 977	0.000	7.075e-5	0.001	0.009	0.075	0.200	0.275	0.288	0.285
N III λ 991	0.000	1.013e-5	0.000	0.002	0.015	0.038	0.053	0.050	0.050
O VI $\lambda\lambda$ 1032, 1037	0.000	0.000	0.000	0.011	0.653	4.650	12.084	22.156	30.910
Ly α λ 1215	19.540	19.610	20.190	22.220	26.280	30.870	34.090	37.440	41.390
N V λ 1240	0.000	0.000	6.491e-5	0.014	0.217	0.673	1.055	1.333	1.468
Si IV + O IV λ 1400	1.099e-5	0.002	0.012	0.117	0.689	1.396	1.831	2.089	2.464
N IV λ 1486	0.000	0.000	0.002	0.047	0.241	0.431	0.515	0.547	0.570
C IV λ 1550	0.000	0.003	0.035	1.206	5.764	10.272	12.136	12.485	12.526
He II λ 1640	0.263	1.425	3.617	2.246	2.091	2.358	2.625	3.033	3.162
O III] λ 1664	9.984e-5	0.005	0.030	0.150	0.558	1.040	1.430	1.638	1.892
N III] λ 1750	5.054e-5	0.001	0.006	0.021	0.054	0.076	0.080	0.065	0.058
C III] λ 1909	0.004	0.085	0.298	1.022	2.113	2.806	2.860	2.630	2.408
C II] λ 2326	0.012	0.036	0.063	0.137	0.210	0.266	0.293	0.324	0.381
Mg II λ 2800	0.107	0.290	0.410	0.716	0.923	1.020	1.032	1.047	1.111
[Ne V] λ 3426	0.000	0.001	0.004	0.147	0.686	1.484	2.089	2.631	2.825
[Ne III] λ 3869	0.052	0.310	0.569	1.310	2.070	2.471	2.636	2.584	2.569
[O II] $\lambda\lambda$ 3727, 3729	1.119	1.241	1.065	1.160	1.316	1.416	1.415	1.416	1.526
[S II] $\lambda\lambda$ 4067, 4076	0.005	0.006	0.007	0.014	0.018	0.022	0.026	0.030	0.036
[O III] λ 4363	0.000	0.009	0.034	0.120	0.298	0.448	0.549	0.586	0.638
He II λ 4686	0.045	0.234	0.603	0.340	0.300	0.327	0.357	0.407	0.420
H β λ 4861	1.000	1.000	1.000	1.000	1.000	1.000	1.000	1.000	1.000
[O III] λ 5007	0.661	4.594	7.639	16.270	23.960	26.920	27.860	26.760	26.760
[N I] λ 5200	0.004	0.021	0.057	0.142	0.203	0.255	0.294	0.343	0.420
[Fe VII] λ 6085	0.000	0.000	7.858e-5	0.003	0.021	0.078	0.142	0.199	0.205
[O I] λ 6300	0.013	0.062	0.131	0.316	0.463	0.571	0.633	0.708	0.829
H α λ 6563	3.011	2.961	2.943	2.873	2.876	2.899	2.922	2.947	2.976
[N II] λ 6583	0.650	0.465	0.325	0.375	0.442	0.475	0.460	0.443	0.449
[S II] $\lambda\lambda$ 6716, 6731	0.244	0.165	0.180	0.334	0.426	0.526	0.613	0.715	0.855
[O II] $\lambda\lambda$ 7318, 7324	0.006	0.014	0.016	0.019	0.024	0.027	0.027	0.027	0.029
[S III] $\lambda\lambda$ 9069, 9532	1.056	1.299	0.965	1.014	1.025	1.003	0.950	0.903	0.922
Br α λ 4.051 μ m	0.102	0.094	0.092	0.081	0.076	0.073	0.072	0.070	0.069
[Ar VI] λ 4.530 μ m	0.000	3.302e-5	0.001	0.003	0.008	0.019	0.028	0.033	0.034
[Ar II] λ 6.983 μ m	0.013	0.006	0.008	0.015	0.018	0.022	0.024	0.027	0.031
[Ar III] λ 6.983 μ m	0.264	0.282	0.159	0.130	0.109	0.090	0.075	0.060	0.051
[Ne VI] λ 7.652 μ m	0.000	0.000	0.004	0.031	0.138	0.373	0.633	0.929	1.153
[S IV] λ 10.44 μ m	0.144	1.993	3.005	3.303	3.149	2.851	2.588	2.298	2.167
[Ne II] λ 12.8 μ m	0.357	0.091	0.066	0.107	0.116	0.133	0.155	0.181	0.216
[Ne V] λ 14.5 μ m	1.702e-5	0.007	0.036	0.098	0.196	0.302	0.363	0.417	0.419
[Ne III] λ 15.5 μ m	1.147	2.148	2.006	2.321	2.390	2.281	2.143	1.947	1.849
[S III] λ 18.7 μ m	0.848	0.667	0.367	0.334	0.315	0.300	0.284	0.273	0.283
[O IV] λ 25.9 μ m	0.342	5.524	15.890	12.550	12.190	11.330	10.150	9.131	8.604
log ₁₀ H β (erg cm ⁻² s ⁻¹)	-4.622	-4.130	-3.769	-3.599	-3.464	-3.359	-3.261	-3.164	-3.082

TABLE 8
 LINE RATIOS FOR SHOCK + PRECURSOR COMPONENTS OF SOLAR ABUNDANCE
 MODELS, N=1.0, B=3.23

Line	Shock Velocity (km s ⁻¹)								
	200	300	400	500	600	700	800	900	1000
C III λ 977	0.593	0.267	0.174	0.144	0.146	0.176	0.189	0.182	0.169
N III λ 991	0.373	0.201	0.125	0.101	0.089	0.086	0.082	0.072	0.066
O VI $\lambda\lambda$ 1032, 1037	30.700	16.634	12.392	10.507	8.917	9.088	10.818	13.538	15.709
Ly α λ 1215	25.055	24.923	27.313	29.194	32.916	38.213	43.695	49.091	53.477
N V λ 1240	0.810	0.448	0.289	0.225	0.265	0.408	0.521	0.596	0.615
Si IV + O IV λ 1400	1.448	0.750	0.517	0.454	0.621	0.830	0.941	0.993	1.079
N IV λ 1486	0.073	0.037	0.028	0.040	0.115	0.180	0.203	0.209	0.210
C IV λ 1550	2.759	1.306	0.791	1.113	2.843	4.366	4.866	4.841	4.674
He II λ 1640	0.393	1.186	3.231	2.222	1.904	1.920	2.029	2.254	2.292
O III] λ 1664	0.427	0.247	0.182	0.208	0.354	0.511	0.632	0.688	0.752
N III λ 1750	0.051	0.030	0.024	0.027	0.038	0.044	0.044	0.037	0.034
C III] λ 1909	0.436	0.367	0.586	0.925	1.345	1.583	1.612	1.581	1.511
C II] λ 2326	0.268	0.338	0.414	0.492	0.650	0.845	1.029	1.176	1.301
Mg II λ 2800	0.381	0.898	1.149	1.426	1.851	2.193	2.561	2.832	3.199
[Ne V] λ 3426	0.173	0.091	0.056	0.107	0.318	0.604	0.805	0.981	1.015
[Ne III] λ 3869	0.207	0.532	0.948	1.311	1.682	1.921	2.089	2.184	2.237
[O II] $\lambda\lambda$ 3727, 3729	4.030	6.897	8.321	8.882	8.902	9.304	9.815	10.352	10.567
[S II] $\lambda\lambda$ 4067, 4076	0.036	0.066	0.080	0.082	0.092	0.107	0.121	0.132	0.142
[O III] λ 4363	0.070	0.046	0.049	0.083	0.151	0.200	0.231	0.241	0.253
He II λ 4686	0.054	0.188	0.519	0.339	0.282	0.279	0.292	0.322	0.325
H β λ 4861	1.000	1.000	1.000	1.000	1.000	1.000	1.000	1.000	1.000
[O III] λ 5007	0.978	2.667	4.895	8.672	11.598	12.220	12.328	11.920	11.792
[N I] λ 5200	0.050	0.148	0.187	0.326	0.655	0.977	1.237	1.403	1.580
[Fe VII] λ 6085	0.008	0.009	0.005	0.005	0.012	0.033	0.056	0.075	0.074
[O I] λ 6300	0.151	0.543	0.737	1.014	1.648	2.291	2.821	3.189	3.537
H α λ 6563	3.010	2.948	2.939	2.916	2.930	2.961	2.989	3.019	3.045
[N II] λ 6583	1.476	2.593	2.973	3.064	3.062	3.180	3.341	3.518	3.580
[S II] $\lambda\lambda$ 6716, 6731	1.284	1.754	1.854	1.895	2.246	2.705	3.085	3.321	3.595
[O II] $\lambda\lambda$ 7318, 7324	0.104	0.118	0.144	0.160	0.164	0.177	0.194	0.213	0.222
[S III] $\lambda\lambda$ 9069, 9532	0.926	1.946	2.219	2.670	3.300	3.877	4.322	4.640	4.899
Br α λ 4.051 μ m	0.099	0.090	0.088	0.083	0.082	0.082	0.081	0.080	0.080
[Ar VI] λ 4.530 μ m	0.000	0.000	0.001	0.001	0.003	0.008	0.011	0.012	0.012
[Ar II] λ 6.983 μ m	0.060	0.049	0.048	0.068	0.108	0.145	0.167	0.180	0.192
[Ar III] λ 6.983 μ m	0.174	0.292	0.259	0.247	0.223	0.203	0.189	0.179	0.173
[Ne VI] λ 7.652 μ m	0.008	0.007	0.005	0.016	0.059	0.146	0.237	0.338	0.406
[S IV] λ 10.44 μ m	0.064	0.852	1.362	1.436	1.324	1.143	1.018	0.904	0.844
[Ne II] λ 12.8 μ m	0.647	0.466	0.345	0.567	0.960	1.299	1.457	1.528	1.628
[Ne V] λ 14.5 μ m	0.008	0.007	0.018	0.044	0.082	0.117	0.136	0.152	0.148
[Ne III] λ 15.5 μ m	0.726	2.195	2.684	2.961	3.304	3.602	3.814	3.950	4.085
[S III] λ 18.7 μ m	0.603	0.889	0.883	1.088	1.367	1.594	1.737	1.828	1.907
[O IV] λ 25.9 μ m	0.217	2.393	7.275	5.538	5.186	4.584	4.038	3.662	3.441
log ₁₀ H β (erg cm ⁻² s ⁻¹)	-4.223	-3.757	-3.418	-3.228	-3.075	-2.944	-2.831	-2.723	-2.627